

# Solar Neutrino Problem Related Nuclear Physics Experiments

by

Weiping Liu

B. S. Beijing University (1983)

M. Sc. the Graduate School of the Ministry of  
Nuclear Industry of China (1986)

Submitted to the Graduate School of the Ministry of Nuclear  
Industry of China in partial fulfilment of the requirement  
for the degree of

Doctor of Philosophy

at the

GRADUATE SCHOOL OF THE MINISTRY OF NUCLEAR  
INDUSTRY OF CHINA

and

Department of Nuclear Physics,  
China Institute of Atomic Energy (CIAE)

September 1998

Certified by

Dazhao Ding

Professor of Physics at China Institute of Atomic Energy

Certified by

Ernst Roeckl

Professor of Physics at Mainz University, Germany

Accepted by

Prof. Naiyan Wang

Chairman of the committee of academic degree of CIAE,

chairman of the Graduate School of Nuclear Industry

Thesis work performed at China Institute of Atomic Energy,  
Beijing, P.R. China

Thesis work performed at Gesellschaft für  
Schwerionenforschung mbH (GSI) Darmstadt, Germany

Research project in China supported by National Science  
Foundation of China and by Nuclear Industry Science  
Foundation of China

Research project in Germany supported by European Union

Research activities in China supported by Honkong Quishi  
Science Foundation

Research activities in Germany supported by Deutscher  
Akademischer Austauschdienst (DAAD)

PhD study registered in the Graduate School of the Ministry of  
Nuclear Industry of China

PhD study registered in Technische Universität Darmstadt,  
Germany

# Solar Neutrino Problem Related Nuclear Physics Experiments

By

Weiping Liu

Submitted to the Graduate School of Nuclear Industry of China in  
September 1998 in partial fulfilment of the requirement for the degree of  
Doctor of Philosophy

## Abstract

This thesis firstly introduces the experimental and theoretical status of the word-wide efforts in solving the long-standing solar neutrino problem. Then the two experiments, performed within the framework of the thesis, are presented. The first experiment concerns a measurement of the  ${}^7\text{Be}(\text{d},\text{n}){}^8\text{B}$  reaction cross section at  $E_{\text{c.m.}}=5.8$  MeV, which aimed at deducing the  $S_{I\pi}(0)$  factor for the  ${}^7\text{Be}(\text{p},\gamma){}^8\text{B}$  reaction on the basis of the ANC- $S_{I\pi}(0)$  relation. The differential cross section for the  ${}^7\text{Be}(\text{d},\text{n}){}^8\text{B}$  reaction at  $E_{\text{c.m.}}=5.8$  MeV was measured by using a  ${}^7\text{Be}$  beam produced by the radioactive nuclear beam facility GIRAFFE at China Institute of Atomic Energy. The  ${}^8\text{B}$  ions were detected in full geometry with a two-dimensional position sensitive  $\Delta E$ -E counter telescope. The reaction cross section was determined to be  $58\pm 8$  mb. The angular distribution data were analyzed by using a distorted-wave Born approximation. The astrophysical  $S_{I\pi}(0)$  factor for the  ${}^7\text{Be}(\text{p},\gamma){}^8\text{B}$  reaction was derived to be  $27.4\pm 4.4$  eV b through the asymptotic normalization constant extracted from the experimental data. It provides a significant crosscheck in nuclear physics input for calculating the flux of  ${}^8\text{B}$  neutrinos.

The second experiment deals with the  $\beta$ -decay of  ${}^{40}\text{Ti}$ , which provided the neutrino absorption cross sections for ICARUS detector, which will be capable of measuring the neutrino oscillation. The  $\beta$ -decay of  ${}^{40}\text{Ti}$  and  ${}^{41}\text{Ti}$  was studied by measuring the  $\beta$ -delayed proton- and  $\gamma$ -emission at the Projectile-Fragment Separator FRS of GSI Darmstadt. The half-lives for  ${}^{40}\text{Ti}$  and  ${}^{41}\text{Ti}$  were determined to be 54(2) and 82(3) ms, respectively. The experimental  $\beta$ -decay strengths are compared with shell-model calculations and results from other measurements. The integrated Gamow-Teller strengths for  ${}^{40}\text{Ti}$  and  ${}^{41}\text{Ti}$  were found to be quenched, compared to the shell-model calculations, by factors of 0.79(3) and 0.93(3), respectively. Based on the experimental  ${}^{40}\text{Ti}$   $\beta$ -decay strength, the neutrino absorption cross-section and induced neutrino event rates for  ${}^{40}\text{Ar}$  were determined to be  $14.3(3)\times 10^{-43}$  cm<sup>2</sup> and  $9.4\pm 0.2(\text{stat.})^{+1.3}_{-1.6}(\text{syst.})$  SNU, respectively.

Thesis Supervisor:

Dazhao Ding, Professor of Physics at China Institute of Atomic Energy

Ernst Roeckl, Professor of Physics at Mainz University, Germany

To my wife, Ling Chen and my son Dongyuan.



This thesis is based on the following publications:

1. A facility for production and utilization of Radioactive beams  
Xixiang Bai, Weiping Liu, Jiuchang Qin, Zhichang Li, Shuhua Zhou, Anli Li, Youbao Wang and Yehao Cheng,  
CIAE, P.R. China,  
Nucl. Phys. A588 (1995) 273c.
2. Angular Distribution for  ${}^7\text{Be}(\text{d},\text{n}){}^8\text{B}$  Reaction at  $E_{\text{c.m.}}=5.8$  MeV and  $S_{17}(0)$  Factor for  ${}^7\text{Be}(\text{p}, \gamma){}^8\text{B}$  Reaction  
Weiping Liu, Xixiang Bai, Shuhua Zhou, Zhanwen Ma, Zhichang Li, Youbao Wang, Anli Li, Zhongyu Ma, Baoqiu Chen, Xiaodong Tang, Yinlou Han, and Qingbiao Shen,  
CIAE, P.R. China,  
Phys. Rev. Lett. 77 (1996) 611.
3. Measurement of the Angular Distribution for  ${}^7\text{Be}(\text{d},\text{n}){}^8\text{B}$  Reaction and Determination of the Astrophysical S Factor for the  ${}^7\text{Be}(\text{p}, \gamma){}^8\text{B}$  Reaction  
Weiping Liu, Xixiang Bai, Shuhua Zhou, Zhanwen Ma, Zhichang Li, Youbao Wang, Anli Li, Zhongyu Ma, Baoqiu Chen, Xiaodong Tang, Yinlou Han, Qingbiao Shen and Jincheng Xu,  
CIAE, P.R. China,  
Nucl. Phys. A616 (1997) 131c.
4.  $\beta$ -decay of  ${}^{40}\text{Ti}$   
W. Liu, M. Hellström, R. Collatz, J. Benlliure, L. Chulkov, D. Cortina Gil, F. Farget, H. Grawe, Z. Hu, N. Iwasa, M. Pfützner, A. Piechaczek, R. Raabe, I. Reusen, E. Roeckl, G. Vancraeynest, A. Wöhr,  
GSI-Kurchatov-Warsaw-IKS collaboration,  
Z. Phys. A359 (1997) 1.
5. Beta-decay of  ${}^{40}\text{Ti}$  and  ${}^{41}\text{Ti}$  and Implication for Solar-Neutrino Detection  
W. Liu, M. Hellström, R. Collatz, J. Benlliure, L. Chulkov, D. Cortina Gil, F. Farget, H. Grawe, Z. Hu, N. Iwasa, M. Pfützner, A. Piechaczek, R. Raabe, I. Reusen, E. Roeckl, G. Vancraeynest, A. Wöhr,  
GSI-Kurchatov-Warsaw-IKS collaboration,  
Phys. Rev. C (in press).

## Table of contents

<b>1. Introduction.....</b>	<b>11</b>
1.1 Solar neutrino problem.....	11
1.2 ${}^7\text{Be}(p,\gamma){}^8\text{B}$ reaction.....	17
1.3 ${}^{40}\text{Ti}$ $\beta$ -decay and ICARUS detector.....	17
<b>2. Measurement of the Angular Distribution for <math>{}^7\text{Be}(d,n){}^8\text{B}</math> Reaction and Determination of the Astrophysical S Factor for the <math>{}^7\text{Be}(p,\gamma){}^8\text{B}</math> Reaction .....</b>	<b>20</b>
2.1 Experimental procedure .....	20
2.2 Data analysis and Extraction of $S_{17}(0)$ factor. ....	24
2.3 Summary .....	26
<b>3. Beta-decay of <math>{}^{40}\text{Ti}</math> and <math>{}^{41}\text{Ti}</math> and implication for solar-neutrino detection.....</b>	<b>28</b>
3.1 Experimental Techniques.....	28
3.1.1 Production and separation of ${}^{40}\text{Ti}$ .....	28
3.1.2 Implantation and detection of protons, $\gamma$ -rays and proton- $\gamma$ coincidence.....	29
3.1.3 Energy and efficiency calibration of the detectors .....	31
3.2 Data analysis .....	31
Event selection .....	31
3.2.2 Proton spectra .....	34
3.2.3 Proton- $\gamma$ coincidence data.....	44
3.2.4 Half-life determination .....	49
3.2.5 Determination of $\beta$ -decay strength.....	51
3.3 Discussion.....	54
3.3.1 Decay strengths of ${}^{40}\text{Ti}$ .....	54
3.3.2 Decay strengths of ${}^{41}\text{Ti}$ .....	58
3.3.3 Isospin asymmetry in ${}^{40}\text{Ti}$ - ${}^{40}\text{Ar}$ mirror pair .....	58
3.3.4 Isospin impurities for ${}^{40}\text{Ti}$ and ${}^{41}\text{Ti}$ .....	59
3.3.5 Calculation of ${}^{40}\text{Ar}$ neutrino absorption cross-sections.....	59
3.4 Summary and outlook .....	63
<b>4. Acknowledgements .....</b>	<b>64</b>
<b>5. Appendix 1: Production of secondary radioactive nuclear beams.....</b>	<b>65</b>
5.1 Introduction.....	65
5.2 Production mechanism.....	65
5.2.1 Projectile fragmentation reaction.....	65
5.2.2 Transfer reaction.....	66
5.2.3 Fusion-evaporation and spallation reactions.....	67
5.3 Separation methods.....	68
5.3.1 Electromagnetic device.....	69
5.3.2 Mass separator online .....	69
5.4 Beam intensity and applications.....	69
5.5 FRS, the secondary beam line in GSI.....	70



5.5.1	General layout .....	70
5.5.2	Beam diagnostics .....	71
5.5.3	Production of $^{40}\text{Ti}$ beam .....	71
5.6	Future development .....	72
<b>6.</b>	<b>Appendix 2: Production and Use of secondary radioactive nuclear beams at HI-13 Tandem Accelerator .....</b>	<b>73</b>
6.1	Introduction .....	73
6.2	General Description of the Facility .....	73
6.3	Choice of production reactions .....	76
6.4	Design of the beam line .....	77
6.5	Beam production .....	78
6.5.1	Beam tuning procedure .....	78
6.6	Purification of RNB .....	78
6.7	Production of secondary beams .....	79
6.8	Future developments .....	81
<b>7.</b>	<b>Appendix 3: Beta-delayed proton emission, neutrino absorption rates, and shell-model calculation .....</b>	<b>83</b>
7.1	Allowed and superallowed $\beta$ -decay .....	83
7.2	IMME mass predictions .....	86
7.3	Neutrino absorption calculation .....	87
7.4	Spherical Shell-Model .....	88
<b>8.</b>	<b>Appendix 4: Formulae for deducing s factors .....</b>	<b>90</b>
8.1	Formulae concerning S factors .....	90
8.2	Formulae concerning the $S_{17}(0)$ factor from one-proton transfer reaction .....	91
<b>9.</b>	<b>Appendix 5: Further discussions on proton separation energy .....</b>	<b>93</b>
9.1	Proton separation energy and proton branching ratio .....	93
9.2	Decay measurement for $^{56}\text{Zn}$ .....	94
<b>10.</b>	<b>Appendix 6: Detailed description of <math>^{40}\text{Ti}</math> data analysis .....</b>	<b>95</b>
10.1	Calculation of the efficiencies for the detection of protons in a silicon detector .....	95
10.2	Measurement of the efficiency of NaI detectors .....	96
10.3	Estimation of uncertainty for branching ratios and decay strengths .....	97
10.3.1	Branching ratios .....	97
10.3.2	Decay strength .....	98
<b>11.</b>	<b>References .....</b>	<b>100</b>

# 1. Introduction

## 1.1 Solar neutrino problem

The neutrinos that are produced by fusion reactions (see Table 1 for details) in the interior of sun provide most valuable information on our understanding of the physical processes inside the sun and of the electroweak interaction theory concerning the basic properties of neutrino [BAH95]. For more than 20 years, the comparison between experimental results (Homestake, Kamiokande, Gallex and Sage, see Table 2) and the theoretical predictions (Standard solar model, SSM, see, e.g., Bahcall *et al.* (In the following, I shall call it BP95) [BAH95] or Dar *et al.* (I will call it DS95) [DAR96]) have yielded the so-called solar neutrino problem [BAH96]. It refers to the fact that the measured solar neutrino flux is significantly lower than that of the solar model predictions, as shown in Figure 1.

Table 1: The principle reactions of the pp chain

Reaction	Neutrino Energy (MeV)	Synonym for charac- terising neutrinos
$p + p \rightarrow {}^2\text{H} + e^+ + \nu_e$	0.0-0.4	pp
$p + e^- + p \rightarrow {}^2\text{H} + \nu_e$	1.4	pep
${}^2\text{H} + p \rightarrow {}^3\text{He} + \gamma$		
${}^3\text{He} + {}^3\text{He} \rightarrow {}^4\text{He} + 2p$		
or		
${}^3\text{He} + {}^4\text{He} \rightarrow {}^7\text{Be} + \gamma$		
then		
$e^- + {}^7\text{Be} \rightarrow {}^7\text{Li} + \nu_e$	0.86, 0.38	${}^7\text{Be}$
${}^7\text{Li} + p \rightarrow {}^4\text{He} + {}^4\text{He}$		
or		
$p + {}^7\text{Be} \rightarrow {}^8\text{B} + \gamma$		
${}^8\text{B} \rightarrow {}^8\text{Be} + e^+ + \nu_e$	0-15	${}^8\text{B}$

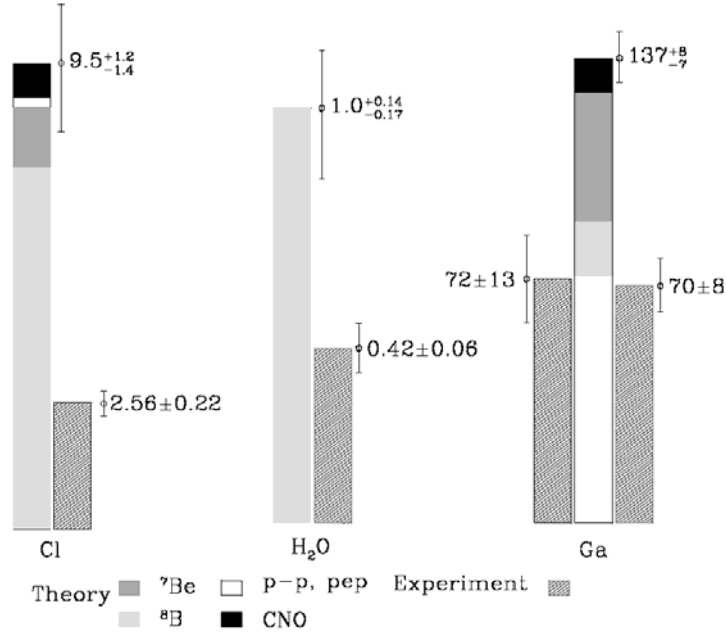


Figure 1: Comparison of measured rates and standard solar model predictions for four solar neutrino experiments [BAH95].

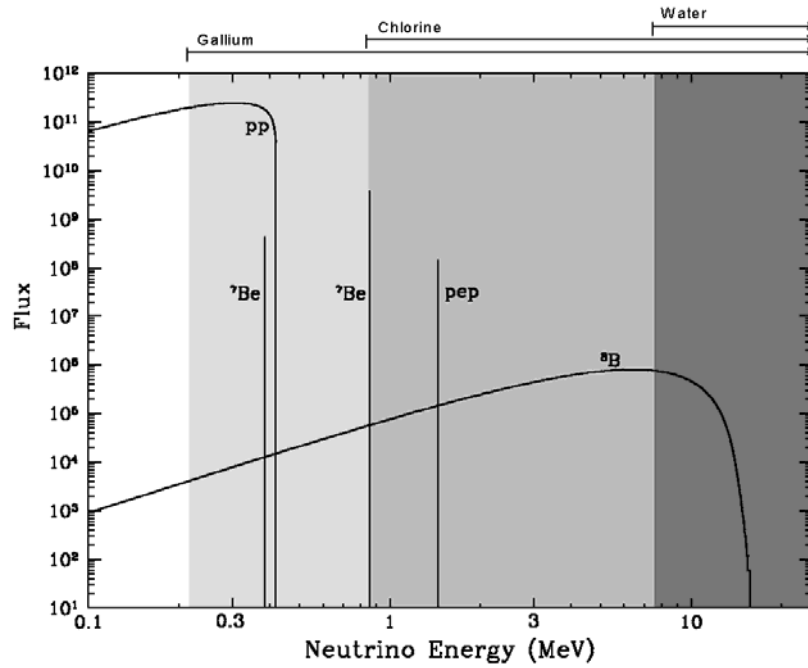


Figure 2: Energy spectrum of solar neutrinos predicted by Bahcall and Ulrich [BAH95].

Table 2: Existing solar neutrino experiments

Collaboration	Reaction	Threshold (MeV)	$\nu$ 's	Detector	technique	Statistics (/d)	Results (SNU)
Homestake	$\nu_e \text{Cl} \rightarrow \text{Ar}^*$	0.814	$^8\text{B}$ , $^7\text{Be}$	600 t Cl	radio-chemical	0.5	2.55 $\pm 0.25$
Kamiokande	$\nu_x e^- \rightarrow \nu_x e^-$	7.5	$^8\text{B}$	2 kt H <sub>2</sub> O	$\nu$ -e scattering	3	0.42 $\pm 0.06$
Gallex	$\nu_e \text{Ga} \rightarrow \text{Ge}^*$	0.235	pp, $^7\text{Be}$ ...	30 t Ga	radio-chemical	1	70 $\pm$ 8
Sage	$\nu_e \text{Ga} \rightarrow \text{Ge}^*$	0.235	pp, $^7\text{Be}$ ...	60 t Ga	radio-chemical	2	72 $\pm$ 13
Super-Kamiokande	$\nu_x e^- \rightarrow \nu_x e^-$	6.5	$^8\text{B}$	22.5 kt H <sub>2</sub> O	$\nu$ -e scattering	23	0.38 $\pm 0.03$

Over the years, the large communities of astrophysics and of nuclear physics took enormous efforts in solving this problem [BEL97]. Based on all the information available experimentally and theoretically, it seems that a solution can only be found by introducing a new physics [BAH96]. On the new physics explaining the missing solar neutrinos, especially the complete missing of  $^7\text{Be}$  neutrinos after evaluating the results of the available experiments (see Figure 1 and Figure 2), the most promising scenario is based on neutrino oscillation. It can be either oscillation in matter (MSW) or vacuum oscillation (VO) as indicated in Table 3 [BEL97A]. Very recently, the Super-Kamiokande group announced the finding of neutrino oscillation - the first experimental observation of non-zero neutrino mass [FUK98].

Table 3: Intervals allowed for the  $^7\text{Be}$  neutrinos flux as 90 % C. L. In the case of four favoured scenarios for explaining solar neutrino problem. The limits of the interval were reported in units of the flux predicted by the BP95.

	Standard neutrinos	VO	MSW-LMA	MSW-SMA
Allowed interval	0-0.14	0.38-0.98	0.50-0.71	0.20-0.50

Standard neutrinos: extreme solar model; LMA: large mixing-angle results; SMA: small mixing-angle results.

To confidentially reach such a conclusion, it is very important to carefully check the uncertainties in the terrestrial neutrino experiments and in the solar model calculations for neutrino production [MOR94, DAR96]. For example, the different treatments of the diffusion effect in the solar models BP95 and DS95 resulted in neutrino

fluxes that differed by 31 %. Furthermore, the different selections of solar and nuclear physics parameters in these two models produced results differed by up to 62 % from each other [DAR96, BAH95]. These deviations are presented in Table 4 and Table 5. Apparently, these differences were much larger than the uncertainties assigned to a single solar model [BAH95], see also Table 6. Therefore, apart from a ‘solar neutrino problem’, there appears to be also a ‘solar model problem’. Thus it is desirable to reach to agreement in treating the diffusion effects and in selecting the nuclear and astrophysical input parameters in solar model calculations.

Table 4: Comparison between the  $^8\text{B}$  solar neutrino fluxes (in  $10^6 \text{ cm}^{-2}\text{s}^{-1}$ ) calculated from the best solar models of Bahall-Pinsonneault (BP95) and Dar-Shaviv (DS95) with diffusion (D) and without diffusion (ND), and with BP95 input parameters [DAR96].

Input	ND	D	With input of BP95	ND
BP95	4.85	6.62		4.85
DS95	2.54	2.49		5.07

Table 5: Nuclear input parameters used in models BP95 and DS95 [DAR96], compared with recent measured and recommended values.

	$S_{17}(0)$	$S_{34}(0)$	$S_{33}(0)$	$S_{11}(0)$
DS95	17 eV b	0.51(2) keV b	5.6 MeV b	$4.07 \times 10^{-22}$ keV b
BP95	22.4 eV b	0.524 keV b	4.99 MeV b	$3.896 \times 10^{-22}$ keV b
Recent meas- urement			5.4(3) MeV b [JUN98]	
Recent compi- lation [ADE97]	$19^{+4}_{-2}$ eV b			$4.00(2) \times 10^{-22}$ keV b

In this context, nuclear physics can make a significant contribution. In a solar model calculation, the uncertainties of nuclear reaction cross sections, such as those of  $^7\text{Be}(p,\gamma)^8\text{B}$ , contribute significantly to the uncertainties associated with the solar model prediction of neutrino fluxes, as demonstrated in Table 6 [BAH95] and Appendix 3. However, in order to compare the prediction of a given solar model with the solar neutrino experiments, the neutrino fluxes predicted by this model have to be translated into reaction rates by using the nuclear absorption cross section of the detector material. Therefore, another important nuclear physics contribution consists in an accurate determination of the absorption cross section in the relevant detector material. The Homestake experiment (neutrino detection via  $^{37}\text{Cl}$  inverse  $\beta$ -decay) and the proposed ICARUS experiment (neutrino detection using  $^{40}\text{Ar}$  inverse  $\beta$ -decay) may serve as examples. This argument is expressed in the following simple formula:

Predicted reaction rates = Absorption cross section (nuclear physics input, e.g.  $^{37}\text{Ca}$  or  $^{40}\text{Ti}$   $\beta$ -decay)  $\times$  Solar neutrino flux (solar model + nuclear physics input, e.g.  $^7\text{Be}(p,\gamma)^8\text{B}$  reaction)

Table 6:  $^8\text{B}$  neutrino flux and theoretical uncertainties for the standard solar model, with the fractional uncertainties associated with important parameters, e.g., p- $^7\text{Be}$  reaction rate, heavy-element-to-hydrogen ratio  $Z/X$ , solar luminosity  $L_\odot$ , and solar age  $t_{age}$  [BAH95].

Flux ( $\text{cm}^{-2}\text{s}^{-1}$ ) <sup>a</sup>	p-p	$^3\text{He}$ - $^3\text{He}$	$^3\text{He}$ - $^4\text{He}$	p- $^7\text{Be}$	$Z/X$	$L_\odot$	$t_{age}$	Opa- city	Diffu- sion
$6.62 \times 10^6$ ( $1.00^{+0.14}_{-0.17}$ )	0.03	0.02	0.03	0.09	0.08	0.03	0.01	0.05	0.08

<sup>a</sup>using  $S_{17}(0)$  value of  $22.4 \pm 2.1$  eV b.

Moreover, the attempt to minimize the uncertainties of neutrino detection has lead to new generation detectors [OBE98], which aim not only at measuring the neutrino flux of individual branches (pp, pep,  $^7\text{Be}$  and  $^8\text{B}$ ) but also at detecting neutrino oscillation. The latter phenomenon is studied by measuring

- (i) the distortion of the neutrino energy spectra compared with solar model prediction (Super-Kamiokande),
- (ii)  $^7\text{Be}$  neutrino (Borexino),
- (iii) the complete fluxes of neutrinos independent of their flavor (SNO),
- (iv) the day-night difference of neutrino fluxes as predicted by MSW theory or seasonal difference as predicted by VO (Super-Kamiokande),
- (v) the ratio between the electron neutrino with neutrinos of all flavors (ICARUS).

A summary of new generation neutrino detectors is show in Table 7. Apart from the observation of solar neutrinos, the long base line experiments provide an alternative way for measuring the possible neutrino oscillations [BEL97], as summarized in Table 8. Here ICARUS detector will serve as an neutrino detector.

In the present thesis, I shall give a detailed description of my contributions to two experiments which both yield to the nuclear physics data relevant to the solar neutrino problem. The first one is the determination of the  $^7\text{Be}(p,\gamma)^8\text{B}$  cross section [LIU96], responsible for the  $^8\text{B}$  neutrino flux, the second one is the measurement of  $^{40}\text{Ti}$   $\beta$ -decay [LIU97, LIU98], which is related to the  $^{40}\text{Ar}$  absorption cross section in the ICARUS detector.

Table 7: New solar neutrino experiments

Collaboration	Reaction	Threshold (MeV)	$\nu$ 's	Detector	Technique	Statistics SSM (/d)	Beginning date
SNO	$\nu_e d \rightarrow p p e^-$ $\nu_x d \rightarrow \nu p n$	5.0	$^8\text{B}$	1 kt $\text{D}_2\text{O}$	abs., nc disinit	20 7	1999
GNO	$\nu_e \text{Ga} \rightarrow \text{Ge}^* e^-$	0.235	pp, $^7\text{Be}...$	30-100 t Ga	Radiochemical	1	1999
BOREXINO	$\nu_x e^- \rightarrow \nu_x e^-$	0.25	$^7\text{Be}$	100 t liquid scint.	$\nu$ -e scattering	55	1999
ICARUS	$\nu_x e^- \rightarrow \nu_x e^-$ $\nu_e \text{Ar} \rightarrow \text{K}^* e^-$	5.0	$^8\text{B}$	600 t liquid Ar	$\nu_e$ abs., TPC	0.6 4	1999
Iodine	$\nu_e \text{I} \rightarrow \text{Xe}^* e^-$	0.789	$^7\text{Be}$ , $^8\text{B}...$	100 t iodine	Radiochemical		1999
HELLAZ	$\nu_x e^- \rightarrow \nu_x e^-$		pp, $^7\text{Be}$	gaseous He	$\nu_e$ -scattering, TPC		Develop.
HERON	$\nu_x e^- \rightarrow \nu_x e^-$		pp, $^7\text{Be}$	liquid He	$\nu_e$ -scattering		Develop.

Table 8: Long baseline experiments

$\nu_u$ source	$\nu$ detector	Distance (km)	Beginning date
KEK 12 GeV p	Super-Kamiokande	225	1999
Fermi Lab. SPS	MINOS 10 kt	730	2001
CERN 80 GeV p	ICARUS 500 t	732	

## 1.2 ${}^7\text{Be}(p,\gamma){}^8\text{B}$ reaction

The high energy neutrinos from the  $\beta^+$  decay of  ${}^8\text{B}$  produced via the  ${}^7\text{Be}(p,\gamma){}^8\text{B}$  reaction at solar energies play a very important role in the solar neutrino problem [BAH95], as explained in Section 1.1. Therefore, the astrophysical  $S_{17}(0)$  factor for the  ${}^7\text{Be}(p,\gamma){}^8\text{B}$  reaction has attracted an increasing attention for many years. There were a number of considerable efforts to study the  $S_{17}(0)$  factor through both direct radiative capture reaction [FIL83, HAM98] and Coulomb dissociation reaction of  ${}^8\text{B}$  [MOT94]. However, the obvious disagreement among the experimental results is still a challenging puzzle. Therefore further experiments were called for to reduce the uncertainties of the  $S_{17}(0)$ . Recently, the proton pickup reactions of  ${}^7\text{Be}$  were proposed as an indirect way to extract the  $S_{17}(0)$  factor by introducing a simple relation between the asymptotic normalization constant (ANC) and the  $S_{17}(0)$  factor [XU94]. This approach was expected to yield the  $S_{17}(0)$  factor with an accuracy at least comparable to that of direct radiative capture or Coulomb dissociation reactions, and could thus provide a valuable cross examination as an independent method. We carried out a measurement of cross section and angular distribution of the proton-pickup  ${}^7\text{Be}(d,n){}^8\text{B}$  reaction using a radioactive  ${}^7\text{Be}$  beam.

The detailed description of this work, which has already been published [LIU96], is presented in Chapter 2 and Appendix 2. To the best of my knowledge, only two experiments were dedicated to this reaction, which were performed at different energies and presented only cross sections with large uncertainties without the measurement of angular distributions [HAI83, YAM89]. In this work, as one of the group leader, I contributed in experiment, in data analysis, and in paper writing.

## 1.3 ${}^{40}\text{Ti}$ $\beta$ -decay and ICARUS detector

In the ICARUS detector [ICA93], the energy and the direction of the electrons scattered by the incoming solar neutrinos, as well as of the electrons produced in the inverse  $\beta$ -decay  ${}^{40}\text{Ar}(\nu_e, e^-){}^{40}\text{K}$ , can be measured in a large-volume liquid argon time-projection chamber, see Table 7. Since the inverse  $\beta$ -decay to the  ${}^{40}\text{K}$  ground state is forbidden, each neutrino-absorption event is accompanied by  $\gamma$ -rays emitted from excited  ${}^{40}\text{K}$  levels, which produce Compton electrons, as shown in Figure 3. In this way the electron multiplicity distinguishes scattering and absorption events, making it possible to measure the ratio between these two types of events. This ratio is independent of the total neutrino flux impinging on a terrestrial detector whereas it depends significantly on possible neutrino oscillations. This is due to electrons being scattered by electron neutrinos as well as by  $\mu$  and  $\tau$  neutrinos while the production of electrons via neutrino absorption is restricted to only electron neutrinos. Furthermore, quantitative information on the oscillation probability  $\nu_e \rightarrow \nu_{\mu, \tau}$  can be obtained from the experimental ratios.

As indicated in Section 1.1, the cross sections for the different interaction processes must be known very well for a reliable evaluation of the ICARUS data. The scattering rates can be accurately calculated by using the standard electroweak theory [BAH86], whereas the situation is more complicated for the case of neutrino absorption. While the value for the Fermi transition strength  $B(F)$  between the  ${}^{40}\text{Ar}$  ground state and the isobaric analog state (IAS) in  ${}^{40}\text{K}$  is given by the model-independent sum-rule [BRO85], it is more difficult to determine the transition strengths  $B(GT)$  for



the individual contribution of allowed Gamow-Teller (GT) transitions to the neutrino-capture rate. In principle, the  $B(GT)$  values for the inverse  $\beta$ -decay can be deduced by using shell-model theory or from data measured for the zero-degree charge-exchange reaction  $^{40}\text{Ar}(p,n)^{40}\text{K}$ . However, as has recently been shown, shell-model calculations failed to reproduce the  $B(GT)$  distributions measured in the region around  $^{40}\text{Ca}$  [ADE91, TRI95A, TRI95B, TRI97A]. Furthermore, the proportionality of  $\beta$ -decay transition strengths and zero-degree (p,n) reaction rates has been questioned, because a comparison of the  $\beta$ -decay of  $^{37}\text{Ca}$  with the  $^{37}\text{Cl}(p,n)^{37}\text{Ar}$  mirror reaction [ADE97] showed that the differences were probably not entirely due to isospin-violating effects [ORM89, BRO92]. Hence, a calibration of the neutrino absorption rate based on shell-model calculations or on (p,n)-reactions might jeopardize the quality of the ICARUS results.

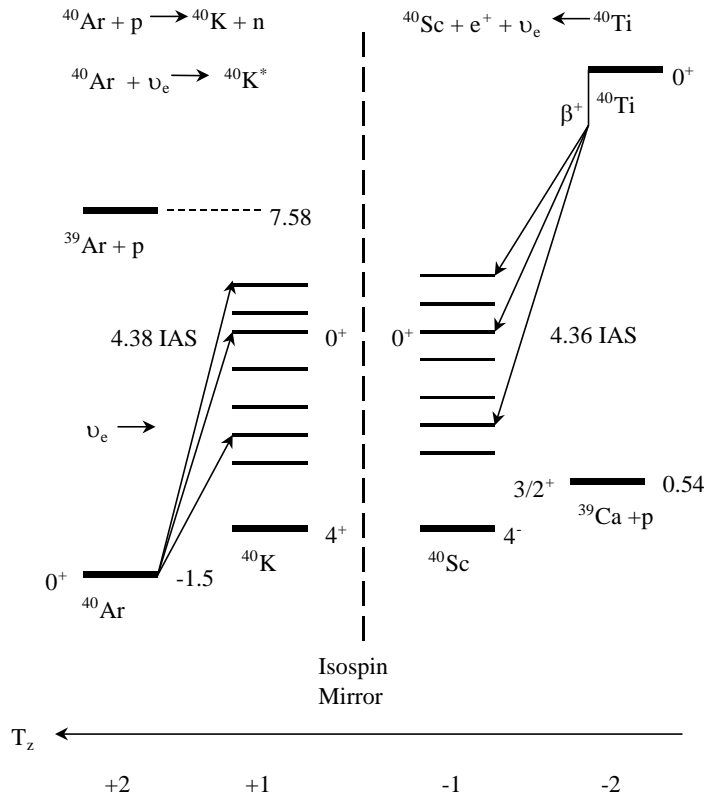
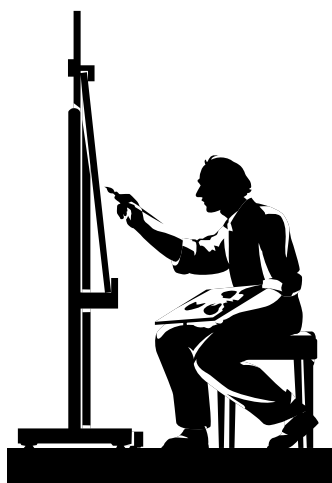


Figure 3: Schematic presentation of the mirror symmetry between  $^{40}\text{Ti}$  and  $^{40}\text{Ar}$ .

An alternative possibility of calibrating the  $^{40}\text{Ar}$  neutrino capture rate is to use, under the assumption of isospin symmetry, the  $B(GT)$  values of the mirror  $\beta$ -decay of  $^{40}\text{Ti}$ , as can be seen in Figure 3 (see Appendix 2 for a general description of a  $\beta$ -decay process). In principle, the large energy release of the  $^{40}\text{Ti}$  decay ( $Q_{EC} = 11680(160)$  keV [AUD97]) enables one to extract all information that is relevant for the GT contributions to the rate of solar neutrinos absorbed by  $^{40}\text{Ar}$ , provided sufficiently accurate half-life and branching-ratio data are available. It is interesting to note that the efficiency calibration for the  $^{37}\text{Cl}$  experiment has recently been achieved in a similar way by using the  $B(GT)$  values measured in the  $\beta$ -decay of  $^{37}\text{Ca}$  (see [TRI97A] for a recent review).

Another motivation for this study was to obtain data on high energy-release  $\beta$ -decay at the beginning of the  $fp$  shell similar to those available from recent experiments on the  $\beta$ -decays of  $^{36}\text{Ca}$  [TRI95A],  $^{37}\text{Ca}$  [TRI95B], and  $^{38}\text{Ca}$  [AND96]. Such data are of interest for further clarification of the evident discrepancy between data from  $\beta$ -decay, charge-exchange reactions, and shell-model calculations. It is interesting to note that  $^{40}\text{Ti}$ , together with  $^{36-39}\text{Ca}$ , are the only nuclei whose  $\beta$ -decays represent mirror transitions to (p,n) reactions on stable-isotope targets.

Prior to the work described here, the  $^{40}\text{Ti}$   $\beta$ -decay had been investigated in only one measurement under severe experimental limitation [DÉT90]. The latter measurement yielded only singles data of  $\beta$ -delayed protons whereas in the experiment presented here proton- $\gamma$  coincidences were measured. This information is indispensable in order to clarify whether the  $\beta$ -delayed proton emission populates the ground state and/or excited states of  $^{39}\text{Ca}$ . Furthermore, the decay of  $^{41}\text{Ti}$  was studied in order to establish an energy calibration for the  $^{40}\text{Ti}$  proton data and to improve, by detecting  $\beta$ -delayed  $\gamma$ -rays, the results of previous  $^{41}\text{Ti}$  studies. A short communication and a detailed description of the  $^{40}\text{Ti}$  data obtained in this work were published [LIU97, LIU98], and similar work was later on reported [TRI97B]. Chapter 4 of the present thesis summarizes the results of a refined data analysis compared to [LIU97] and presents details of the experimental technique, the data analysis, and the determination of experimental  $B(GT)$  values. In this work, I contributed in experiment, in data analysis, and in paper writing.



## 2. Measurement of the Angular Distribution for ${}^7\text{Be}(d,n){}^8\text{B}$ Reaction and Determination of the Astrophysical S Factor for the ${}^7\text{Be}(p,\gamma){}^8\text{B}$ Reaction

### 2.1 Experimental procedure

The  ${}^7\text{Be}(d,n){}^8\text{B}$  experiment was performed by using a radioactive beam line GIRAFFE (see Appendix 2 for details) built at HI-13 tandem accelerator of China Institute of Atomic Energy. The details of GIRAFFE have already been reported [BAI95]. An important alteration for purifying the secondary beams was that the angle (acceptance angle) for collecting the primary reaction products was changed from  $0^\circ$  to  $3^\circ$ . The  ${}^7\text{Be}$  beam was produced with an energy of 26.0 MeV via the  ${}^1\text{H}({}^7\text{Li}, {}^7\text{Be})n$  reaction by bombarding a  $\text{H}_2$  gas cell at 1.2 atm pressure with 34 MeV  ${}^7\text{Li}$  ions, which were produced by the HI-13 tandem accelerator. With an appropriate setting of the parameters of the secondary beam line, we focused the  ${}^7\text{Be}$  beam to a spot of 10 mm diameter with an angular divergence of  $1.9^\circ$  FWHM. The beam typically comprised more than 90 %  ${}^7\text{Be}^{4+}$  ions with the major contaminants being  ${}^7\text{Be}^{3+}$  ( $<1\%$ , 12 MeV) and  ${}^7\text{Li}^{3+}$  ions ( $<9\%$ , 13 MeV).

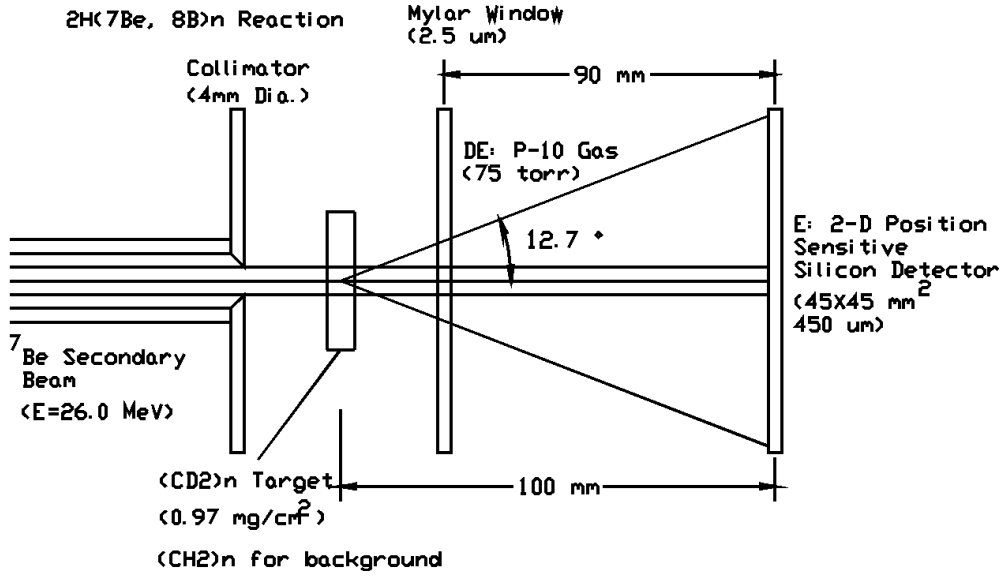


Figure 1: Experimental setup.

The  ${}^7\text{Be}$  beam was further collimated by using a  $\phi 4$  mm aperture and was directed onto a secondary target placed on the final focal plane. The resulting beam energy resolution was 1.2 MeV FWHM. The experimental setup is shown in Figure 1. A deuterated polyethylene ( $(\text{CD}_2)_n$ ) foil of  $0.97 \text{ mg}/\text{cm}^2$  in thickness was used as the secondary target for studying the reaction of interest, and a polyethylene ( $(\text{CH}_2)_n$ ) foil was used for determining the background. The reaction products were detected and identified by using a  $\Delta E$ -E counter telescope. It consisted of a 9 cm long ionization chamber filled with 75 torr P-10 gas backed by a  $45 \times 45 \text{ mm}^2$  Hamamatsu two-dimensional position sensitive silicon detector (PSSD) of 450  $\mu\text{m}$  in thickness. The PSSD enabled us to determine both the energy and the emission angle of the outgoing particles. The inverse kinematics of the  ${}^1\text{H}({}^7\text{Be}, {}^8\text{B})n$  reaction restricted the maximum angle of the  ${}^8\text{B}$  particles to about  $9^\circ$ , thus the full angular distribution was covered. The overall

angular resolution was  $1.1^\circ$  FWHM, which resulted from the  $^7\text{Be}$  beam position uncertainty ( $0.6^\circ$ ), the  $^7\text{Be}$  beam angular divergence after collimation ( $0.8^\circ$ ), the  $^7\text{Be}$  beam energy resolution ( $<0.3^\circ$ ), the position resolution of PSSD ( $0.6^\circ$ ), and the  $^8\text{B}$  angular straggling in passing materials ( $<0.4^\circ$ ).

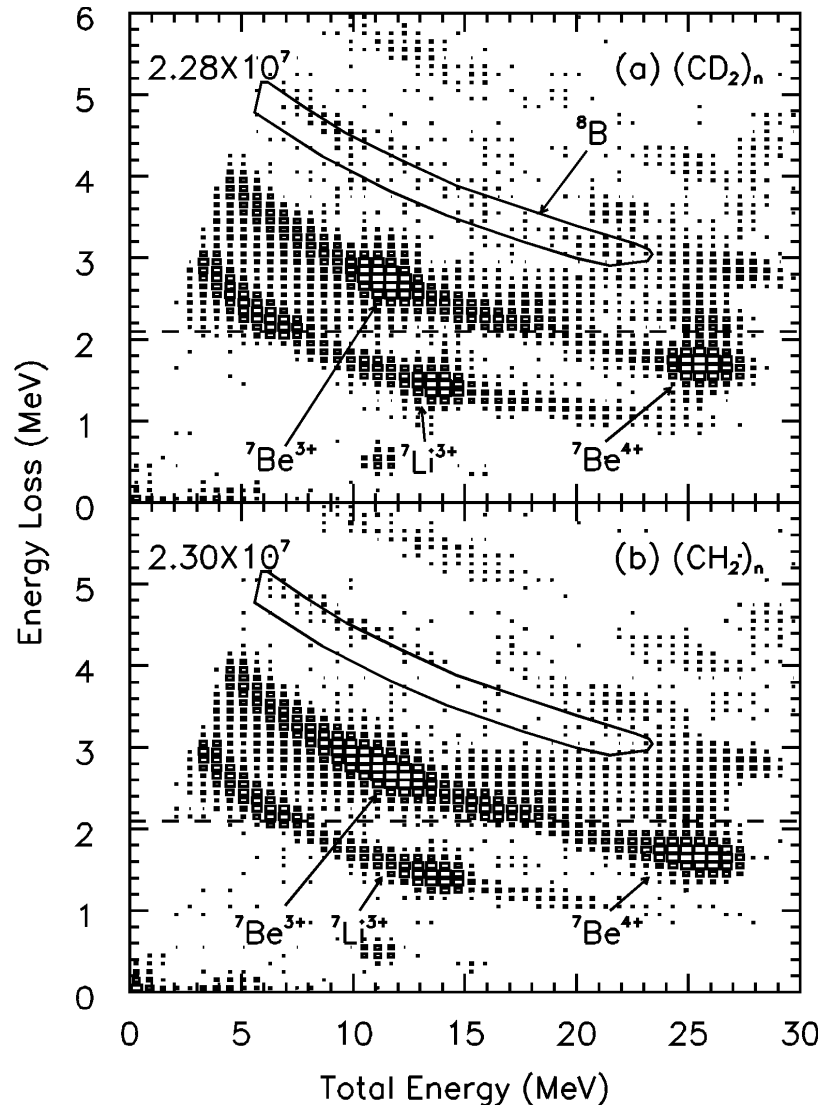


Figure 2: Contour plots of energy loss versus total energy for (a)  $(\text{CD}_2)_n$  and (b)  $(\text{CH}_2)_n$  targets. The numbers of the incident  $^7\text{Be}$  particles are shown in the upper-left corner of each panel. The size of the data points is proportional to the logarithm of the counts per channel; the smallest size corresponds to 1 count per channel. The events below the dashed line are the beam components that were scaled down by a factor of 100.

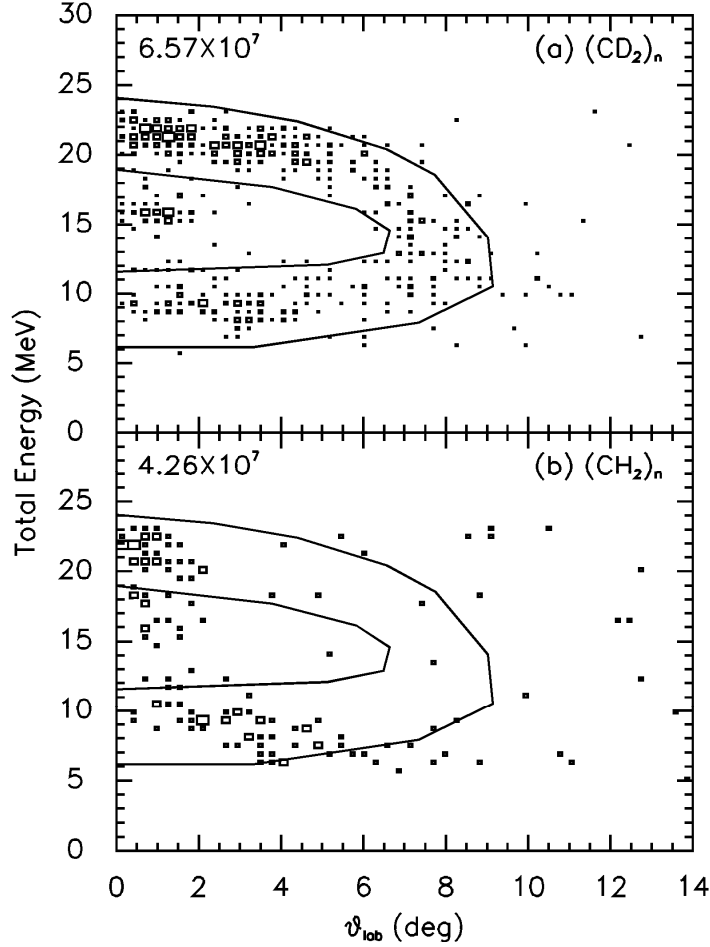


Figure 3: Contour plots of  $E_t$  vs.  $\theta_{lab}$  for (a)  $(CD_2)_n$  and (b)  $(CH_2)_n$  targets. The numbers of the incident  $^7Be$  particles are shown in the upper-left corner. Here, the size of the points is proportional to the counts per channel.

The experiment scheme also facilitated beam normalization with high accuracy because the counter telescope simultaneously recorded the  $^7Be$  beam. However, the latter fact led to serious pulse-pileup. In order to solve this problem, the beam intensity on the target was kept at a very low level of 200 to 400 counts per second. Moreover, a particular consideration was paid to pileup rejection. A mixing trigger was used, in which the logical output for the  $^7Be$  beam events, characterized by the low energy loss in ionization chamber ( $<2.1$  MeV), were scaled down by a factor of 100. This measure lightened the unnecessary burden of the data taking system and of the off-line analysis. The beam time used for the  $(CD_2)_n$  target was approximately 150 hours, during which about 300  $^8B$  events were accumulated. The background measurement with the  $(CH_2)_n$  target took about 50 hours.

A contour plot of  $\Delta E$  versus  $E_t$  from the runs with  $(CD_2)_n$  target is shown in Figure 2(a), where  $\Delta E$  and  $E_t$  denote the energy loss and the total energy of particles respectively. The two-dimensional gate in Figure 2(a) refers to the  $^8B$  candidates from the  $^2H(^7Be, ^8B)n$  reaction. The events outside this gate were well identified to be the beam components, the remaining peak pileup pulses corresponding to detection of  $^7Be$ , as well as of products from other reaction channels. Figure 3(a) displays a contour plot of  $E_t$  versus  $\theta_{lab}$  for the events within the gate from the sum of all runs, where the  $\theta_{lab}$  is the laboratory emission angle that was determined from the PSSD position data. A parabola-shaped gate finally selected  $^8B$  events. The corresponding events from the

background measurements with  $(\text{CH}_2)_n$  target are shown in Figure 2(b) and Figure 3(b). It can be seen from Figure 3(b) that the background mainly appeared around  $0^\circ$  and obviously resulted from the  $^7\text{Be}$  events piling up on each other. Because the considerable contaminants from the reactions on carbon that infiltrated into the region corresponding to center-of-mass (CM) angle  $\theta_{c.m.} > 160^\circ$ , the data in that region were discarded. The total cross section for  $^7\text{Be}(d,n)^8\text{B}$  reaction at  $E_{c.m.}=5.8$  MeV was determined to be  $58 \pm 8$  mb. The uncertainty mainly stems from statistics (9 %), background subtraction (7 %), from the influence of the target thickness (6 %). The data were converted into the CM frame, where the non-uniform angular intervals were assigned in accordance with angular uncertainties discussed above. The resulting CM angular distribution is presented in Figure 5. Since  $^8\text{B}$  has no excited states with detectable half-lives in the present experiment, the data included only the ground state transition. A flow chart of the data processing is shown in Figure 4.

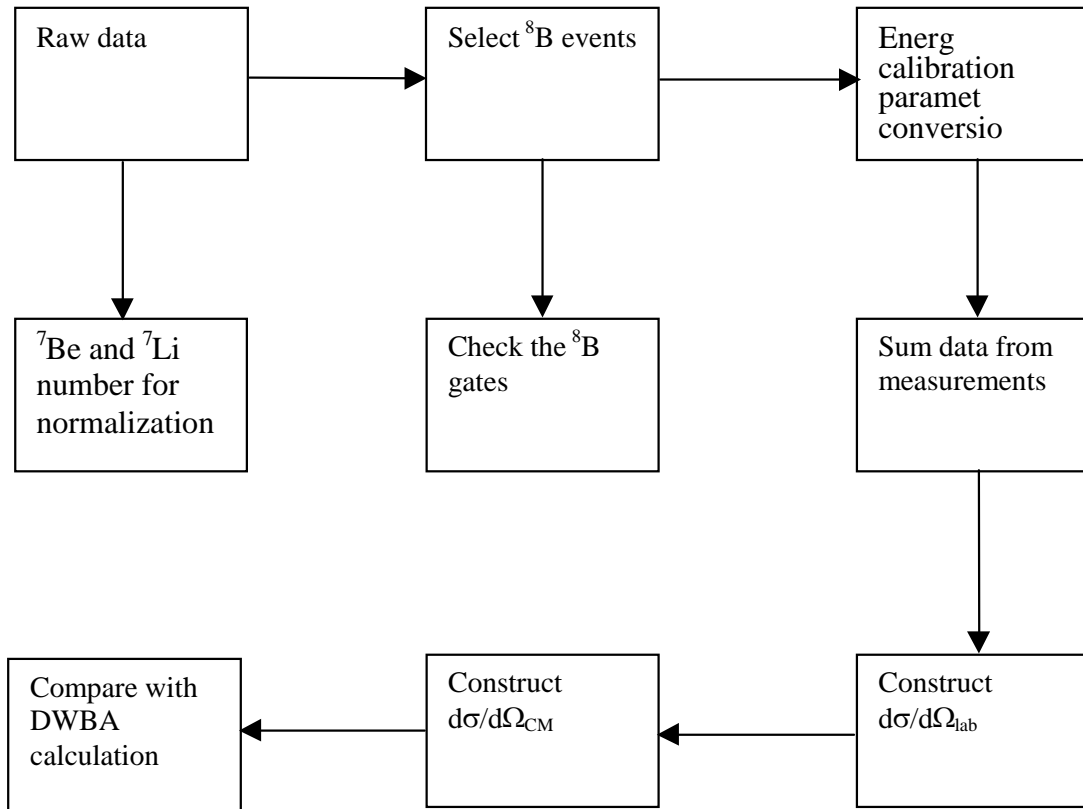


Figure 4: The flow chart of data analysis for  $^7\text{Be}(d,n)^8\text{B}$  reaction.

## 2.2 Data analysis and Extraction of $S_{17}(0)$ factor.

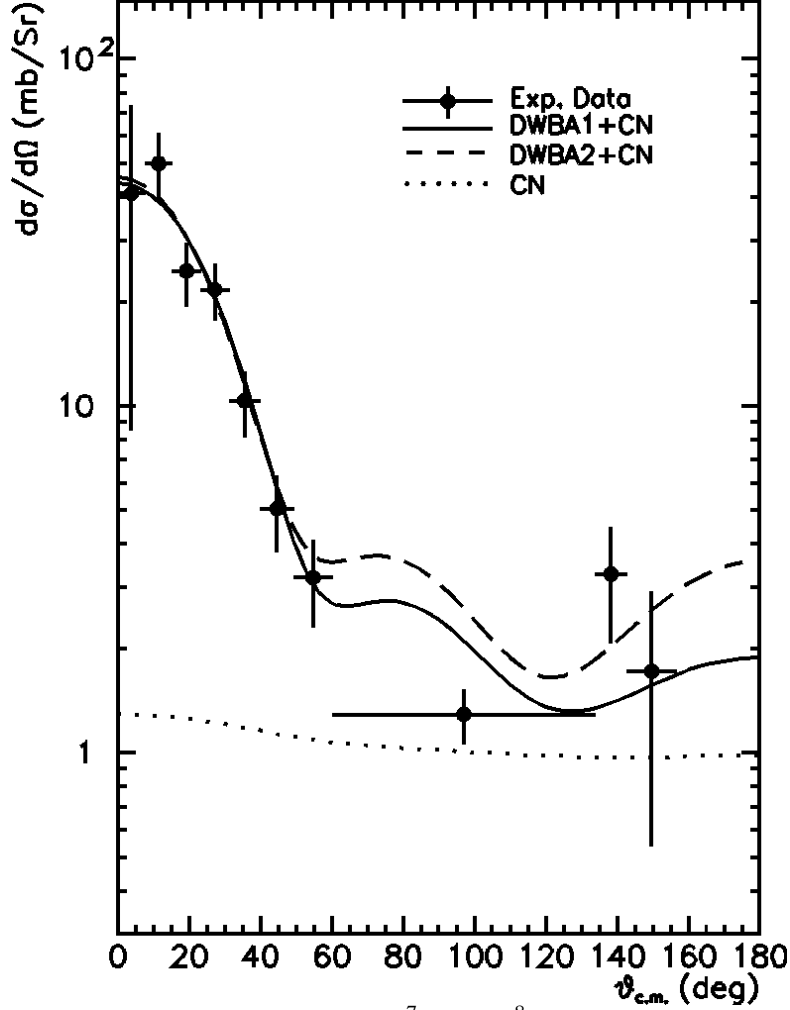


Figure 5: Differential cross section for the  ${}^7\text{Be}(d,n){}^8\text{B}$  reaction at  $E_{c.m.} = 5.8$  MeV together with the theoretical calculations. DWBA1 and DWBA2 denote the normalized DWBA calculations with OM parameter set 1 and set 2 in Table 1 respectively, CN refers to the compound nucleus contribution. The parameters of proton bound state were  $r_0 = 1.25$  fm and  $a = 0.65$  fm, and the spectroscopic factors corresponding to DWBA1 and DWBA2 were 1.21 and 1.34 respectively.

The DWBA code [KUN] was adopted in the analysis of the data. The peripheral amplitudes of the reaction corresponding to a large contribution to the differential cross sections in the peak region. Therefore our consideration was restricted to the differential cross sections measured in peak region at the small CM angles. The method for extracting the empirical spectroscopic factor  $S_{lj}$  from experiment is based the conventional relation

$$\sigma_{\text{exp}}(\theta_0) - \sigma_{\text{CN}}(\theta_0) = S_{lj} \sigma_{\text{DWBA}}(\theta_0) \quad , \quad (1)$$

where  $\sigma_{\text{exp}}(\theta_0)$  and  $\sigma_{\text{DWBA}}(\theta_0)$  are the values of the experimental and theoretical differential cross sections in the peak region, respectively, and  $\sigma_{\text{CN}}(\theta_0)$  is the theoretical compound nucleus contribution. In this procedure,  $D_0^2$  is taken to be  $1.58 \times 10^4$   $\text{MeV}^2 \text{fm}^3$  [STA83], where  $D_0$  stands for the volume integral constant in the zero-range approximation. As has already been pointed out in previously [BAR80, GON82], the

$\sigma_{DWBA}(\theta)$  value has a large uncertainty, which strongly depended on the geometry parameters of the Woods-Saxon potential  $r_0$  and  $a$  (the radius and diffuseness parameters) used for calculating the wave function of a single-particle bound state. Such an uncertainty was removed by introducing the ANC of the true overlap functions,  $C_{lj}$ , which is related to the spectroscopic factor by

$$C_{lj}^2 = S_{lj} b_{nlj}^2, \quad (2)$$

with  $b_{nlj}$  being the asymptotic normalization of a single-particle radial wave function  $u_{nlj}(r)$  in the shell-model calculation with the geometry parameters  $r_0$  and  $a$  of a Woods-Saxon potential,

$$u_{nlj}(r) \approx b_{nlj} W_{-\eta, l+\frac{1}{2}}(2\kappa r) / r, \quad r > R_N. \quad (3)$$

Here  $R_N$  is the nuclear interaction radius between the proton and  ${}^7\text{Be}$ ,  $W_{-\eta, l+\frac{1}{2}}(2\kappa r)$  the Whittaker function, and  $\eta$  the Sommerfeld parameter. The optical-potential parameters for the deuteron and neutron were carefully chosen by fitting the experimental scattering data of the nearby nuclei at the closest energies. The resulting parameters were then extrapolated to the energies of the present study by a reasonable energy dependence. The results are listed as set 1 in Table 1. The depth of the Woods-Saxon potential for the proton bound state was chosen by fitting the  ${}^7\text{Be}$  proton separation energy of 0.137 MeV for given geometry parameters. The overall agreement between the measured and calculated differential cross sections was fairly good, as shown in Figure 5. The peak value of the differential cross section was found to be insensitive to the distorted-wave optical potential parameters. It made about 10 % change of ANC value when replacing the optical potentials set 1 by set 2 [PER76], as shown in Table 1, though the two sets of parameters are quite different. The ANC  $C_{1\frac{3}{2}}^2$  for  ${}^8\text{B} \rightarrow {}^7\text{Be}+p$  was extracted to be  $0.711 \pm 0.092$  fm from the present experiment data by using Eqs. (1)-(3), where  $S_{1\frac{3}{2}}$  was obtained as the weighted average of the experimental data in the peak area. The uncertainty included only experimental ones. When the geometry parameters  $r_0$  and  $a$  were changed, the variation of the ANC values was only about one percent, though the asymptotic normalization of the  $u_{11\frac{3}{2}}$ , as well as the spectroscopic factor, changed dramatically. Xu *et al.* [XU94] showed that  $b_{nlj}^2 / S_{l7}(0)$  is almost constant ( $\approx 0.026$ ) for different proton-bound wave functions in  ${}^8\text{B}$ , in which the spectroscopic factor was chosen to be the same as that given by Barker [BAR80], i.e.  $S_{l=1,j} \approx 1.0$ .

Following the procedure proposed by Xu *et al.*, the  $S_{l7}(0)$  factor for  ${}^7\text{Be}(p,\gamma){}^8\text{B}$  was derived to be  $27.4 \pm 4.4$  eV b from the ANC value determined in this work. The uncertainty includes the experimental ones (13 %) and the estimated contribution ( $\sim 10\%$ ) from the theoretical calculation, which arose from the uncertainty of the optical potential, of the CN calculation, and of the  $D_0^2$  value.



Table 1: The optical potential parameters used in DWBA calculation and the corresponding ANC and  $S_{I7}(0)$  values.

Set	Channel	$V$	$r$	$a$	$4W_D$	$r_D$	$a_D$	$4V_{SO}$	$r_{SO}$	$a_{SO}$	$C_{ij}^2$ (fm)	$S_{I7}(0)(\text{eV b})$
1	${}^7\text{Be}+d$	-138.74	1.02	0.86	65.36	1.31	0.76	-28.0	1.64	0.81		
	${}^8\text{B}+n$	-48.19	1.13	0.72	45.32	1.43	0.66	-24.8	1.13	0.77	$0.711\pm0.092$	$27.4\pm3.6$
2	${}^7\text{Be}+d$	-118.00	1.00	0.94	27.48	1.98	0.59	-34.0	1.00	0.94		
	${}^8\text{B}+n$	-42.36	1.35	0.55	37.76	1.35	0.75	-20.0	1.35	0.55	$0.796\pm0.103$	$15.2\pm1.5$

For  ${}^7\text{Be}+d$  of set 1, the additional parameters are  $W = -14.84$ ,  $r_W = 1.64$ ,  $a_W = 0.29$ ;  $V$  and  $W$  are in MeV,  $r$  and  $a$  are in fm.

### 2.3 Summary

In the present experiment the angular distribution of the  ${}^7\text{Be}(d,n){}^8\text{B}$  reaction was measured for the first time. The resulting  $S_{I7}(0)$  factor of  $27.4\pm4.4$  eV b for the  ${}^7\text{Be}(p,\gamma){}^8\text{B}$  reaction can be compared with values used in standard solar models ( $22.4\pm2.1$  eV b in [BAH95] and 17 eV b in [DAR96]). A recent refined calculation based on these data yielded a  $S_{I7}(0)$  value of  $23.5\pm6.7$  eV b [GAG97] by using finite-range DWBA (In the present work a zero-range DWBA was used). A measurement of the  ${}^7\text{Be}(d,n){}^8\text{B}$  reaction by our group at higher energy ( $E_{\text{c.m.}} = 8.3$  MeV), yielded a comparable result of  $25\pm5$  eV b [TAN97]. This result conformed to some extent the reliability of the present indirect method to determine  $S_{I7}(0)$ . A more up-to-date DWBA analysis base on this experimental data including the detailed analysis of the theoretical uncertainties will be presented soon [FER98]. There is also a preliminary result from  ${}^{10}\text{B}({}^7\text{Be}, {}^8\text{B}){}^9\text{Be}$  reaction, which yielded a  $S_{I7}(0)$  factor of  $18.7\pm2.9$  eV b [AZH98].

Recently, a new direct measurement of  ${}^7\text{Be}(p,\gamma){}^8\text{B}$  reaction has been performed [HAM98], yielding the  $S_{I7}(0)$  value of  $18.3\pm0.8$  eV b. A updated compilation [ADE97] resulted in a recommended  $S_{I7}(0)$  value of  $19_{-2}^{+4}$  eV b. A comparison of  $S_{I7}(0)$  values, grouped according to experimental approaches, is shown in Figure 9. As a result of an independent experimental method, our result agrees with results of other experiments. As can be seen from Figure 9, the results from the three kinds of experiment support the recent evaluation of [ADE97].

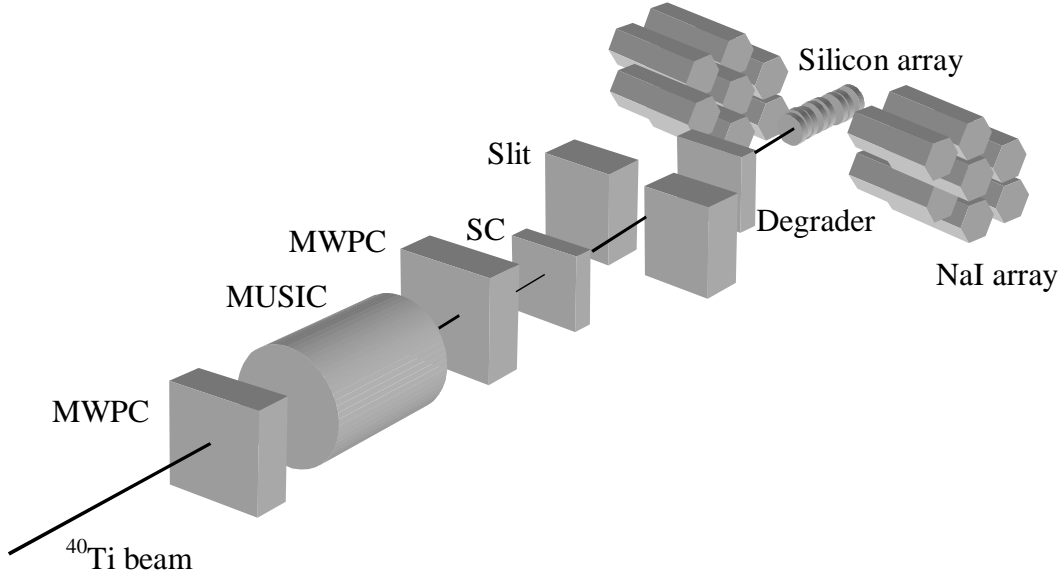
### 3. Beta-decay of $^{40}\text{Ti}$ and $^{41}\text{Ti}$ and implication for solar-neutrino detection

#### 3.1 Experimental Techniques

##### 3.1.1 Production and separation of $^{40}\text{Ti}$

A  $^{58}\text{Ni}$  beam of 500-A MeV with an intensity of  $1 \times 10^9$  ions/s from the heavy-ion synchrotron SIS at GSI in Darmstadt was used to produce  $^{40}\text{Ti}$  by fragmentation reactions in a  $4 \text{ g/cm}^2$  thick  $^9\text{Be}$  target. The secondary  $^{40}\text{Ti}$  beam was isotopically separated by using the projectile fragment separator FRS [GEI92]. The FRS was operated with two degraders at the first and intermediate focal plane ( $F_1$  and  $F_2$ ), respectively to achieve both a more narrow range profile and higher purity of the  $^{40}\text{Ti}$  beam with respect to contaminating secondary beams, in particular  $\beta$ -delayed proton emitters such as  $^{41}\text{Ti}$ . By inserting a degrader at  $F_1$ , the ratio of  $^{40}\text{Ti}$  to  $^{41}\text{Ti}$  was improved from 10 to 100. The intensity of the  $^{40}\text{Ti}$  beam at the final focus ( $F_4$ ) of the FRS was measured to be about one atom per minute. During the experiment of 5 days, about  $1.1 \times 10^4$   $^{40}\text{Ti}$  ions were produced. The experimental setup is sketched in Figure 1. The  $^{40}\text{Ti}$  ions were identified by energy-loss ( $\Delta E$ ) and mass-to-charge ratio ( $A/q$ ).  $\Delta E$  was determined by means of a multiple sampling ionization chamber (MUSIC), and  $A/q$  by measurements of the time-of-flight (TOF) and the magnetic rigidity of the FRS. The TOF was determined by using two scintillation counters (SC) positioned at  $F_2$  and  $F_4$ , respectively, and corrected by the position information ( $X/Y$ ) measured by means of two multi-wire proportional chambers (MWPC). Figure 2 shows a scatter plot of events on a  $\Delta E$  versus  $A/q$  plane.

Figure 1: Sketch of the detector set-up at the intermediate and final focal plane of the FRS, see text for details.



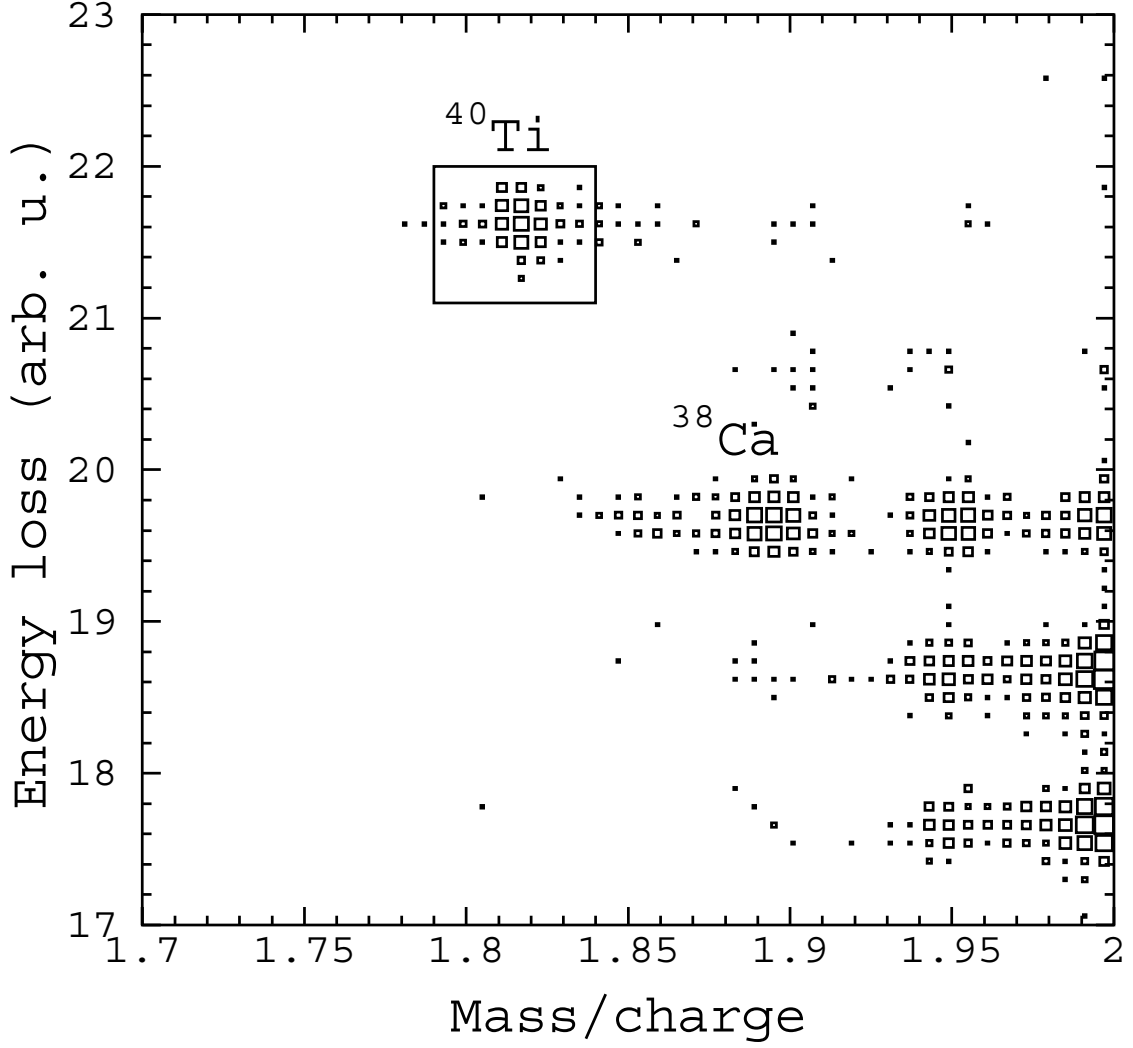


Figure 2: Energy-loss versus mass-to-charge scatter plot for the  $^{40}\text{Ti}$  data set. The locations of  $^{40}\text{Ti}$  and  $^{38}\text{Ca}$  ions are indicated. A frame marks the  $^{40}\text{Ti}$  events, used in the data evaluation.

### 3.1.2 Implantation and detection of protons, $\gamma$ -rays and proton- $\gamma$ coincidence

As shown in Figure 1, the  $^{40}\text{Ti}$  beam was collimated by a slit of  $\pm 5$  cm aperture in the dispersive dimension. The slit, in combination with the trigger signal derived from the implantation detector (see below), should in principle restrict the  $A/q$  values to a range between 1.75 and 1.89. However, due to the low-energy tail in the fragment energy distribution, a sizable amount of contaminating ions was also transmitted to the implantation detectors. Fortunately, the influence of other positron or  $\beta$ -delayed proton emitting contaminants was small, since the most intense secondary beams reaching  $F_4$  were stable isotopes (see Figure 2). Such contaminants were further rejected by a delayed-coincidence between the identified  $^{40}\text{Ti}$  events and time-correlated decay events, as described in Section 3.2.1. The  $^{40}\text{Ti}$  beam was slowed down at  $F_4$  from 140-A MeV to 60-A MeV by using a 1.14 g/cm<sup>2</sup> thick aluminum degrader. This measure was taken in order to shift the implantation profile to the center of the silicon detector stack consisting of eight 300  $\mu\text{m}$  thick, 30 mm diameter silicon detectors. The three central counters were used to measure positrons and  $\beta$ -delayed protons, whereas the outer ones served as veto detectors to reject unwanted particles as described below.

About 90 % of the  $^{40}\text{Ti}$  ions arriving at  $F_4$  were implanted in the central three counters. The measured range profile, shown in Figure 3, has a full-width at half maximum of about 630  $\mu\text{m}$ . The signals of each silicon detector, stemming from passage/implantation of heavy ions, or from positron or proton decays, were processed by a common pre-amplifier. Low-gain and high-gain main amplifiers were used to take the different energy ranges into account, which were 100-1000 MeV and 0-10 MeV, respectively. A time generator allowed to record the arrival time of each event for determining the decay half-life.

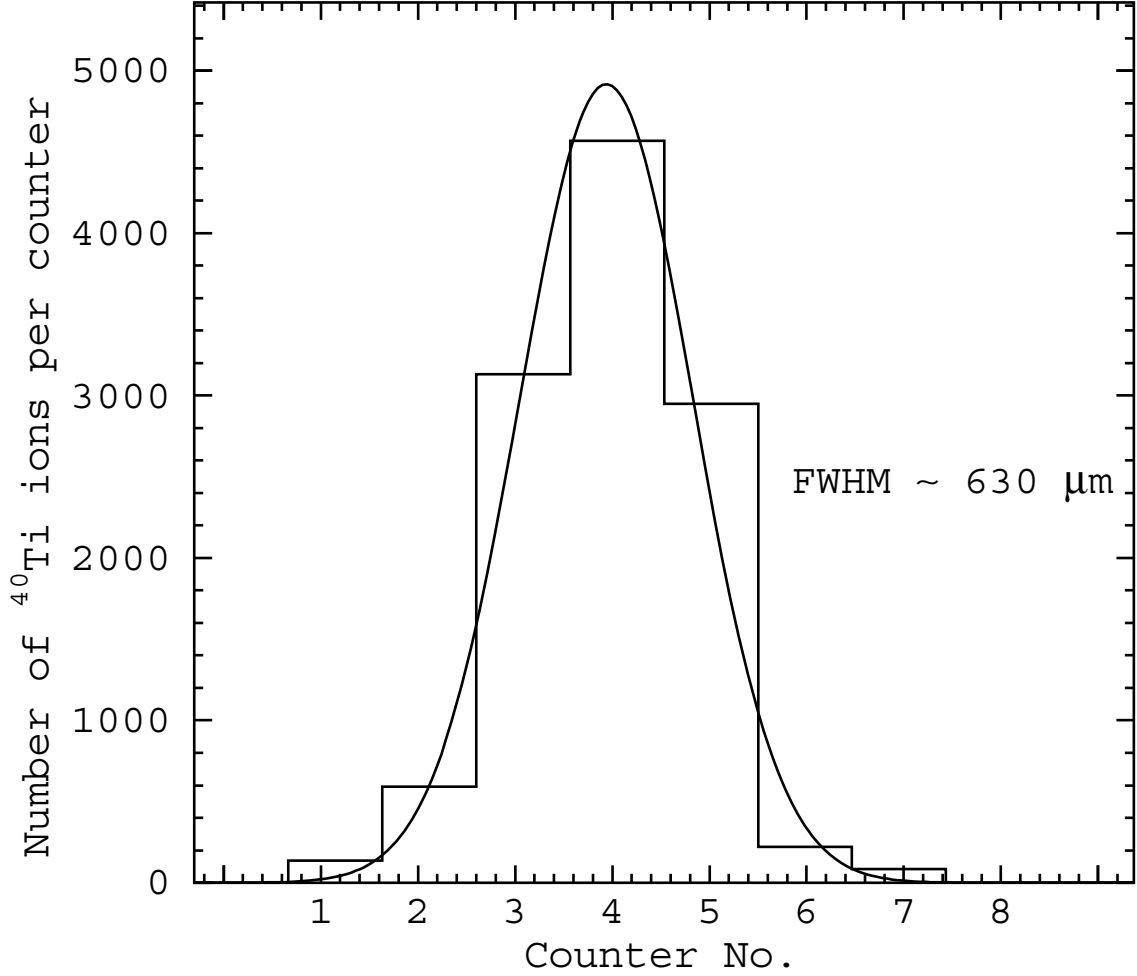


Figure 3: Range profile of the  $^{40}\text{Ti}$  ions implanted into the silicon detectors. The thickness of each silicon detector was 300  $\mu\text{m}$ . The experimental data are shown as a histogram with a Gaussian-fit superimposed.

An array of 14 large-volume Crystal Ball NaI detectors [MET86] was mounted close to the silicon detector stack to measure  $\gamma$ -rays emitted in the  $^{40}\text{Ti}$  or  $^{41}\text{Ti}$  decay processes. The NaI detectors were selected due to their higher photo-peak efficiencies compared to standard germanium detectors.

### 3.1.3 Energy and efficiency calibration of the detectors

The energy and efficiency calibration of the NaI array was obtained by using standard calibration sources. The photopeak efficiency was measured to be 15(2) % at 1.33 MeV, which is an order of magnitude higher than that obtained by using two large-

volume germanium detectors in previous FRS experiments [TRI97A]. The details of efficiency measurement for NaI detectors are presented in Appendix 4.

The proton-energy ( $E_p$ ) calibration has to take into account the pulse-height defect [PIE94] of the  $^{39}\text{Ca}$  recoil atoms ( $^{40}\text{Ti} \rightarrow ^{40}\text{Sc} \rightarrow ^{39}\text{Ca}$ ) and the line shifts caused by the summation between  $\beta$ -ray energy loss and proton signals. To address this problem, we performed the energy calibration of the silicon detectors by implanting the known  $\beta$ -delayed proton emitter  $^{41}\text{Ti}$  [HON97] in a separate experiment, with the FRS being optimized for this isotope. The difference in the line-shifts occurring in the  $\beta$ -delayed proton spectra of  $^{40}\text{Ti}$  and  $^{41}\text{Ti}$  is negligible [TRI95C].

A first rough energy calibration of the silicon detectors was obtained by using an  $\alpha$ -source and a pulse generator. This calibration was then improved on the basis of the  $\beta$ -delayed proton spectrum of  $^{41}\text{Ti}$ . The resultant uncertainty of  $E_p$  amounts to 10-15 keV for the major peaks. The detection efficiencies for the silicon detectors were determined from experimental data, from a Monte-Carlo simulation, and from a simple analytical calculation (see Appendix 5 for detail), and will be discussed below.

## 3.2 Data analysis

### 3.2.1 Event selection

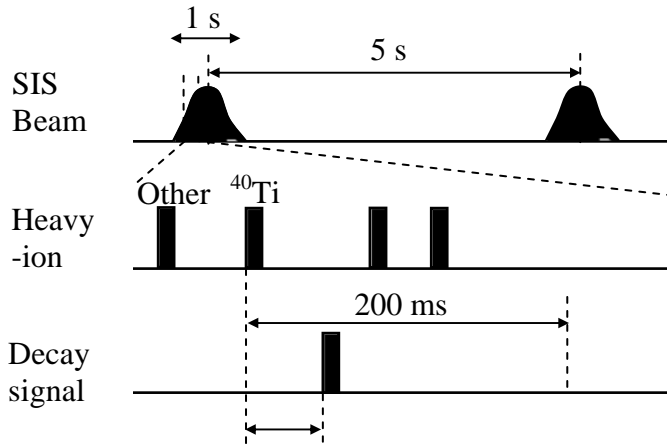


Figure 4: Schematic diagram of decayed coincidence between  $^{40}\text{Ti}$  events and decay events.

The delayed-coincidence technique, used in the off-line data analysis of the  $^{40}\text{Ti}$  data, was based on a time window of 200 ms. This window was opened by a  $^{40}\text{Ti}$  event, selected according to conditions with respect to  $\Delta E$  and  $A/q$  (see Figure 2), and closed by the subsequent decay event, as illustrated in Figure 4. Those selections are illustrated in the flow-charts Figure 5 and Figure 6. In this way, decay events from positron and/or  $\beta$ -delayed proton emitters (e.g.  $^{38}\text{Ca}$ , see Figure 2) were rejected. The decay events selected contained proton and  $\gamma$ -ray energy information. The  $E_p$  spectra were generated by an anti-coincidence condition with the front and rear silicon counters in order to eliminate heavy ions, which were implanted into the first counter or penetrated through all of them. The proton events, which were not completely stopped in a single detector, were rejected by an anti-coincidence condition with adjacent counters. The identification of the implantation of  $^{40}\text{Ti}$  ions in any of the three central detectors was also used to select only those decay signals that were recorded in the

relevant counter. This condition rejected the  $\beta$ -background stemming from contaminants implanted in neighboring detectors. The analysis of the  $^{41}\text{Ti}$  data was performed in a similar way, with the implantation-decay window being 300 ms.

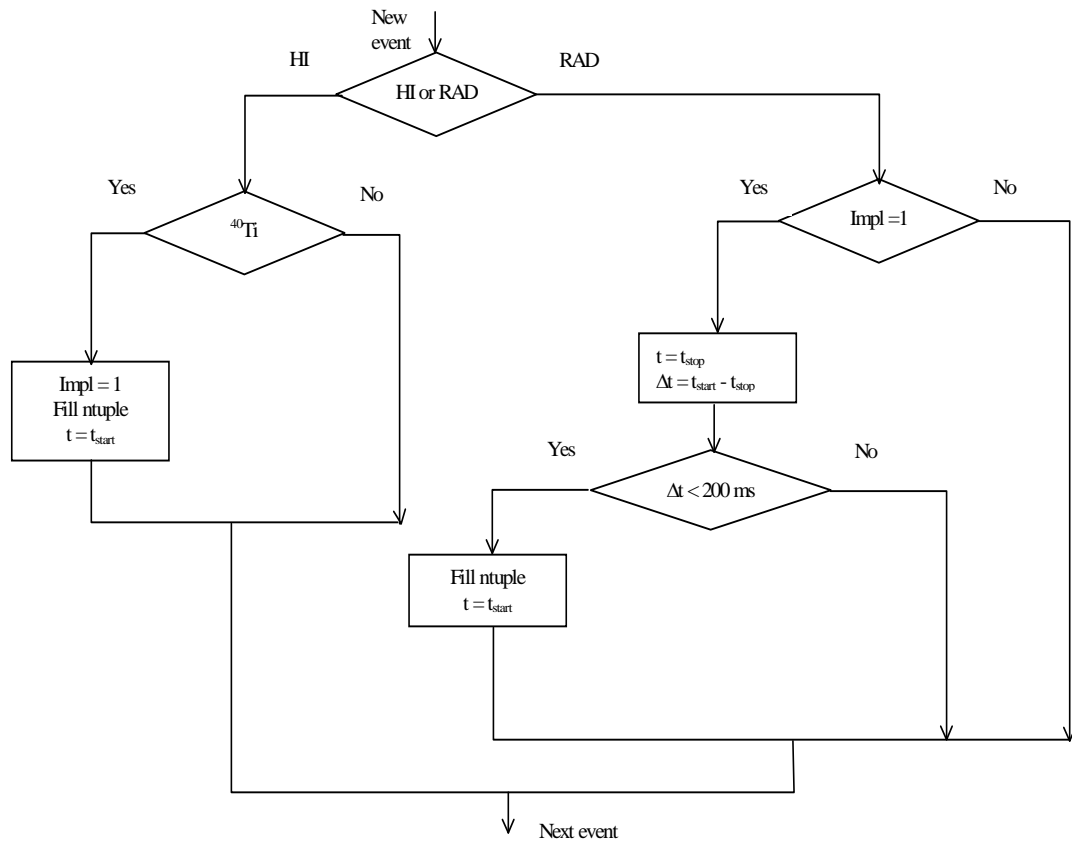


Figure 5: The first selection of events based on the particle identification and delayed-coincidence.

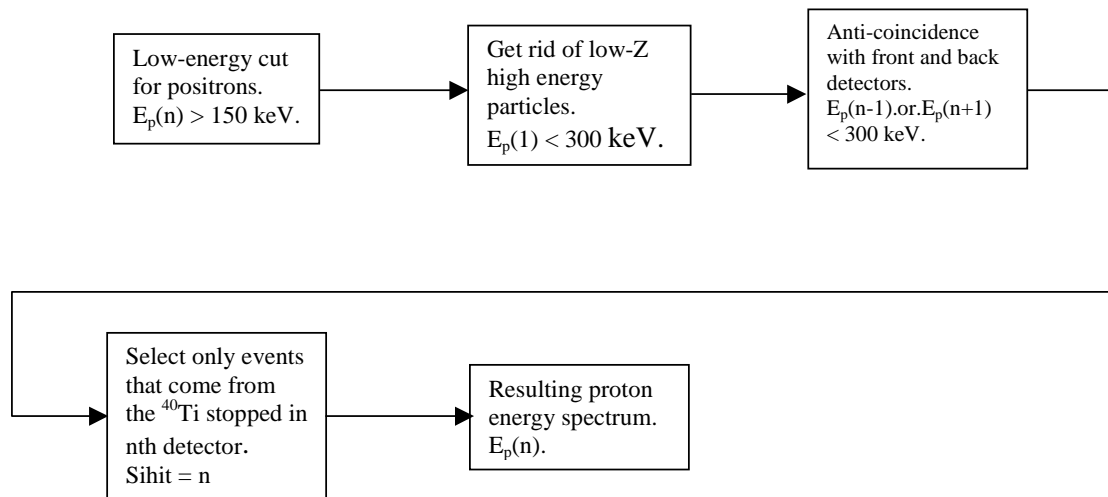


Figure 6: The second selection of proton-decay events in nth silicon detector based on the coincidence condition between silicon detectors.

### 3.2.2 Proton spectra

The  $E_p$  spectra obtained from the three central silicon counters were used to extract the intensities of individual proton transitions ( $I_p$ ). Figure 7 and Figure 8 show the  $E_p$  spectra obtained for  $^{40}\text{Ti}$  and  $^{41}\text{Ti}$ , respectively. The  $I_p$  values of major peaks were determined by adding the contribution from the central part and from the low-energy and high-energy tails of the lines. The proton peak shape function used in this procedure was established by using the major proton peaks as well as by a Monte-Carlo simulation. The  $I_p$  values of small peaks or 'energy groups' were obtained by simply determining, after subtraction of the background from the major peaks, the number of events in consecutive proton energy intervals. This procedure was based on the assumption of a minimum number of proton energy groups to account for the observed intensity. A typical peak fitting procedure is shown in Figure 9. As will further be discussed below, the  $E_p$  and  $I_p$  values for weak proton energy groups have large uncertainties due to the poor counting statistics, the poor resolution, and the inferior full-energy detection efficiency described below.



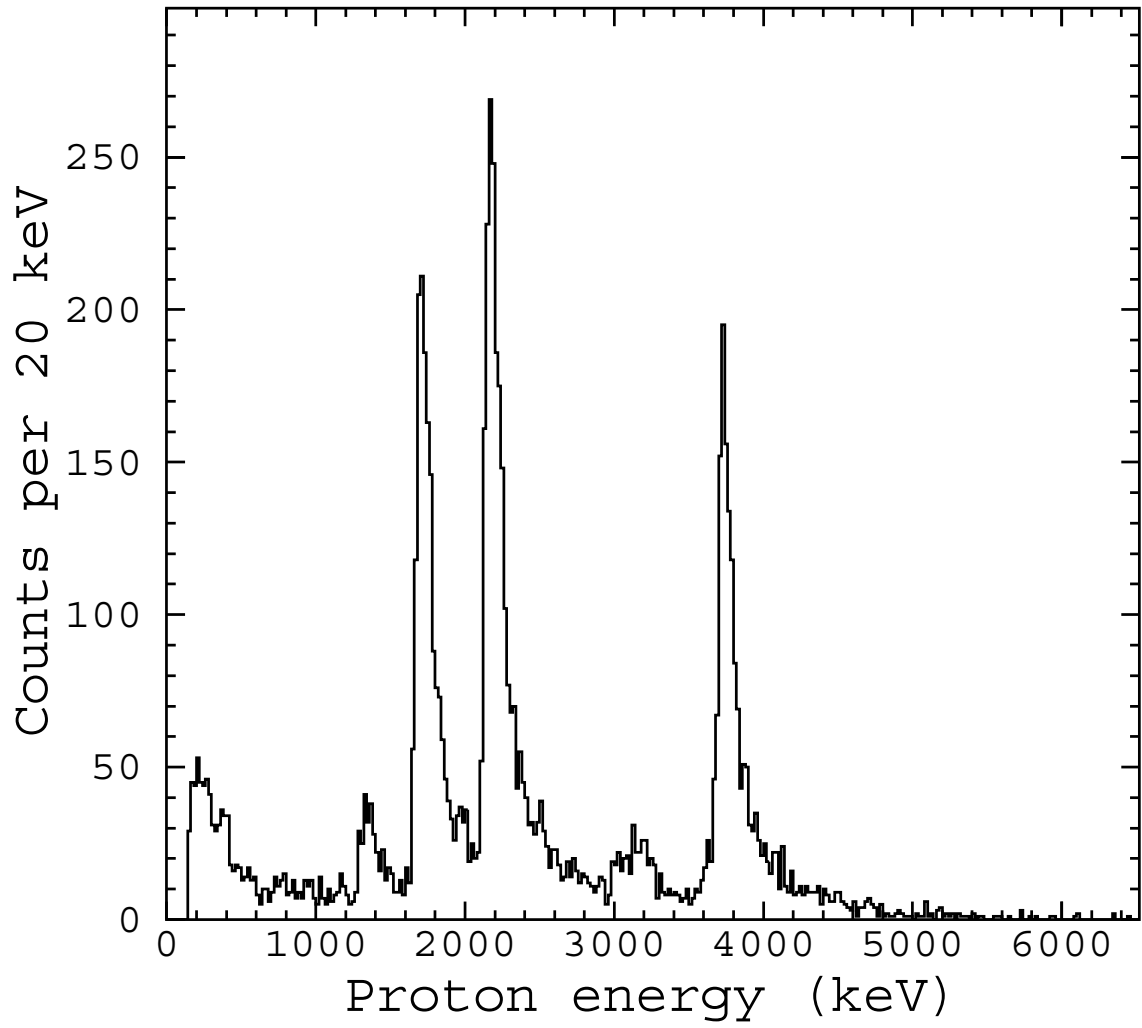


Figure 7: Energy spectrum, recorded in the central three silicon detectors, of  $\beta$ -delayed protons measured for the decay of  $^{40}\text{Ti}$ .

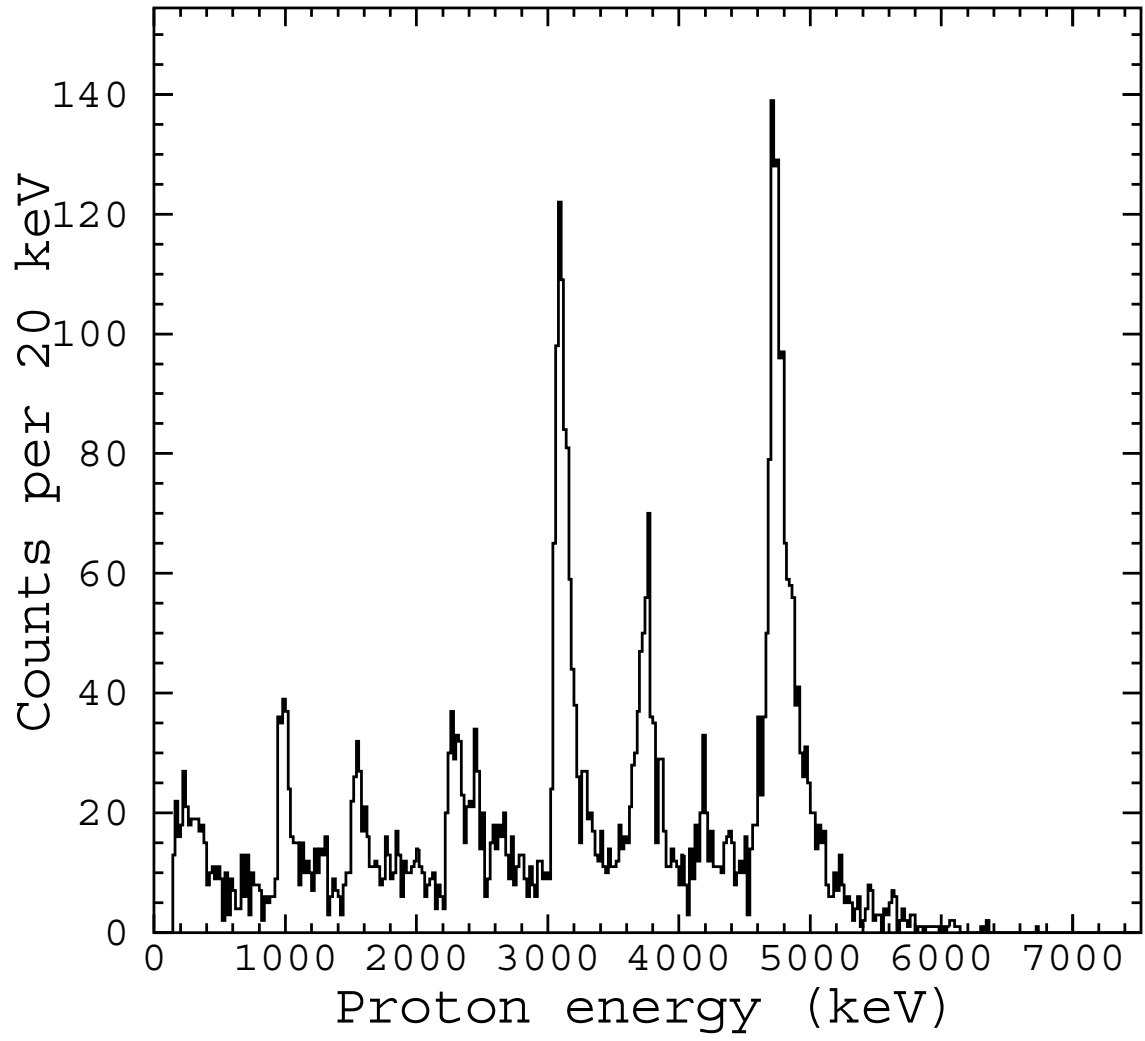


Figure 8: Energy spectrum of  $\beta$ -delayed protons measured for the decay of  $^{41}\text{Ti}$ .

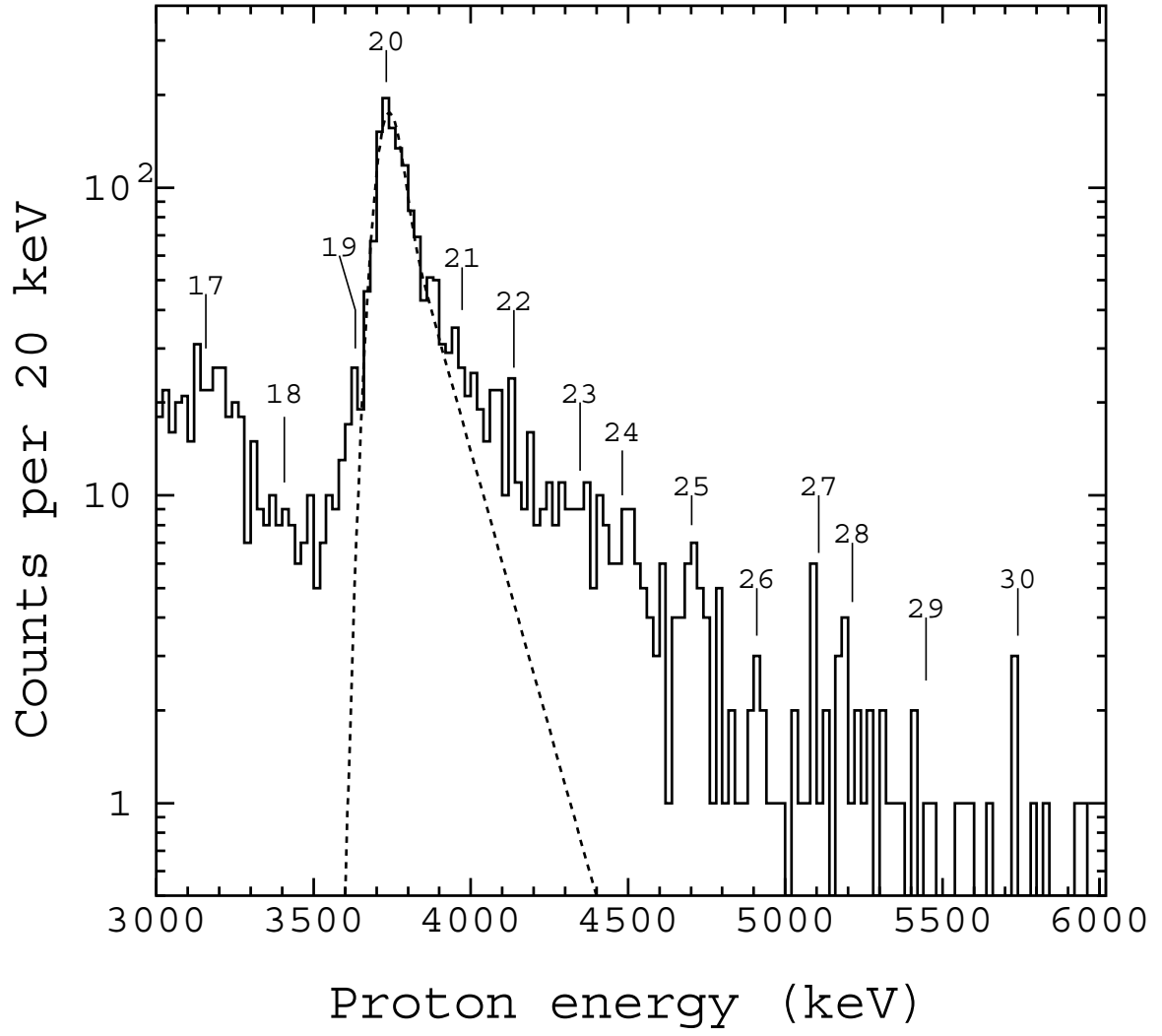


Figure 9: Section of the energy spectrum of  $\beta$ -delayed protons measured for the decay of  $^{40}\text{Ti}$ . The fit of the 3731 keV line is shown as a dashed curve. The individual proton energy groups are marked according to Table 1.

Table 1: Energies  $E_p$  and branching ratios  $b_p$  of  $\beta$ -delayed protons for the decay of  $^{40}\text{Ti}$ . The uncertainties of  $E_p$  have been increased by a factor of 2 for  $b_p \leq 1.43\%$ , see text for details.

Peak no.	This work		Trinder <i>et al.</i>	
	$E_p$ (keV)	$b_p$ (%)	$E_p$ (keV)	$b_p$ (%)
1	242(80) <sup>a</sup>	1.32(40)		
2	400(60) <sup>a</sup>	0.7(30)		
3	759(60) <sup>a</sup>	0.77(43)	709(25)	0.34(10)
4	951(86) <sup>b</sup>	0.8(32)		
5	1157(60)	0.77(42)	1105(26)	0.31(11)
6	1322(25) <sup>a</sup>	4.35(82)	1322(9)	3.46(25)
7	1580(40) <sup>a</sup>	0.4(20)	1574(28)	0.45(12)
8	1705(10)	22.5(21)	1698(9)	24.9(70)
9	1992(40) <sup>a</sup>	0.95(43)	1957(79)	1.3(20)
10	2167(10)	28.5(19)	2159(10)	29.4(14)
11	2366(40)	0.6(18)	2355(35)	0.86(22)
12	2518(46)	1.01(56)	2481(26)	1.6(30)
13	2609(60)	1.05(42)		
14	2733(40)	1.6(11)	2708(31)	1.6(30)
15	2907(40)	0.69(28)	2902(31)	1.3(30)
16	3045(40)	1.43(78)	3046(23)	1.8(30)
17	3158(27)	3.4(16)	3153(20)	2.9(40)
18	3407(88)	0.57(30)	3428(35)	1.1(20)
19	3632(46)	1.09(27)	3633(21)	0.99(18)
20	3731(10)	22.8(19)	3733(12)	21.8(15)
21	3972(100)	1.4(42)	3890(33)	1.4(30)
22	4137(60)	1.27(53)	4015(32)	1.5(40)
23	4347(74)	0.97(40)	4353(99)	2(1)
24	4481(88)	0.73(22)		
25	4702(60)	0.55(21)		
26	4909(40)	0.16(10)	4951(60)	0.63(20)
27	5107(60)	0.41(30)		
28	5213(80)	0.3(12)		
29	5448(60)	0.18(10)	5308(33)	0.68(20)
30	5740(60)	0.11(6)		

<sup>a</sup>Transition feeding the 2469 keV state in  $^{39}\text{Ca}$ .

<sup>b</sup>Transition feeding the 3026 keV state in  $^{39}\text{Ca}$ .

To improve the energy resolution, a range selection method was applied. It consisted of selecting those events that corresponded to  $^{40}\text{Ti}$  atoms stopped in the central 100  $\mu\text{m}$  thick layer of one of the three central silicon detectors. This was accomplished by comparing the measured residual energy of  $^{40}\text{Ti}$  ions with range-energy relation [SCH]. As can be seen by comparing Figure 7 and Figure 10, the proton energy resolution was improved by this method from 100 keV to 70 keV at a proton energy of 3.7 MeV. This improvement has to be confronted by a loss of about 2/3 of the total events as a result of such selection.

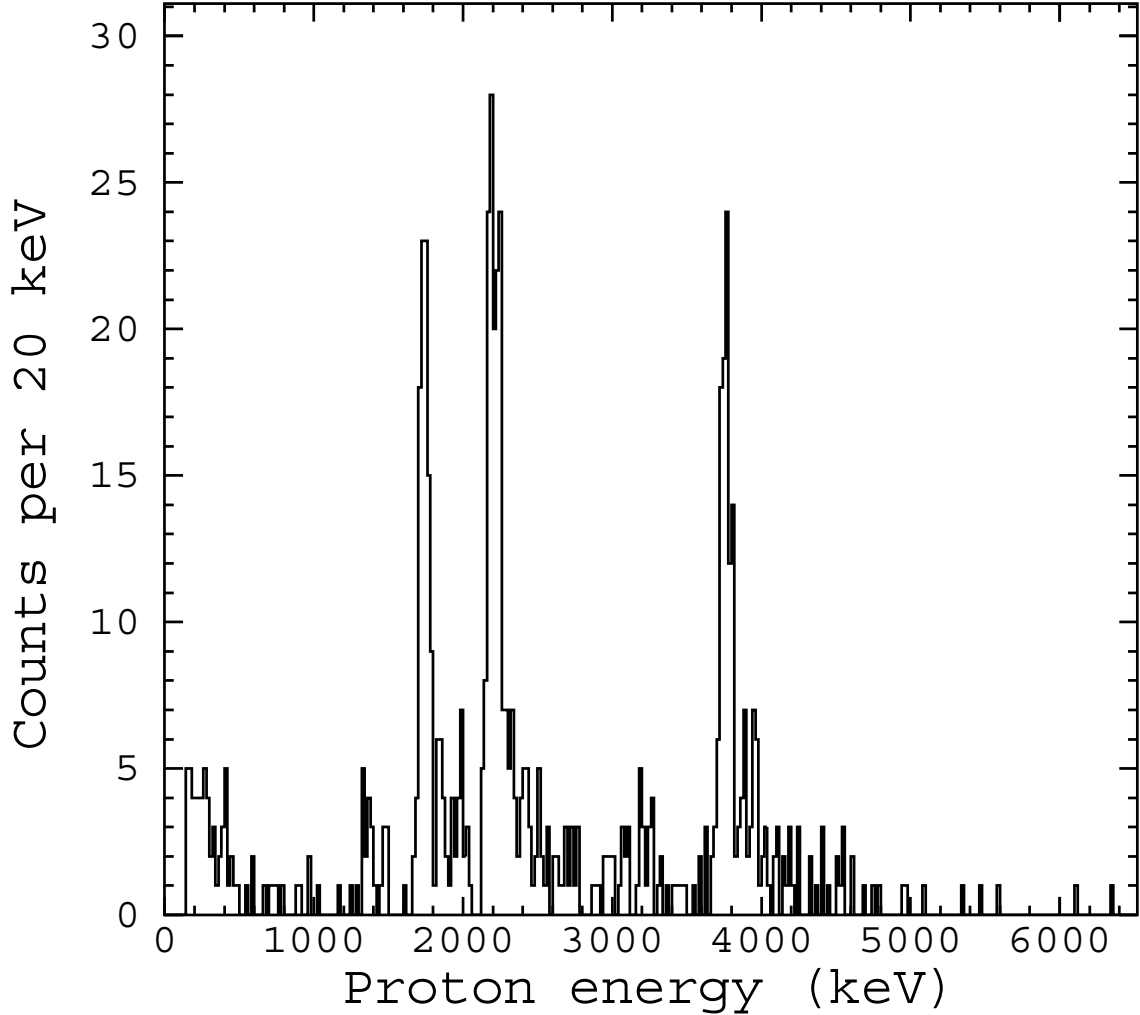


Figure 10: Proton energy spectrum recorded in one of the silicon detectors under the restriction that  $^{40}\text{Ti}$  ions are implanted into the central 100  $\mu\text{m}$  thick silicon layer.

The  $E_p$  data presented in Table 1 and Table 2 were mainly extracted from the proton energy spectra displayed in Figure 7 and Figure 8, the range-selected data such as those displayed in Figure 9 serving as a reference. The  $E_p$  uncertainties were determined by taking into account the uncertainties of the energy calibration and the fitting procedure. However, for the small proton energy groups, these uncertainties may not be large enough to account for the uncertainties introduced by the simple minimum-number approach mentioned above. In an attempt to take this deficiency into account, we increased the uncertainties of the corresponding  $E_p$  data by a factor of 2. The energy groups, obtained in this way, do not necessarily correspond to individual levels

in  $^{40}\text{Sc}$  and  $^{41}\text{Sc}$ , respectively, but represent a sufficiently safe basis for determining  $B(GT)$  values.

The  $I_p$  values were corrected for the full-energy detection efficiency. The latter quantity was determined by selecting events recorded in coincidence between the adjacent counters. The experimental results obtained in this way are displayed in Figure 11, in comparison with results from a Monte-Carlo simulation [TRI] based on the proton stopping power in silicon. See also Appendix 4 for a presentation of an alternative method for determining this efficiency. To get the proton branching ratios ( $b_p$ ) for individual proton transitions, the  $I_p$  values were normalized to the total number of implanted  $^{40}\text{Ti}$  ions. The latter quantity was deduced from the  $\Delta E$  versus  $A/q$  data displayed in Figure 2, and corrected for the intensity loss due to secondary reactions in the energy degrader at  $F_4$  (See Sect. 3.1.2). This loss amounted to 13(3) %, which was determined experimentally by using the energy-loss and the residual energy measured for the heavy-ions in the silicon counters, as shown in Figure 12. This result is in good agreement with an estimate of 10 %, based on systematics of fragmentation cross-sections [SÜM90]. The final  $E_p$  and  $b_p$  values for  $^{40}\text{Ti}$  and  $^{41}\text{Ti}$ , listed in Table 1 and Table 2, respectively, represent weighted averages based on the results from different detectors and range selection conditions. The sum of individual  $b_p$  values for  $^{40}\text{Ti}$  and  $^{41}\text{Ti}$  amounts to 101(5) and 104(5) %, respectively. The agreement of these results with a value of 100 % yielded an integral proof for the consistency of the corrections concerning intensity losses and proton full-energy efficiency, and allowed also to determine a  $1\sigma$  limit of order of 5 % for the branching ratio of *unobserved*  $\beta$ -delayed protons from the decay of  $^{40}\text{Ti}$  and  $^{41}\text{Ti}$ , respectively. The same limit applies for  $\gamma$ -transitions in  $^{40}\text{Sc}$  and  $^{41}\text{Sc}$ , populated in  $\beta$ -decay. Table 1 and Table 2 list the  $E_p$  and  $b_p$  results from this work to literature data for  $^{40}\text{Ti}$  and  $^{41}\text{Ti}$ , respectively.

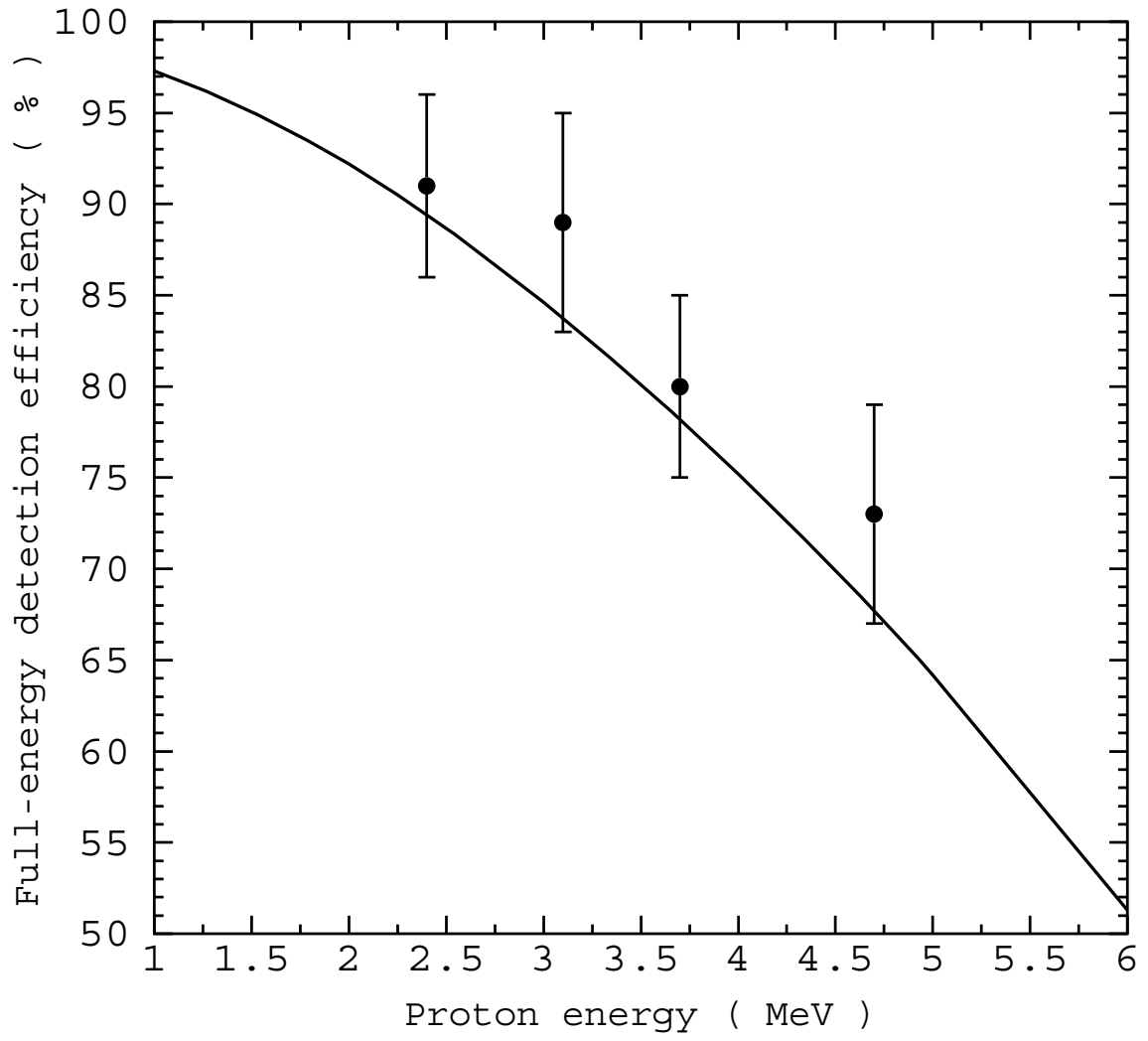


Figure 11: Full-energy detection efficiency deduced from the experimental data (full points) and from a Monte-Carlo simulation (solid line).

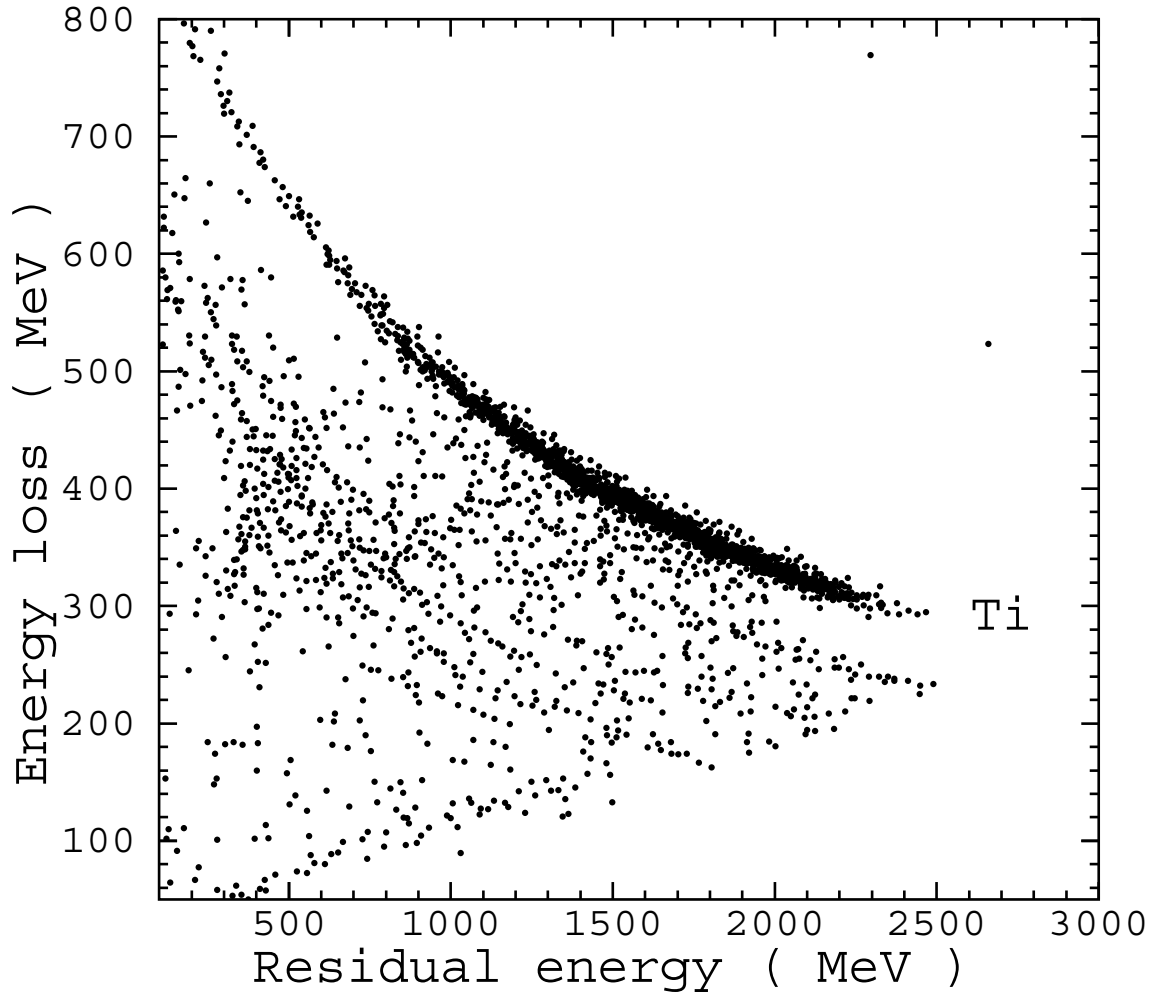


Figure 12: Energy-loss versus residual energy scatter plot of the  $^{40}\text{Ti}$  event observed after the energy degrader in the final focal plane of the FRS. The cluster of events, corresponding to titanium ions, is marked.



Table 2: Energies and relative branching ratios ( $b_p^{rel}$ ) of  $\beta$ -delayed protons observed for the decay of  $^{41}\text{Ti}$  from this work and from Refs. [HON97, SEX74, ZHO85]. The  $b_p^{rel}$  values from this work have to be multiplied by a factor 0.261 to yield absolute branching ratios  $b_p$ . The uncertainties of  $E_p$  have been increased by a factor of 2 for  $b_p^{rel} \leq 12.8$  %, i.e.  $b_p \leq 3.34$  %, see text for details.

This work		Honkanen <i>et al.</i>		Sextro <i>et al.</i> and Zhou <i>et al.</i>	
$E_p$ (keV)	$b_p^{rel}$ (%)	$E_p$ (keV)	$b_p^{rel}$ (%)	$E_p$ (keV)	$b_p^{rel}$ (%)
744(60)	4.3(14)	754(12)	1.1(5)		
976(30)	24.0(64)	986(1)	19.6(19)	1000(15)	38.6(24)
1272(70) <sup>a</sup>	5.0(15)			1248(15)	3.9(9)
1540(20)	20.8(21)	1542(2)	28.8(23)	1546(15)	21.6(7)
		1586(11)	4.0(9)		
1842(40) <sup>a</sup>	3.3(12)				
1987(60) <sup>a</sup>	5.2(13)	1981(12)	2.6(7)	1983(25)	3.1(6)
2111(42) <sup>a</sup>	3.3(7)			2063(30)	4.1(5)
2270(25)	21.0(57)	2270(0)	17.9(18)	2271(10)	26.1(3)
2440(40)	7.3(53)	2414(3)	8.3(12)	2409(20)	14.7(8)
2538(128)	2.5(5)				
2654(40)	7.3(32)	2650(12)	7.0(11)	2662(20)	8.1(5)
2817(46)	5.2(16)	2796(14)	2.1(6)	2814(15)	4.9(38)
3095(10)	67.3(73)	3083(5)	66.0(30)	3077(15)	60.3(11)
3295(40)	3.5(18)	3139(12)	2.8(6)	3148(20)	4.0(4)
		3330(13)	2.2(6)	3339(30)	2.3(4)
3452(70)	3.7(19)	3480(12)	2.1(6)	3487(20)	2.8(4)
3569(40)	5.1(21)	3598(6)	7.2(10)	3605(15)	9.7(4)
3647(50)	5.3(20)	3691(5)	17.8(16)	3590(15)	15.5(8)
3749(18)	39.0(40)	3749(5)	29.2(21)	3749(10)	31.0(20)
3857(40)	2.0(11)	3837(9)	3.4(8)	3836(25)	2.4(2)
4025(40)	2.0(7)	3888(11)	3.2(8)	3904(25)	1.5(2)
4192(20)	12.8(27)	4189(6)	13.1(14)	4187(15)	15.4(5)
		4298(13)	1.3(5)		
4376(40)	9.2(21)	4381(8)	6.0(9)	4379(15)	7.2(4)
4486(60)	4.9(20)	4564(20)	2.2(3)	4564(20)	2.2(3)
4625(66)	6.3(41)	4639(5)	19.1(17)	4638(10)	22.1(7)
		4684(11)	4.1(8)		
4727(16)	107(11) <sup>b</sup>	4736(4)	100	4734(4)	100.0
				4832(25)	3.0(3)
4883(60)	2.4(12)			4876(20)	3.4(4)
4976(40)	3.6(17)	4950	14(5)	4925(20)	2.9(3)
5093(40)	2.1(15)			5177(30)	1.5(3)
5219(40)	2.6(5)				
5364(60)	1.5(8)				
5451(60)	2.4(5)				
5658(40)	3.0(15)			5595(15)	0.26(3)
5736(40)	1.1(4)			5715(15)	0.36(6)
5889(94)	0.8(2)			5950(20)	0.40(3)
6082(60)	0.6(2)			6125(20)	0.29(2)
6359(60)	0.4(1)			6380(50)	0.20(3)
6725(60)	0.3(1)			6650(50)	0.20(2)

<sup>a</sup>Transition feeding the 3904 keV state in  $^{40}\text{Ca}$ .

<sup>b</sup>Due to the rather poor energy resolution of this work, the neighbouring 4684 and 4832 keV peaks,

observed by Honkanen et al. and Sextro et al., respectively, remain unresolved.

### 3.2.3 Proton- $\gamma$ coincidence data

The proton- $\gamma$  coincidence data were used for identifying proton emission from  $^{40,41}\text{Sc}$  levels to excited states of  $^{39,40}\text{Ca}$ . This information was used for deducing the  $\beta$ -branching ratios ( $b_\beta$ ) from the experimental  $b_p$  values. The resulting  $b_\beta$  data for  $^{40}\text{Ti}$  and  $^{41}\text{Ti}$  are listed, together with the individual proton decay modes, in Table 3 and Table 4. A typical proton- $\gamma$  coincidence pattern is shown in Figure 13, Figure 14 displays the  $\gamma$ -ray spectra measured in coincidence with 1322 and 2167 keV protons. As can be seen from Figure 13 and Figure 14, there is clear evidence for a proton transition between the 4365 keV isobaric analog state (IAS) in  $^{40}\text{Sc}$  and the 2469 keV State in  $^{41}\text{Ca}$ . A ratio of 12(3) % was found between the number of  $\gamma$ -gated events in the 1322 keV proton peak and the number of events observed for this peak in the ungated spectrum (see Figure 13). This value is in good agreement with the calibrated NaI photopeak efficiency of 13(3) % at 2.5 MeV (see Sect. 3.1.3). Correspondingly, the intensity of the 1322 keV proton line is assigned to a IAS $\rightarrow$ 2469 keV transition. The remaining  $^{40}\text{Ti}$  and  $^{41}\text{Ti}$  proton- $\gamma$  coincidence data were interpreted in a similar way.

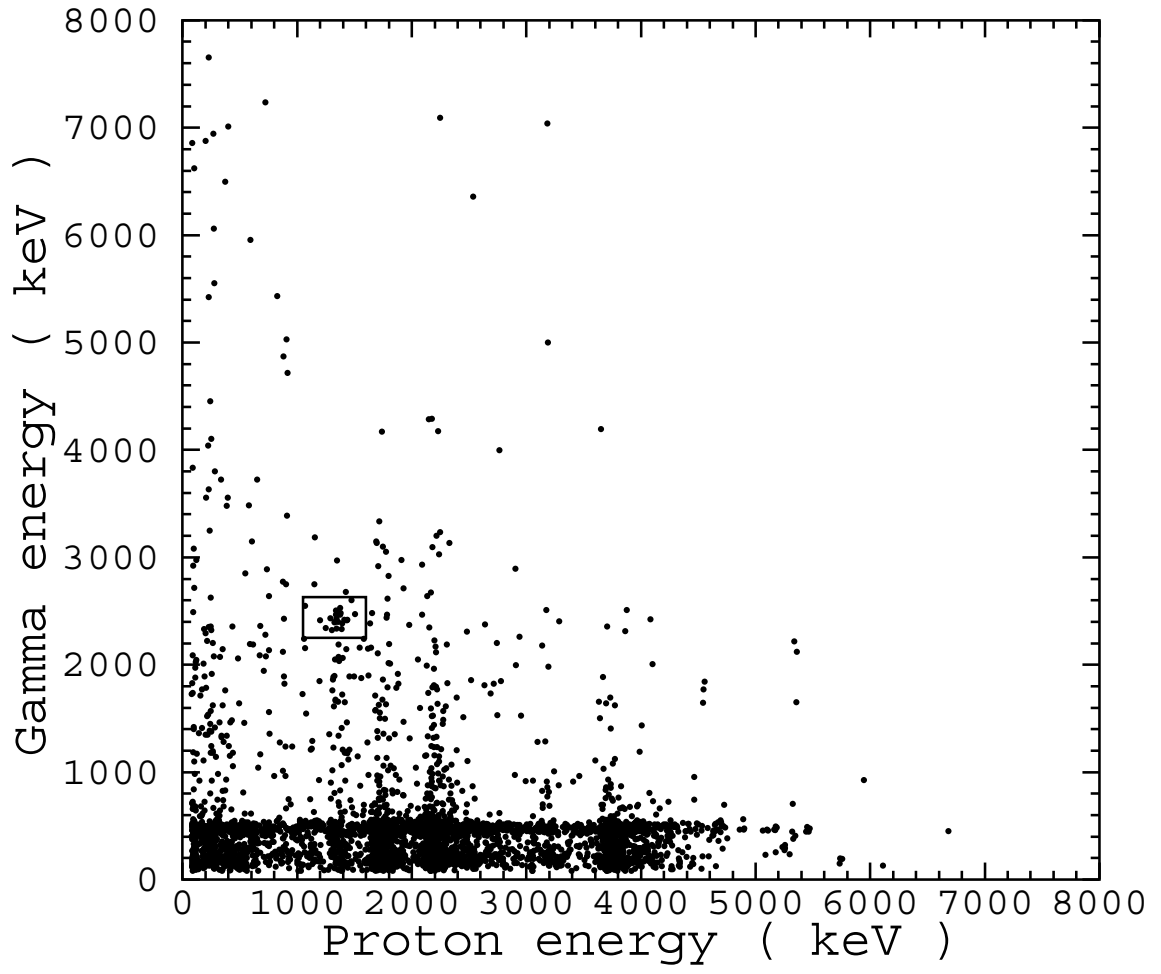


Figure 13: Scatter plot of the proton- $\gamma$  coincidence data obtained for  $^{40}\text{Ti}$ . The coincidence events between 1322 keV proton and 2469 keV  $\gamma$ -ray are marked by a frame.

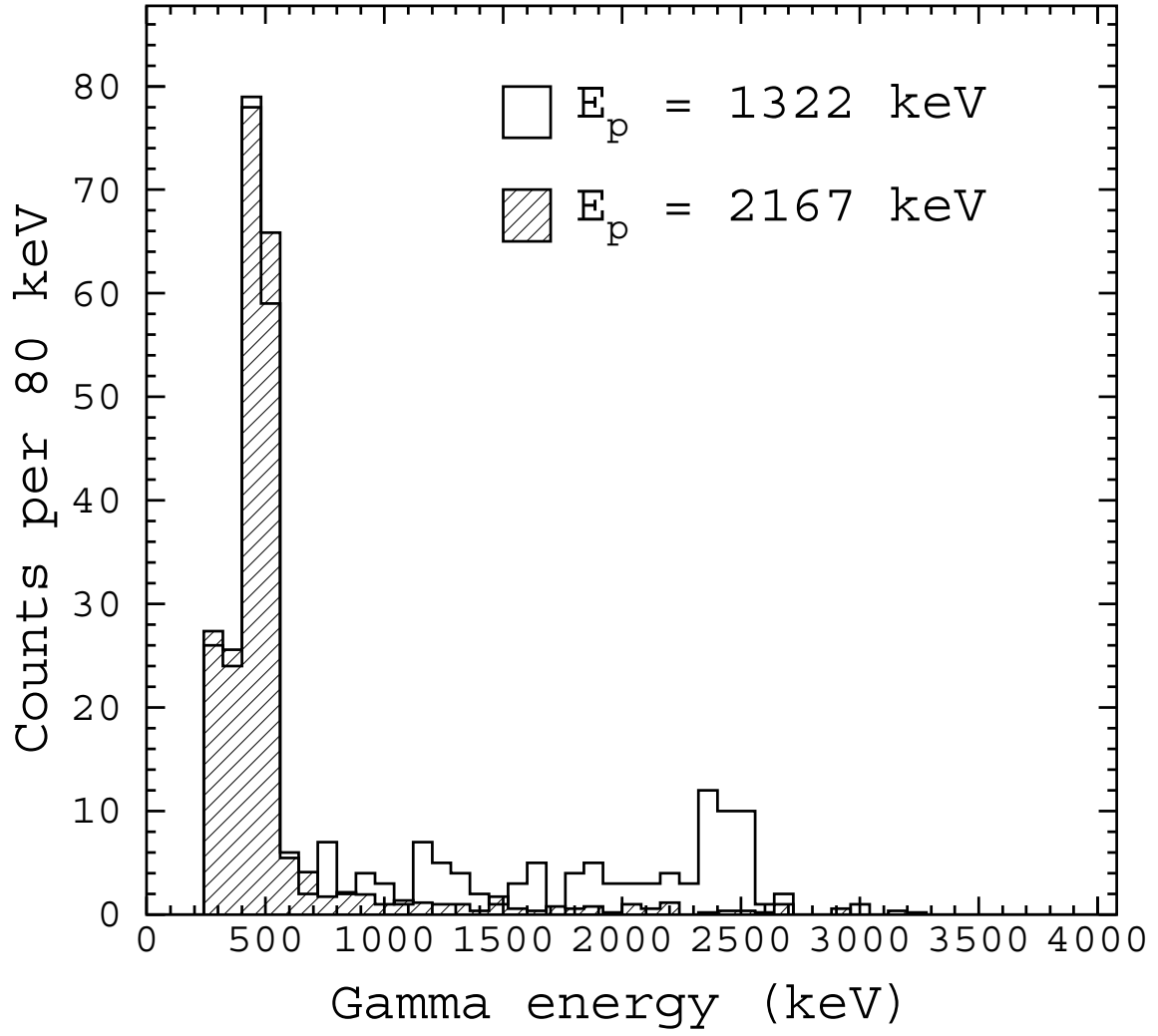


Figure 14: Gamma-ray spectrum measured in coincidence with 1322 keV proton events (open histogram), compared to that obtained in coincidence with 2167 keV proton events (hatched histogram). In the latter case, the intensity was scaled to match the number of counts in the 511 keV peak.

Table 3: Energies of excited levels in  $^{40}\text{Sc}$ ,  $\beta$ -branching ratios, and  $\beta$ -transition strengths for  $^{40}\text{Ti}$  decay, and  $^{40}\text{Ar}$  neutrino capture cross-sections deduced from the present data, in comparison with the results from other works.  $p_0$ ,  $p_1$ , and  $p_2$  denote proton transitions to the ground state, first excited state (2469 keV) and second excited state (3026 keV) of  $^{39}\text{Ca}$ , respectively.

$E_x(^{40}\text{Sc})$ (keV)	Decay mode	This work		$E_x(^{40}\text{K})$ (keV)	$\sigma_v$ ( $10^{-43}\text{cm}^2$ )	Trinder <i>et al.</i>		(p,n) data	
		$b_\beta$ (%)	$B(F)$ $+B(GT)$			$E_x(^{40}\text{Sc})$ (keV)	$B(F)$ $+B(GT)$	$E_x(^{40}\text{Sc})$ (keV)	$B(F)$ $+B(GT)$
2287(10)	$p_0$	22.5(21)	0.83(8)	2290	2.82(26)	2281(9)	0.96(3)	2280	1.23(24)
2761(10)	$p_0$	28.5(19)	1.40(10)	2730	3.80(26)	2753(11)	1.50(7)	2730	1.05(21)
2966(40)	$p_0$	0.60(18)	0.03(1)		0.080(24)	2955(35)	0.05(1)		
3121(46)	$p_0$	1.01(56)	0.06(3)	3110	0.138(77)	3084(26)	0.10(2)		
3235(50)	$p_0, p_1$	2.37(58)	0.16(4)		0.324(80)				
3342(40)	$p_0$	1.6(11)	0.11(8)	3376	0.21(14)	3317(31)	0.11(2)	3376	0.09(2)
3418(60)	$p_1$	0.70(30)	0.05(2)		0.097(42)				
3521(40)	$p_0$	0.69(28)	0.06(2)		0.096(39)	3515(31)	0.11(2)		
3662(40)	$p_0$	1.43(78)	0.13(7)		0.20(11)	3664(23)	0.16(3)		
3782(40)	$p_0, p_1$	4.2(17)	0.40(16)	3739	0.61(24)	3758(20)	0.32(5)	3830	0.28(6)
4033(88)	$p_0$	0.57(30)	0.07(4)		0.081(44)	4055(35)	0.14(3)		
4194(60)	$p_1$	0.77(42)	0.10(6)		0.111(61)	4141(26)	0.04(1)		
4264(46)	$p_0$	1.09(27)	0.15(4)		0.158(39)	4265(22)	0.14(3)		
4365(10)	$p_0, p_1$	27.1(21)	4.01(31)	4384	3.87(30)			4380	0.71(35) <sup>a</sup>
4540(86)	$p_2$	0.80(32)	0.14(5)		0.116(46)	4528(33)	0.24(6)		
4628(40)	$p_0, p_1$	1.80(47)	0.33(9)		0.262(68)	4637(29)	0.38(8)		
4782(60)	$p_0$	1.27(53)	0.26(11)	4789	0.183(77)			4760	0.30(6)
4997(72)	$p_0$	0.97(40)	0.24(10)		0.140(58)				
5051(40)	$p_1$	0.95(43)	0.25(11)		0.137(63)	5003(99)	0.90(30)		
5135(86)	$p_0$	0.73(22)	0.20(6)		0.105(32)			5160	0.33(7)
5362(60)	$p_0$	0.55(21)	0.19(7)		0.077(30)				
5574(40)	$p_0$	0.16(10)	0.07(4)		0.022(14)	5617(61)	0.28(9)		
5777(60)	$p_0$	0.41(30)	0.21(15)		0.054(40)			5700	0.07(1)
5886(60)	$p_0$	0.30(12)	0.17(7)		0.038(15)				
6126(60)	$p_0$	0.18(10)	0.13(7)		0.022(13)	5983(33)	0.44(13)	6110	0.26(5)
6426(60)	$p_0$	0.11(6)	0.11(6)		0.012(6)				

<sup>a</sup>There appears to be some significant GT strength admixed to the Fermi transition.

Table 4: Energies of excited levels in  $^{41}\text{Sc}$  and their spins and parities,  $\beta$ -branching ratios,  $\beta$ -transition strengths deduced from this work, in comparison with other works.  $p_0$  and  $p_1$  denote proton transitions to the ground state and first excited state (3904 keV) of  $^{40}\text{Ca}$ , respectively.

$Ex(^{41}\text{Sc})^a$ (keV)	$J^\pi$	This work			Honkenen <i>et al.</i>	
		decay	$b_\beta$ (%)	$B(F) + B(GT)$	$Ex(^{41}\text{Sc})$ (keV)	$B(F) + B(GT)$
2095.9(5)	$3/2^+$	$p_0$	6.3(17)	0.06(2)	2095.9(5)	0.057(12)
2666.60(7)	$5/2^+$	$p_0$	5.4(6)	0.07(1)	2666.60(7)	0.108(21)
	$1/2^+$				2719.12(9)	0.016(5)
3411.4(4)	$1/2^+$	$p_0$	5.5(15)	0.11(3)	3411.4(4)	0.097(12)
3562.6(3)	$1/2^+, 3/2^+, 5/2^+$	$p_0$	1.9(14)	0.04(3)	3562.6(3)	0.049(9)
3687(40)	$1/2^+, 3/2^+, 5/2^+$	$p_0$	0.7(1)	0.014(3)		
3780.6(2)	$5/2^+$	$p_0$	1.9(8)	0.05(2)	3781(0)	0.047(9)
3971(15)	$1/2^+, 3/2^+, 5/2^+$	$p_0$	1.4(4)	0.04(1)	3951(14)	0.015(5)
4245(4)	$5/2^+$	$p_0$	17.6(19)	0.58(7)	4245(4)	0.580(50)
	$5/2^+$				4328(3)	0.026(7)
4502(5)	$3/2^+$	$p_0$	0.9(5)	0.04(2)	4502(5)	0.023(7)
4661(2)	$1/2^+, 3/2^+, 5/2^+$	$p_0$	1.0(5)	0.04(2)	4644(5)	0.024(7)
4777(5)	$3/2^+$	$p_0$	1.3(6)	0.06(3)	4777(5)	0.090(15)
4869(4)	$5/2^+$	$p_0$	1.4(5)	0.07(3)	4869(4)	0.240(30)
4947(5)	$5/2^+$	$p_0$	10.2(10)	0.53(6)	4928(5)	0.400(40)
5023(5)	$1/2^+$	$p_0$	0.5(3)	0.03(2)	5023(5)	0.050(13)
	$3/2^+$				5084(5)	0.049(13)
5210(40)	$1/2^+, 3/2^+, 5/2^+$	$p_0$	0.5(2)	0.03(1)		
5375(5)	$5/2^+$	$p_0$	3.3(7)	0.23(5)	5375(5)	0.250(30)
	$1/2^+$				5493(5)	0.027(11)
5576(4)	$3/2^+, 5/2^+$	$p_0$	2.4(6)	0.19(5)	5576(4)	0.130(30)
5683(60)	$1/2^+, 3/2^+, 5/2^+$	$p_0$	1.3(5)	0.11(5)		
5774(4)	$1/2^+, 3/2^+, 5/2^+$	$p_1$	1.1(4)	0.11(3)	5774(4)	0.110(30)
5863(5)	$5/2^+$	$i$	1.6(11)	0.16(11)	5840(5)	0.510(60)
5886(12)	$1/2^+, 3/2^+, 5/2^+$	$p_0$	0.9(5) <sup>b</sup>	0.09(5)	5886(12)	0.110(30)
5939(4)	$3/2^+$	$p_0$	26.1(29)	2.77(34)	5939(4)	2.87(22)
6038(25)	$1/2^+, 3/2^+, 5/2^+$	$p_0$	0.9(5) <sup>b</sup>	0.10(6)	6038(25)	0.81(11) <sup>c</sup>
6090(60)	$1/2^+, 3/2^+, 5/2^+$	$p_0$	0.6(3)	0.08(4)	6083(20)	0.096(13)
6185(40)	$1/2^+, 3/2^+, 5/2^+$	$p_0$	0.9(5)	0.12(6)	6133(20)	0.085(11)
6299(40)	$1/2^+, 3/2^+, 5/2^+$	$p_0, p_1$	1.9(6)	0.26(8)	6391(30)	0.054(13)
6435(40)	$1/2^+, 3/2^+, 5/2^+$	$p_0$	0.7(1)	0.11(2)	6468(12)	0.120(40)
6583(60)	$1/2^+, 3/2^+, 5/2^+$	$p_0$	0.4(2)	0.07(4)		
6672(40)	$1/2^+, 3/2^+, 5/2^+$	$p_0$	0.6(1)	0.12(3)		
6881(28)	$5/2^+$	$p_0, p_1$	1.7(5)	0.39(12)	6820(15)	0.016(2)
6964(40)	$1/2^+, 3/2^+, 5/2^+$	$p_0$	0.3(1)	0.07(3)	6942(15)	0.024(3)
7026(60)	$1/2^+, 3/2^+, 5/2^+$	$p_1$	1.4(3)	0.37(9)		
7137(52)	$1/2^+, 3/2^+, 5/2^+$	$p_0, p_1$	1.1(2)	0.33(6)	7180(20)	0.034(5)
7319(60)	$1/2^+, 3/2^+, 5/2^+$	$p_0$	0.17(5)	0.06(2)	7360(20)	0.029(3)
7603(60)	$1/2^+, 3/2^+, 5/2^+$	$p_0$	0.11(2)	0.05(1)	7630(50)	0.027(5)
7978(60)	$1/2^+, 3/2^+, 5/2^+$	$p_0$	0.07(3)	0.05(2)	7900(50)	0.037(5)

<sup>a</sup>Adapted best values either from this work or from Ref. [HON97].

<sup>b</sup>Decomposed using the information from Ref. [HON97].

<sup>c</sup>Most probably misprinted in Ref., was calculated to be 0.081(11) according to the  $b_\beta$  value in Ref. [HON97].

By demanding NaI events in coincidence with positrons, i.e. with low-energy signal derived from the silicon detectors could in principle search for gamma-transitions in  $^{40,41}\text{Sc}$ . No such  $\beta$ -delayed  $\gamma$ -ray events were found. It is clear from Figure 13 and Figure 14, however, that there is only a small number of events just above the electronic threshold that could be candidates for positrons emitted in the decay of  $^{40}\text{Ti}$  and  $^{41}\text{Ti}$ , respectively. Therefore, our experiment is not very sensitive for recording of  $\gamma$ -transitions in  $^{40}\text{Sc}$  or  $^{41}\text{Sc}$ . The upper  $1\sigma$ -limit for the branching ratio of such  $\gamma$ -rays is 5 % in both cases, as mentioned above.

### 3.2.4 Half-life determination

The distributions of time periods, elapsed between implantation and  $\beta$ -decay of  $^{40}\text{Ti}$  and  $^{41}\text{Ti}$ , were generated by the delayed-coincidence technique described in Sect. 3.2.1. To suppress  $\beta$ -background from other nuclei, only events corresponding to  $E_p$  values larger than 1.5 MeV were used. Figure 15 shows the time spectrum obtained for  $^{40}\text{Ti}$ . The half-lives ( $T_{1/2}$ ) of  $^{40}\text{Ti}$  and  $^{41}\text{Ti}$ , measured to be 54(2) and 82(3) ms, respectively, are compared with the results of other works in Table 5. Good agreement within the experimental uncertainties was achieved for both nuclei.

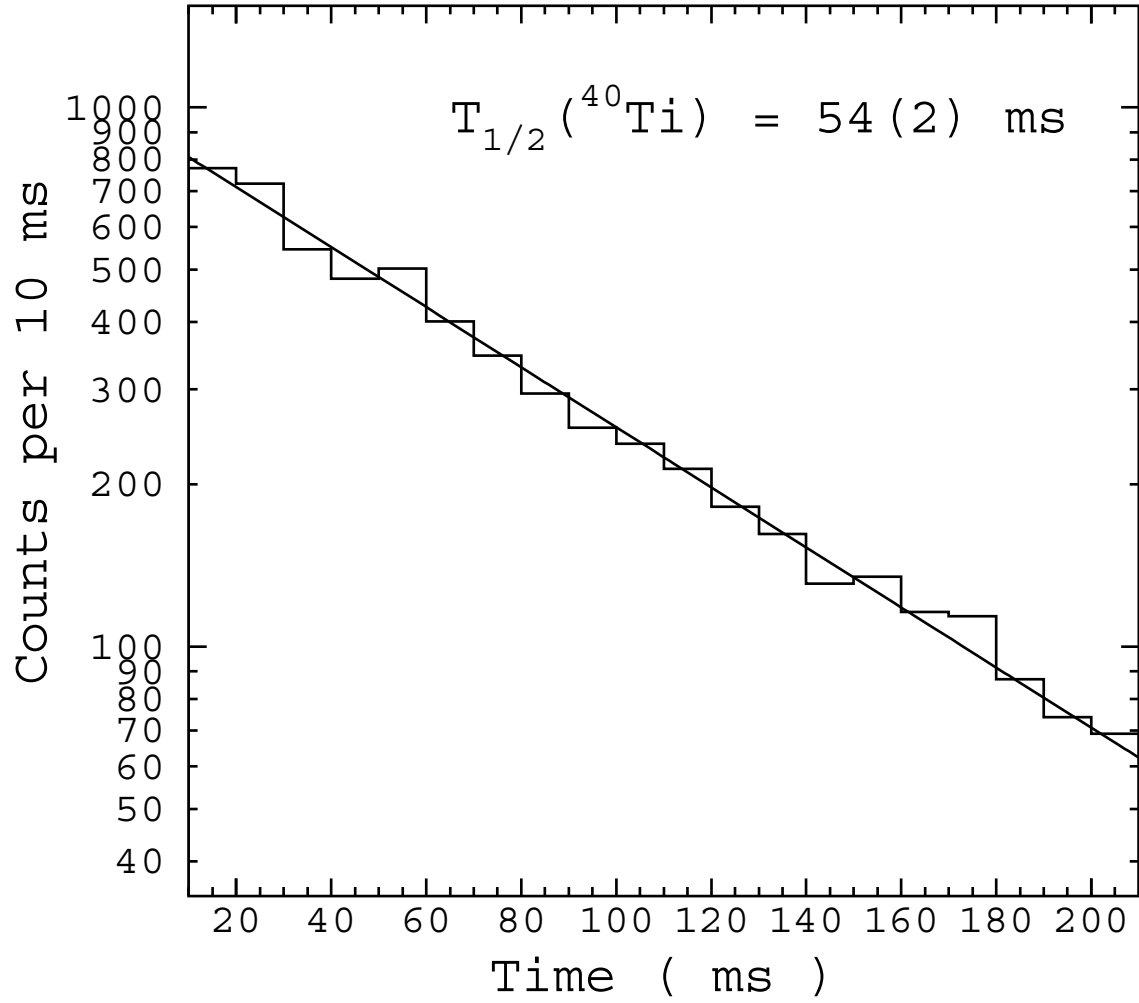


Figure 15: Experimental time spectrum for  $^{40}\text{Ti}$  (histogram) and result obtained from a one-component fit (solid line).

Table 5: Summary of measured half-lives in ms for  $^{40}\text{Ti}$  and  $^{41}\text{Ti}$ .

	This work	Détraz <i>et al.</i> [DÉT90]	Trinder <i>et al.</i> [TRI97B]	
$^{40}\text{Ti}$	54(2)	$56^{+18}_{-12}$	51.7(6)	
	This work	Sextro <i>et al.</i> [SEX74]	Faux <i>et al.</i> [FAU96]	Trinder <i>et al.</i> [TRI97B]
$^{41}\text{Ti}$	82(3)	80(2)	81(4)	80.1(9)



### 3.2.5 Determination of $\beta$ -decay strength

The  $\beta$ -decay strength functions  $B(GT)$  and  $B(F)$  were deduced by using the relation [TRI95B]

$$[B(F) + B(GT)]_i = 6127(9)s / ft_i,$$

with  $t_i = T_{1/2}/b_{\beta}$ ,  $f(Q_{EC}-E_x, Z)$  being the phase space factor in  $\beta$ -decay and  $E_x$  the excitation energy in the daughter nucleus. This evaluation was based on  $T_{1/2}$  results from this work. As discussed by Trinder *et al.* [TRI97B], the  $Q_{EC}$  value of  $^{40}\text{Ti}$  of 11680(160) keV from the literature [AUD97] can be improved by applying the isobaric multiplet mass equation (IMME). This procedure used the experimental excitation energy of the  $^{40}\text{Sc}$  IAS state, measured by Trinder *et al.* [TRI97B] of 4365(8) keV as well as in this work of 4365(10) keV (see Table 3). Appendix 3 presents the detailed description of this procedure. We followed the suggestion of Trinder *et al.* and used the revised  $Q_{EC}$  value of 11466(13) keV [TRI97B], to calculate the transition strengths for  $^{40}\text{Ti}$ . The  $Q_{EC}$  value for the  $\beta$ -decay of  $^{41}\text{Ti}$  was taken to be 12932(40) keV from the mass compilation [AUD97].

The  $B(F)$  and  $B(GT)$  values from this work are displayed in Figure 16 and listed in Table 3 in comparison with results from the other recent  $\beta$ -decay measurement [TRI97B], a  $^{40}\text{Ar}(p,n)^{40}\text{K}$  experiment [AND98], and a shell-model calculation [ORM95]. Figure 17 and Table 4 show the corresponding results for  $^{41}\text{Ti}$ . Based on the results from the present work, partial decay schemes for  $^{40}\text{Ti}$  and  $^{41}\text{Ti}$  are proposed, as shown in Figure 18 and Figure 19.

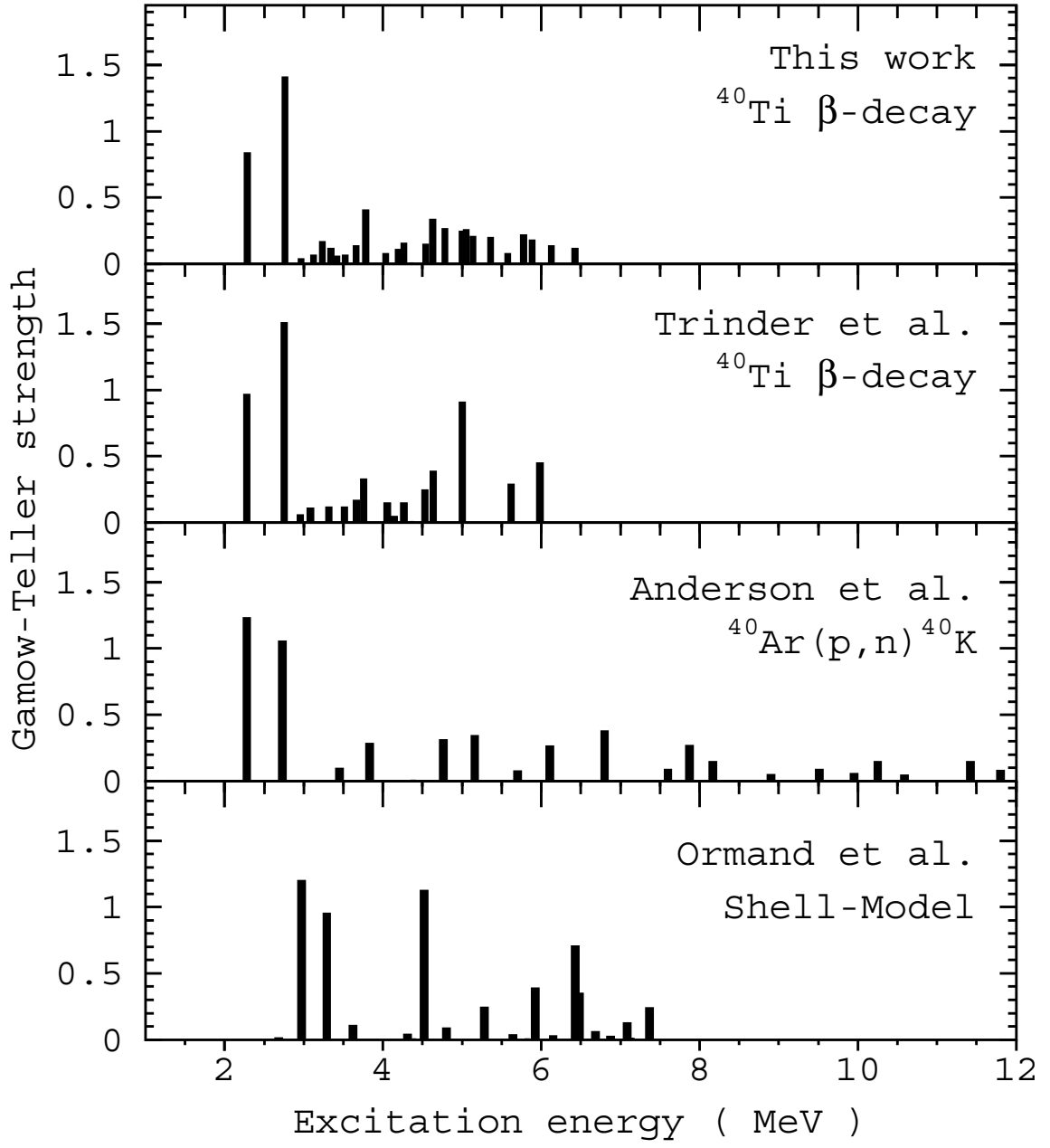


Figure 16: Comparison of Gamow-Teller strength distributions for the  $^{40}\text{Ti}$  decay obtained from the present work, another recent  $\beta$ -decay experiment [TRI97B], an  $^{40}\text{Ar}(p,n)^{40}\text{K}$  measurement [AND98], and a shell-model calculation [ORM95].

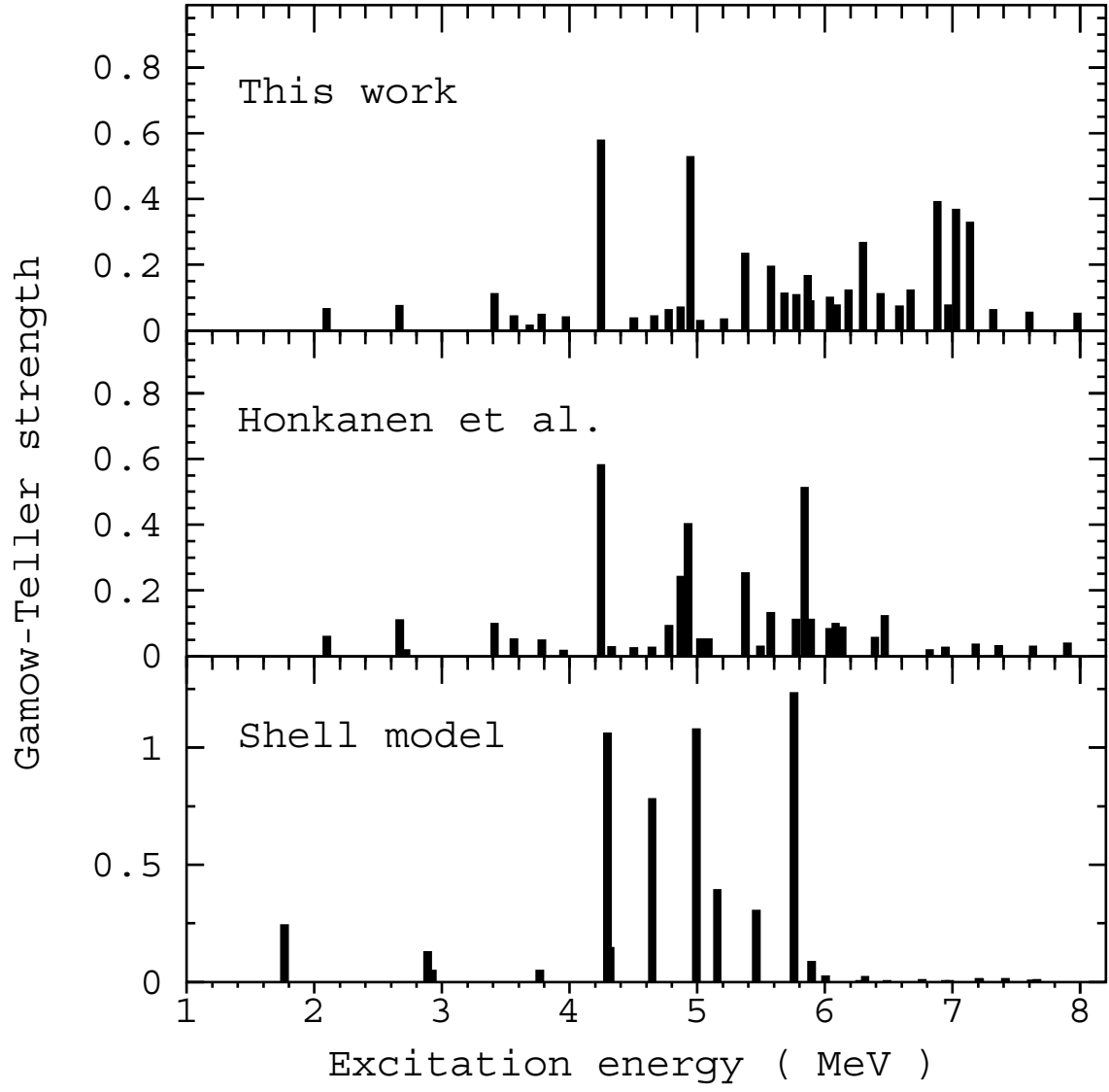


Figure 17: Comparison of Gamow-Teller strength distributions for the  $^{41}\text{Ti}$   $\beta$ -decay, obtained from the present work and the work of Honkanen *et al.* [HON97].

### 3.3 Discussion

#### 3.3.1 Decay strengths of $^{40}\text{Ti}$

In this work, we found the evidences for 18 new proton energy groups compared with the previous analysis [LIU97] of the data obtained in this work, and 9 new proton energy groups compared with Ref. [TRI97B]. This progress is due to the reduction of the  $\beta$ -background and the more detailed analysis of small proton energy groups described in Sect. 3.2.1. Five proton energy groups were assigned, according to the proton- $\gamma$  coincidence data, to proton transitions to the 2469 KeV State in the  $^{39}\text{Ca}$ . The ratio between the  $\text{IAS}(^{40}\text{Sc}) \rightarrow 2469\text{keV}(^{39}\text{Ca})$  decay and the  $\text{IAS}(^{40}\text{Sc}) \rightarrow \text{g.s.}(^{39}\text{Ca})$  transition is 17(3) %. The 951 keV proton energy group was assigned to a transition to the 3026 keV  $3/2^-$  state in  $^{39}\text{Ca}$ , even though the corresponding proton- $\gamma$  coincidence relation was not observed. This non-observation can be explained by taking the intensity of the 951 keV proton energy group and the NaI efficiency for 3026 keV  $\gamma$ -ray into account. Moreover, if one assigned this line to a transition to the  $^{39}\text{Ca}$  ground state, the resulting  $^{40}\text{Sc}$  excitation energy would not have a corresponding level in the mirror nucleus  $^{40}\text{K}$ , which has been extensively studied. The  $J^\pi$  assignment for  $^{40}\text{Sc}$  levels populated by  $\beta$ -decay of  $^{40}\text{Ti}$  were  $1^+$ , except for the 4365 keV level which was identified as the  $0^+$ , IAS. The latter interpretation is based on the observed  $\beta$ -strength of 4.01(31), which agrees with the theoretical value of  $|Z-N| = 4$  for a pure Fermi transition.

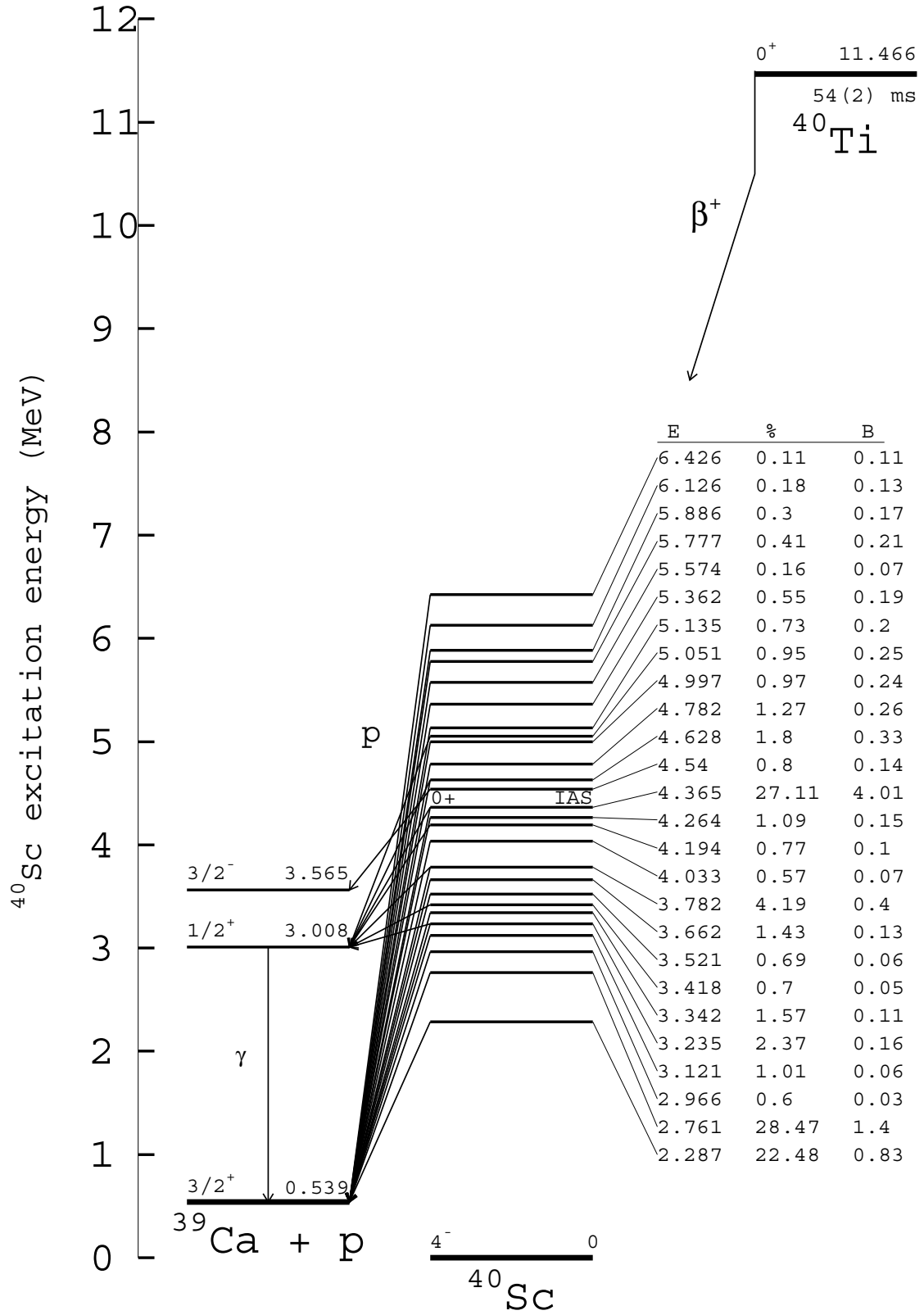


Figure 18: Partial decay scheme for  $^{40}\text{Ti}$ ; E, %, B stand for  $E_x(^{40}\text{Sc})$  in keV,  $b_p$  (%), and  $B(F)+B(GT)$ , respectively. The spin and parity assignments for  $^{40}\text{Sc}$  levels were  $1^+$ , except for the 4365 keV level which was identified as the  $0^+$ , IAS.

The integrated  $B(GT)$  value is 5.84(39), which can be compared with the shell-model result of 5.62 [ORM95] that was obtained by the free-nucleon GT operator quenched by a factor of 0.775. The latter value is in good agreement with the result of 0.79(3) obtained from a comparison of our experimental data with "unquenched" shell-model results. The integrated experimental  $B(GT)$  above the IAS is 2.28(30), whereas the shell-model gives 3.33. In addition to this discrepancy, we note that the shell-model overestimates the excitation energies of the first two excited states of  $^{40}\text{Sc}$  by roughly one MeV, as can be seen from Figure 16; a similar difference in excitation energy was also observed for the  $^{37}\text{Ca}$  decay [KAL97]. To some extent these discrepancies result from the truncation in model space introduced in the shell-model calculation [VIE78].

Excellent agreement was found between the present results and those obtained by Trinder *et al.* [TRI97B] up to a  $^{40}\text{Sc}$  excitation energy of 4 MeV. At higher excitation energies, however, the GT strength from this work was more fragmented than that obtained by Trinder *et al.*. This discrepancy is not surprising as the statistics of our data (see Figure 9) as well as of those obtained by Trinder *et al.* were too poor for proton energies above 4 MeV for an *unambiguous* decomposition into individual transitions. The  $\beta$ -decay data agree with those of the (p,n) work [AND98]. In particular, the  $B(GT)$  values of the (p,n) work for the sum of the first two states are in good agreement with present result. The difference in the ratio between these two states may be due to the difference in the configuration mixing in  $^{40}\text{Sc}$  and  $^{40}\text{K}$ . Note that, due to detector response function (see Sects. 3.1.3 and 3.2.2) and the strong energy dependence of the phase-space factor in  $\beta$ -decay, both  $\beta$ -decay experiments were not very sensitive to the determination of  $\beta$ -strength above a  $^{40}\text{Sc}$  excitation energy of 6 MeV. This is illustrated by the fact that a  $B(GT)$  value of 0.1 for a  $^{40}\text{Sc}$  level at 6.5 MeV corresponds to a  $b_\beta$  value of only 0.1 %, the corresponding proton line being characterized by a large width (FWHM about 150 keV) and a peak-to-total ratio below 50% (see Figure 9). However, this deficiency has only a small impact on the integrated  $B(GT)$  strengths. The sum of experimental  $B(GT)$  values in the region above the IAS up to  $^{40}\text{Sc}$  excitation energy of 5.6 MeV are 2.28(30), 2.24(27), and 1.33(13) from the present  $\beta$ -decay results, from the  $\beta$ -decay data obtained by Trinder *et al.* [TRI97b], and from the (p,n) experiment [AND98], respectively.

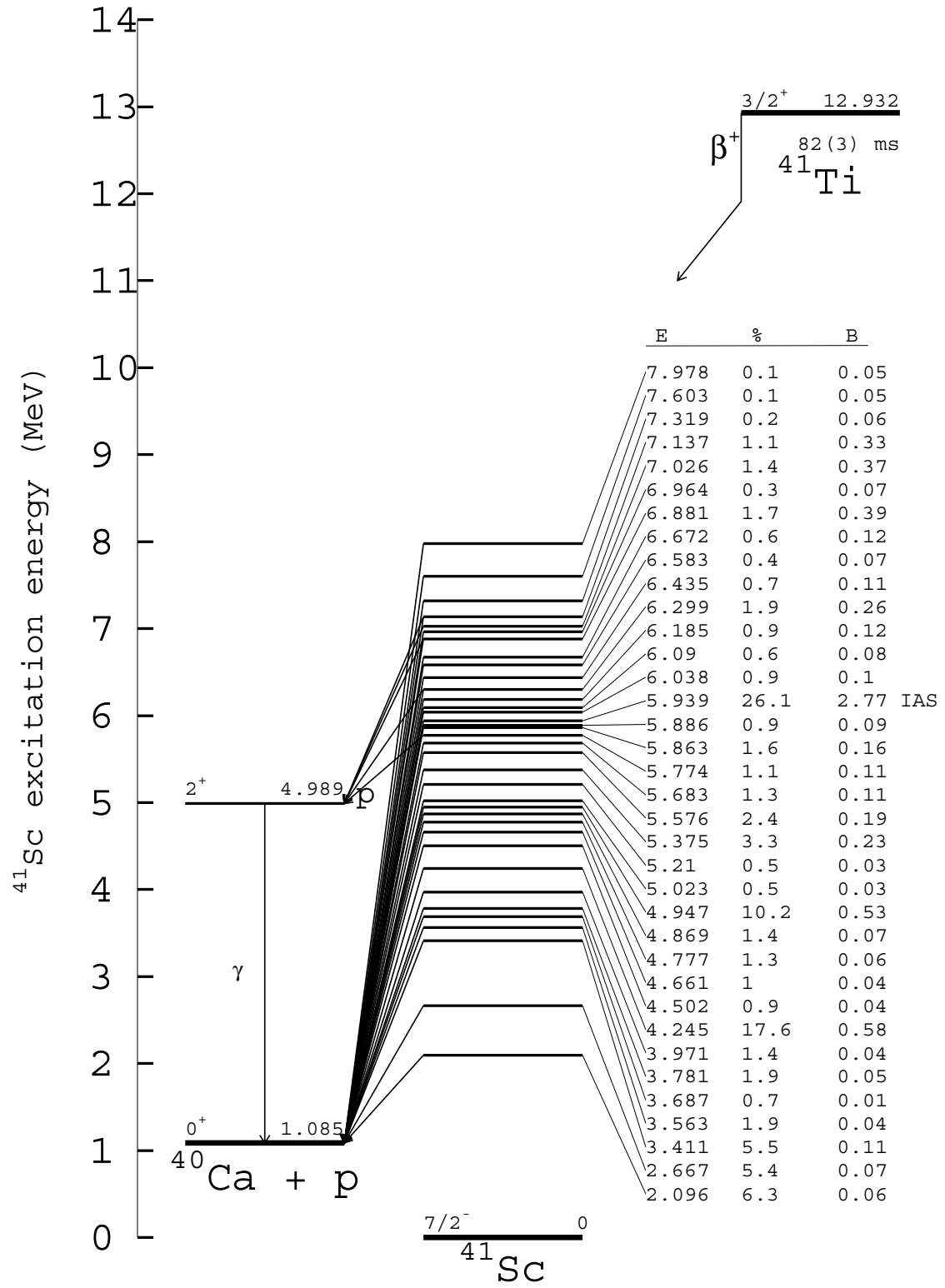


Figure 19: Partial decay scheme for  $^{41}\text{Ti}$ ; E, %, B stand for  $E_x(^{41}\text{Sc})$  in keV,  $b_p$  (%), and  $B(F)+B(GT)$ , respectively. For spin and parity assignments of  $^{41}\text{Sc}$  levels, see Table 4.

The recent  $^{40}\text{Ti}$   $\beta$ -decay study of Trinder *et al.* [TRI97B] was characterized by better statistics and lower electronic thresholds of the silicon detectors compared to our work; the latter feature was used to improve the proton energy resolution by  $\beta$ -energy selection in neighboring detectors. The present work, however, profited from higher purity of the  $^{40}\text{Ti}$  beam with respect to contaminating positron and  $\beta$ -delayed proton emitters, and from higher detection efficiency for  $\gamma$ -rays. The former effect reduced the probability of chance coincidences in the delayed-coincidence procedure, and resulted thus in purer proton energy and decay time distributions. Furthermore, the measurement presented here used thinner silicon detectors (300  $\mu\text{m}$ ) than those used by Trinder *et al.* (500  $\mu\text{m}$ ), which reduced  $\beta$ -summing effects but decreased the full-energy detection efficiency. Furthermore, by using the information of the detector number where the  $^{40}\text{Ti}$  ions were stopped, the  $\beta$ -background was reduced. In summary, the two experiments are complementary, with the good agreement in the  $I_p$  results from both works being indeed remarkable.

### 3.3.2 Decay strengths of $^{41}\text{Ti}$

On the basis of the proton- $\gamma$  coincidence data, five transitions were assigned to populate the 3904 keV State in  $^{40}\text{Ca}$ . According to the experimental  $\log ft$  value from this work and some levels deduced from reaction data [END90], spin and parity assignments of several  $^{41}\text{Sc}$  levels, were made as shown in Table 4. Although there is reasonable overall agreement between the new  $b_\beta$  results and those of previous works [HON97, SEX74, ZHO85], substantial deviations remain for individual  $b_\beta$  values, in particular at high excitation energies. Correspondingly, the resulting  $B(GT)$  values are significantly larger at high excitation  $^{41}\text{Sc}$  energies than those of Honkanen *et al.* [HON97], as can be seen from Figure 17 and Table 4. As an example, the integrated  $B(GT)$  strengths above the IAS from the present work and from the data obtained by Honkanen *et al.* [HON97] are 2.18 (21), and 1.33(12), respectively. In evaluating this discrepancy, we note that proton- $\gamma$  coincidence data have not been available previously. Furthermore, the  $b_\beta$  results from this work were based on the absolute counting of  $^{41}\text{Ti}$  ions, whereas all the earlier experiments [HON97, SEX74, ZHO85] simply normalized the sum of the experimental  $I_p$  values to 100 %. These experimental improvements are probably also responsible for the fact that additional GT strength at high  $^{41}\text{Sc}$  excitation energy was found in the present work.

The integrated  $B(GT)$  strength of 5.6 for  $^{41}\text{Ti}$ , determined by shell-model calculations [HON97], is larger than the values of 4.83(29) from this work. This most probably stems from the fact that no quenching factor was introduced in the calculation. As shown in Figure 17, the  $B(GT)$  prediction agreed with experiment with respect to the gross structure but overestimates the individual strengths at  $^{40}\text{Sc}$  excitation energies of 4-6 MeV, and failed to reproduce the noticeable  $B(GT)$  strengths at even higher excitation energy. The overall GT quenching was obtained to be 0.93(3).

### 3.3.3 Isospin asymmetry in $^{40}\text{Ti}$ - $^{40}\text{Ar}$ mirror pair

The isospin asymmetry ( $\delta$ ) of the mirror  $\beta$ -decay is mainly resulted from the binding energy difference [TOW73]. It is important to know these quantity in detail, to make sure that our application of  $^{40}\text{Ti}$   $\beta$ -decay to  $^{40}\text{Ar}(\nu_e, e^-)^{40}\text{K}^*$  is reliable enough.

We estimated the  $\delta$  values by comparing the  $B(GT)$  values of  $^{40}\text{Ti}$   $\beta$ -decay from this work and those from the measurement of  $^{40}\text{Ar}(p, n)^{40}\text{K}$  reaction [AND98]. We define  $\delta$  as,  $\delta = (ft)^+ / (ft)^- - 1 = B(GT)^- / B(GT)^+ - 1$ . The results are summarized in Table 6.



Table 6: The isospin asymmetry between  $T_z = +2$  ( $^{40}\text{Ar}$ ) and  $T_z = -2$  ( $^{40}\text{Ti}$ ) mirror pair.

$E_x$ ( $^{40}\text{Ti}$ ) (keV)	$E_x$ ( $^{40}\text{Ar}$ ) (keV)	$\delta$
2287	2290	0.48(32)
2761	2730	-0.25(16)
3342	3450	-0.18(62)
3782	3739	-0.30(32)
4782	4789	0.15(54)

From Table 6, we concluded that within the experimental uncertainties, we did not observe the isospin asymmetry in the  $^{40}\text{Ti}$ - $^{40}\text{Ar}$  mirror pair. This is in contrary with the case of  $^{20}\text{Mg}$ - $^{20}\text{O}$  mirror pair, where the  $\delta$  value for  $^{20}\text{Mg}$  3001 keV level (corresponding to the 3488 keV in  $^{20}\text{O}$ ) was 1.69(75) [PIE95].

### 3.3.4 Isospin impurities for $^{40}\text{Ti}$ and $^{41}\text{Ti}$

We deduced the isospin impurities ( $a^2$ ) for  $^{40}\text{Ti}$  and  $^{41}\text{Ti}$  using the relation:  $B(F)_{\text{exp}} = B(F)_{\text{theory}} (1-a^2)$ , where  $B(F)_{\text{exp}}$  and  $B(F)_{\text{theory}}$  are the experimental and theoretical Fermi decay strength respectively. Table 7 presents our results compared with the results from [TRI97B] and [HON97].

Table 7: Isospin impurities for  $^{40}\text{Ti}$  and  $^{41}\text{Ti}$

Nucleus	Data	$[B(F)+B(GT)]_{\text{exp}}$	$B(GT)_{\text{theory}}$	$B(F)_{\text{theory}}$	$a^2$ (%)
$^{40}\text{Ti}$	This work	4.01(31)	0.0	4.00	-0.2(19)
	[TRI97B]	3.90(25)	0.0	4.00	2.5(16)
$^{41}\text{Ti}$	This work	2.77(34)	0.18 <sup>a</sup>	3.00	14(5)
	[HON97]	2.87(22)	0.18 <sup>a</sup>	3.00	10(3)

<sup>a</sup>Theoretical  $B(GT)$  contribution to IAS state, calculated by Honkanen et al. [HON97] using a quenching factor of 0.6.

We concluded from Table 7 that this work and that of Trinder *et al.* [TRI97B] suggested that for  $^{40}\text{Ti}$  there is no isospin impurity within the experimental uncertainty of 2 %. For the case of  $^{41}\text{Ti}$  both this work and that of Honkanen *et al.* [HON97] implied that there was a sizable isospin impurity of the order of 10 % occurs.

### 3.3.5 Calculation of $^{40}\text{Ar}$ neutrino absorption cross-sections

The highest-lying  $^{40}\text{Sc}$  excitation energy reached in this work is 6426(30) keV, compared with the proton separation energy of 7582 keV [AUD97] in the mirror nucleus  $^{40}\text{K}$ . Therefore, the present experiment covers most of the strengths relevant to the  $^{40}\text{Ar}$ -neutrino capture process. Following the procedure suggested by Ormand *et al.* [ORM95] (see also Appendix 3 for a detail), the  $^{40}\text{Ar}$  neutrino absorption rate was calculated according to the experimental  $^{40}\text{Ti}$   $\beta$ -decay strength from this work and the

updated solar neutrino flux of  $6.6^{+0.9}_{-1.1} \times 10^6 \text{ cm}^{-2}\text{s}^{-1}$  [BAH95]. In this calculation, the experimental  $^{40}\text{K}$  excitation energies were used whenever possible; otherwise the  $^{40}\text{Sc}$  excitation energies from this work were taken, as shown in Table 3. The resultant neutrino absorption cross-sections of  $^{40}\text{Ar}$  and the neutrino induced event rates for the ICARUS detector are  $13.8(6) \times 10^{-43} \text{ cm}^2$  and  $9.1 \pm 0.4(\text{stat.})^{+1.3}_{-1.6}(\text{syst.})$  SNU, respectively. The systematical uncertainty is related to the calculation of the solar neutrino flux [BAH95]. As shown in Table 8, these results are in agreement with our previous evaluation [LIU97], the data obtained by Trinder *et al.* [TRI97B], the results based on (p,n) work [AND98], and the shell-model prediction [ORM95]. However, the neutrino absorption cross-section from these sources is approximately four times higher than that calculated by Bahcall [BAH86] about a decade ago ( $3.79 \times 10^{-43} \text{ cm}^2$ ). This discrepancy is due to the significant contribution of GT transition strengths, which was previously not taken into account.

Table 8: Comparison of  $^{40}\text{Ar}$  neutrino absorption cross-sections and neutrino induced event rates for ICARUS detector.

	Cross sections ( $10^{-43} \text{ cm}^2$ )	Solar neutrino flux ( $10^6 \text{ cm}^{-2}\text{s}^{-1}$ )	Event rates (SNU)
This work, $\beta$ -decay data [LIU98]	13.8(6)	$6.6^{+1.3}_{-1.6}$ [BAH95]	$9.1 \pm 0.4(\text{stat.})^{+1.3}_{-1.6}(\text{syst.})$
Liu <i>et al.</i> [LIU97]	-	5.8(21) [BAH86]	6.8(26)
Trinder <i>et al.</i> [TRI97B]	14.5(4)	$6.6^{+1.3}_{-1.6}$	$9.6^{+1.4}_{-1.7}$
This work, (p,n) data <sup>a</sup> [LIU98]	11.9(10)	$6.6^{+1.3}_{-1.6}$	$7.9 \pm 0.7(\text{stat.})^{+1.2}_{-1.5}(\text{syst.})$
Ormand <i>et al.</i> [ORM95]	11.5(7)	5.8(21)	6.7(25)
Bahcall <i>et al.</i> [BAH86]	3.79	-	-
Recommended value [LIU98]	14.3(3) <sup>b</sup>	$6.6^{+1.3}_{-1.6}$	$9.4 \pm 0.4(\text{stat.})^{+1.3}_{-1.6}(\text{syst.})$

<sup>a</sup>Calculated using the  $B(GT)$  value from Ref. [AND98] the  $B(F)$  value from this work.

<sup>b</sup>Weighted average of the results from this work and those from Trinder *et al.*.

Based on the  $^{40}\text{Ti}$   $\beta$ -decay measurement of the present work and that of Trinder *et al.* [TRI97B], a recommended value of  $14.3(3) \times 10^{-43} \text{ cm}^2$  was derived for the neutrino absorption cross-sections of  $^{40}\text{Ar}$ . This result represents the weighted average of the experimental values of  $13.8(6) \times 10^{-43}$  and  $14.5(4) \times 10^{-43} \text{ cm}^2$  (see Table 8). The averaging procedure was based on weights deduced from the uncertainties of the individual experimental results. This approach, which neglects the fact that we used a common  $Q_{EC}$  value (11466(13) keV, see Sect. 3.2.5), is probably justified as the latter has only a minor influence on the individual uncertainties.

The recommended neutrino absorption cross-section, together with the solar neutrino flux according to [BAH95], yields a recommended value of the neutrino induced event rates for the ICARUS detector of  $9.4 \pm 0.2(\text{stat.})^{+1.3}_{-1.6}(\text{syst.})$  SNU.

The summary of the results of this work and those of previous works, as well as interplay between the reaction rates with the solar model prediction of  $^8\text{B}$ -neutrino flux is show in Figure 20. It can be clearly seen that the  $^{40}\text{Ar}$ -absorption cross section is sufficiently accurate, whereas the solar model prediction for  $^8\text{B}$ -neutrino flux has large uncertainty. The latter is the major source of uncertainty in the prediction of ICARUS detector event rate.

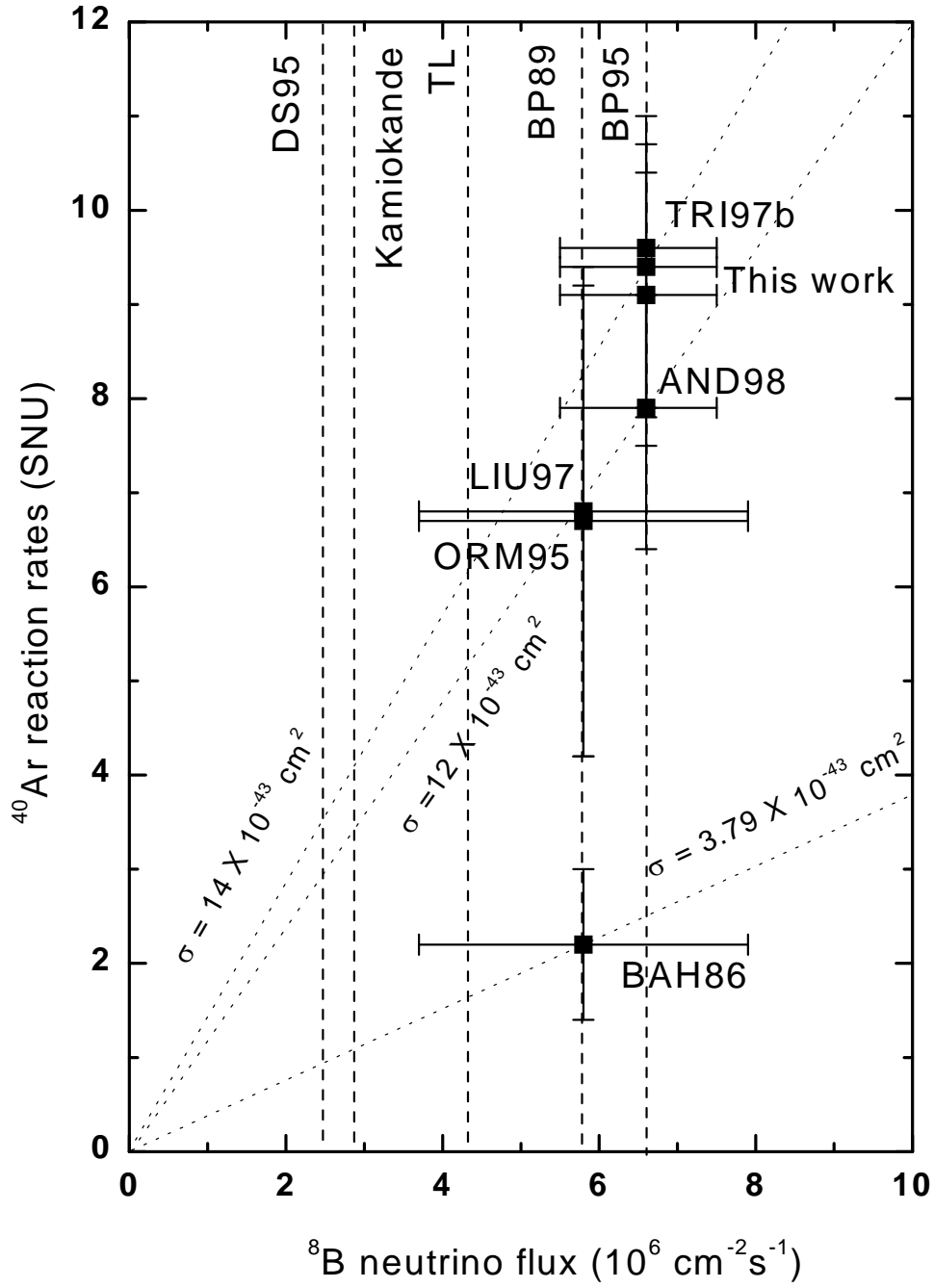


Figure 20: The experimental measurements and theoretical calculations for  $^{40}\text{Ar}$  neutrino absorption rates for ICARUS detector. The vertical dashed line show the model prediction of  $^8\text{B}$  neutrino fluxes (BP95, BP89, TL, DS95) and the measured ones (Kamiokande); the dotted lines show the measured absorption cross-sections (This work, TRI97, AND98, LIU97) and the predicted ones (BAH86), as indicated by values led by arrows.

### 3.4 Summary and outlook

The  $\beta$ -decay of  $^{40}\text{Ti}$  and  $^{41}\text{Ti}$  was investigated by detecting  $\beta$ -delayed proton and  $\gamma$ -rays. For both nuclei, the half-lives were measured and the  $\beta$ -transition strengths were deduced. From the non-observation of  $\beta$ -delayed  $\gamma$ -rays for  $^{40}\text{Ti}$  and  $^{41}\text{Ti}$ , and from the integrated  $b_\beta$  values of 101(5) % and 104(5) %, respectively, it follows that, within the sensitivity of the present experiment,  $\beta$ -delayed proton emission is the only disintegration mode in both cases.

The comparison with the shell-model prediction shows that the quenching factor of 0.775 in the GT operator is adequate for describing the total  $B(GT)$  strength of  $^{40}\text{Ti}$ . Further improvement is needed, however, to account for the discrepancy between experiment and theory in the *shape* of the  $B(GT)$  distribution. Comparing the present results for  $^{41}\text{Ti}$  with shell-model calculation reveals a quenching factor of 0.93(3), i.e. less quenched than that of  $^{40}\text{Ti}$ .

The experimental  $B(GT)$  data for  $^{40}\text{Ti}$  were used to calculate the neutrino absorption cross-section for the ICARUS detector as  $9.4 \pm 0.2(\text{stat.})^{+1.3}_{-1.6}(\text{syst.})$  SNU. The major part of the (systematical) uncertainty was due to the limited knowledge of the solar-neutrino flux. We also note that the  $Q_{EC}$  value, used in this evaluation, does not stem from experiment, but from an IMME analysis.

An improvement of the  $^{40}\text{Ti}$  data obtained in this work could be in principle be realized by using sources prepared by isotope separator on line. This method yields superior energy resolution compared to the present work. Furthermore, proton measurements can be extended to *higher energies* by choosing the adequate detector thickness without the line-shape limitations of the proton peak related to deep implantation. However, it is far from being obvious how  $^{40}\text{Ti}$  sources of sufficient strength and purity can be produced at an isotope separator online. Another improvement would be to re-measure the  $^{40}\text{Ti}$   $\beta$ -decay at the FRS by using a  $^{50}\text{Cr}$  beam, to increase the production rate of  $^{40}\text{Ti}$  ions.

## 4. Acknowledgements

I wish to express my appreciation to many great people who helped me throughout these years.

To Prof. Dazhao Ding, my Chinese supervisor, thank you for those inspiring moments, which prompted me to do better research works and for your valuable encouragement of my new research directions.

To Prof. Ernst Roeckl, my German supervisor, thank you very much for continuously teaching me the ways to do a good nuclear research and to be a good physicist, for your patience and understanding in the experimental work and in the writing of the papers and this thesis.

I would to thank the peoples from the Deutscher Akademischer Austauschdienst very much for their support of my two-year research work and stay in Germany and for their continuous kindness.

I would like to thank the Hongkong Qiushi Science Foundation, for their support of my home research activities and for their understanding of hard works of Chinese scientists under the inferior conditions.

To Prof. Xixiang Bai, my research advisor, thank you for your simulating discussions and suggestions in our home-group responsible for the  ${}^7\text{Be}(\text{d},\text{n}){}^8\text{B}$  work, due to your indispensable contributions, impressive results were achieved in spite of limited experimental conditions.

To the peoples in my home group for your experimental assistance, inspiring contributions and good times, especially to Youbao Wang, Xiaodong Tang, Zhanwen Ma, Chengjian Lin and many others.

Many thanks to GSI staff members, visiting scientists, post-docs, and graduate students who participated in my GSI experiments. You showed me the contemporary know-how of experimental nuclear physics, especially to Dr. Maric Pfötzner, Dr. Margareta Hellström, Dr. Rüdiger Collatz, Dr. Zhiqiang Hu, and Dr. Wilhelm Trinder.

To my son, Dongyuan, you drove me doing things better and I missed you very much during my stay in aboard. And to my wife, Ling Chen, you shared the ups and downs in my graduate period; your understanding, your encouragement, your loving, and your great effort of managing the family during my German stay. All of these helped me bounce back after a fall from time to time.

I am grateful to the staff of tandem accelerator for smooth operation of the machine. The  ${}^7\text{Be}(\text{d},\text{n}){}^8\text{B}$  work was funded in part by National Science Foundation of China under Grant No. 19195007 and Nuclear Industry Science Foundation of China through Grant No. 92A01015.

I am grateful to GSI authority for hosting me working at GSI and the team of FRS and online mass separator for their operations of the devices and for their technical support in preparing the experiments. I would like to thank Prof. B.D. Anderson for making the  ${}^{40}\text{Ar}(\text{p},\text{n}){}^{40}\text{K}$  data available prior to publication. The  ${}^{40}\text{Ti}$   $\beta$ -decay work was supported by the European Union under Contract No. ERBFMGE-CT95-0083.

## 5. Appendix 1: Production of secondary radioactive nuclear beams

### 5.1 Introduction

Up to now, most knowledge in nuclear physics has been obtained from nuclear reactions induced by ion beams of stable isotopes. The isospin degree of freedom of those beams, however, was restricted so far. By broadening the range of isospin available in radioactive nuclei, it is now or will soon be possible to investigate the nuclear properties under very unsymmetrical conditions of the neutron or proton density distribution. This development coincides with increased interest in nuclear astrophysics. In a primordial stage of stellar evolution, the material of nuclear burning consists often of unstable nuclei, so that the experimental data on reactions induced by radioactive nuclear beams (RNB) have become of the fundamental importance in studying nuclear astrophysics. In fact, the production of RNB and the studies based on RNB are the most active fields in nuclear physics nowadays. Many laboratories invest a lot of efforts in producing RNB for nuclear physics research. Since there are many excellent review articles on this topic [MUE93, GEI95], I shall only give a brief introduction of RNB production in the following.

To use RNB, one has to start from the design of a device that transforms a stable isotope beam provided by an accelerator into a secondary beam whose quality is good enough for nuclear physics experiments. Such an attempt was pioneered by Tanihata *et al.* in Berkeley in the 80's and resulted in the successful discovery of a neutron halo in  $^{11}\text{Li}$ . In the beginning of the 90's, the LISE spectrometer in GANIL was built and yielded the discovery of many new isotopes as well as the study of their exotic decay properties such as  $\beta$ -delayed 3-proton emission. Currently, many such devices are operational in the world.

### 5.2 Production mechanism

The general idea of producing RNB is to select a suitable nuclear reaction, which is capable of producing nuclei in a wide range of isospin. The production schemes can be classified according to the reaction mechanisms.

#### 5.2.1 Projectile fragmentation reaction

The projectile fragmentation reaction occurs at a beam energy of 50 to 500 A MeV. The beams with these energies can be produced by a cyclotron (50-200 A MeV) or by a synchrotron (100-500 A MeV). The reaction mechanism was first studied by Goldhaber *et al.* [GOL74] in the 70's. This reaction was used to produce RNB in Berkeley for the first time. Currently, there are a number of devices employing fragmentation reactions, such as LISE3 at GANIL, FRS at GSI, RIPS at RIKEN, A1200 at MSU, etc. The first advantage of this approach is that the fragments approximately reserve the same velocity as the primary beam with a limited momentum spread (discussed below in detail). As a result, the outgoing fragments, which are concentrated in a forward cone, can easily be collected, separated, and identified. A further advantage is that the fragments are produced in a wide isospin range extending to the proton or neutron drip line for light nuclei, which makes this reaction an ideal tool to produce very proton-rich or neutron-rich RNB.

According to the Goldhaber's work, the momentum distribution of projectile fragments is parameterized as follows:

$$\frac{d^3\sigma}{dp} \propto \exp\left[-\frac{p_{\perp}^2}{2\sigma_{\perp}^2} - \frac{(p_{\parallel} - p_0)^2}{2\sigma_{\parallel}^2}\right],$$

where the perpendicular momentum width is

$$\sigma_{\perp} = \sigma_0 \sqrt{A_F(A_p - A_F)/(A_p - 1)},$$

and the transverse momentum width is

$$\sigma_{\perp}^2 = \sigma_0^2 A_F(A_p - A_F)/(A_p - 1) + \sigma_1^2 A_F(A_F - 1)/A_p(A_p - 1),$$

with  $\sigma_0 \approx 90 \text{ MeV}/c$ ,  $\sigma_1 \approx 200 \text{ MeV}/c$ , and  $\sigma_0 = \frac{p_F}{\sqrt{5}}$ ,  $p_F$  being the Fermi momen-

tum. For example, for  $A_p = 11$  and  $A_F = 9$ , one obtains  $\sigma_{\parallel} = 133 \text{ MeV}/c$  and  $FWHM_{\parallel} = 312 \text{ MeV}/c$ .

The production cross section  $\sigma$  is usually estimated by the empirical code EPAX [SÜM90] as:

$$\sigma(A, Z) = Y(A) n \exp(-R/Z_p - Z/U),$$

where  $n$  is a normalisation factor,  $Y(A)$  the total yield of for the fragment mass number  $A$ ,  $Z_p$  the peak position in the  $Z$  distribution of the cross section,  $R$  the width parameter, and  $U$  a parameter, which is assumed as 1.5 for  $Z_p > Z$  and 2.0 for  $Z_p < Z$ .

It can be seen from the above equations that the cross section is basically independent of the projectile energy, whereas it strongly depends on the isospin of the projectile. The more proton (neutron)-rich the projectile is, the higher will be the production yield for the proton (neutron)-rich fragments.

One also needs to calculate the total reaction cross section  $\sigma_{tot}$ , e.g. in the case of estimating the reaction loss due to an energy degrader. This can also be done by using EPAX, based on the following formula developed by Kox *et al.* [KOX85]:

$$\sigma_{tot} = \pi r_0^2 \left( A_p^{1/3} + A_T^{1/3} + a \frac{A_p^{1/3} A_T^{1/3}}{A_p^{1/3} + A_T^{1/3}} - c \right)^2 \left( 1 - \frac{B_C}{E_{CM}} \right),$$

where  $B_C$  is Coulomb barrier energy:

$$B_C = \frac{Z_p Z_T e^2}{r_c (A_p^{1/3} + A_T^{1/3})}.$$

The constants involved in these two equations are  $r_0 = 1.1 \text{ fm}$ , and  $a = 1.85$ ,  $c$  is increased linearly from 0.65 (at  $30 \cdot A \text{ MeV}$ ) to 2.05 (at  $200 \cdot A \text{ MeV}$ ),  $r_c = 1.3 \text{ fm}$ , and  $E_{CM}$  is the center-of-mass energy of the projectile.

For example, the total reaction cross section for the system  $^{58}\text{Ni} + ^9\text{Be}$  is 1.643 b at a  $^{58}\text{Ni}$  beam energy of  $500 \cdot A \text{ MeV}$ , and the corresponding cross section for the production of  $^{40}\text{Ti}$  is  $1.6 \times 10^{-5} \text{ mb}$ .

### 5.2.2 Transfer reaction

The idea of using a transfer reaction to produce RNB can be traced back to the 70's when high precision spectrometers like Q3D were used to study such reactions. The device dedicated to RNB was firstly established in LLNL, where a QSBTS spectrometer was used to study the  $^7\text{Be}(d,n)^8\text{B}$  reaction. Today, such devices are used in Notre Dame, in Beijing (GIRAFFE) and elsewhere. The transfer reaction has a simple



exit channel, so that a simple separation device can achieve very high purity and intensity of the respective RNB.

In most cases, inverse geometry is adapted by using a heavy beam impinging on a light target. For example, to produce  $^7\text{Be}$  beam in GIRAFFE, a  $^7\text{Li}$  beam was guided to a  $\text{H}_2$  gas target, in which  $^7\text{Li}(\text{d},\text{n})^7\text{Be}$  reactions occurred. Such geometry compresses the reaction products  $^7\text{Be}$  to a small angular cone of  $9^\circ$ , see Appendix 2 for a detailed description of this device. Because of the small momentum transfer from beam to target, the velocity of  $^7\text{Be}$  is roughly the same as that of  $^7\text{Li}$ , similar to projectile fragmentation reactions. Thus the resulting RNB is also easy to collect and to focus. The production cross section and angular distribution can be calculated by a DWBA program. In practice, one often uses the experimentally measured low-energy reaction data that have well established before. The charge-exchange reactions such as  $^7\text{Li}(\text{d},\text{n})^7\text{Be}$  are frequently used, which have production cross sections of several tens of mb and result in a different atomic number ( $Z$ ) of the reaction products compared to that of the primary beam. Such a  $Z$  difference results in a large magnetic rigidity difference, which in turn is a key factor to achieve a high RNB purity. To produce more exotic RNB, one may use two- or multi-nucleon transfer reaction, with production cross section two- or multi-orders of magnitude lower.

### 5.2.3 Fusion-evaporation and spallation reactions

Fusion-evaporation or spallation reactions are mainly used in mass separator on line, pioneered by ISOLDE in CERN, followed by online mass separator at GSI, at Jyväskylä and other laboratories. These kind reactions proceed in two steps. Firstly, the beam and the target nuclei fuse into a compound nucleus, which then evaporate neutrons or protons and thus leave residues that can be collected. Such products can be easily collected in an ion-source for further mass separation using online mass separator (These residues can also be electromagnetically separated via a recoil separator, that will not be discussed here.). The merits the RNB resulting from this approach is the excellent energy resolution and beam quality, which are very useful in high-resolution  $\beta$ -decay spectroscopy studies, such as those performed for the  $^{37}\text{Ca}$   $\beta$ -decay at CERN, study of  $\beta$ -decays of nuclei in  $^{100}\text{Sn}$  region at GSI, and for the  $^{41}\text{Ti}$   $\beta$ -decay at Jyväskylä. The drawback of the mass separator is that it is only mass sensitive, with the collection/release efficiencies of RNB being  $Z$ -dependent.

### 5.3 Separation methods

The principle of separation of RNB, as briefly indicated before, is based on electric and/or magnetic fields to select the desired isotope by its magnetic rigidity  $B\rho$  (electro-magnetic device), by its velocity  $v$  (velocity filter), or by its mass number  $A$  (mass separator). The principle of separation and particle identification can be summarized in the following formulae.

$$AZ^2 \propto E\Delta E$$

$$E = A(\gamma-1)$$

$$B\rho = p/q = A\beta\gamma/q = B\rho_0(1+x/d)$$

with  $\gamma = 1/(1-\beta^2)^{1/2}$ , where  $E$  and  $\Delta E$  are the total energy and energy-loss of the ion,  $Z$  and  $q$  its atomic number and charge state,  $x$  and  $d$  its position and the dispersion in the focal plane.

Under the condition of the small spectrometer acceptance  $\Delta p/p$ ,  $\beta$  is constant. For the case of  $q = Z$ , which is valid in the energy of multi-hundred-A MeV,

$$Z \propto (\Delta E)^{1/2},$$

$$TOF \propto A/Z.$$

where  $TOF$  is the time of flight of an ion.

In general, the atom is not fully stripped, so that  $q = Z, Z-1, \dots$ . As a result,

$$TOF \propto A/q,$$

$$q \propto E.$$

The detailed treatment for partially stripped charge states can be found in [LIU88].

For the velocity filter,  $v \propto B/E$ , where  $B$  and  $E$  stand for the magnetic field and electric field of the filter, respectively.

### 5.3.1 Electromagnetic device

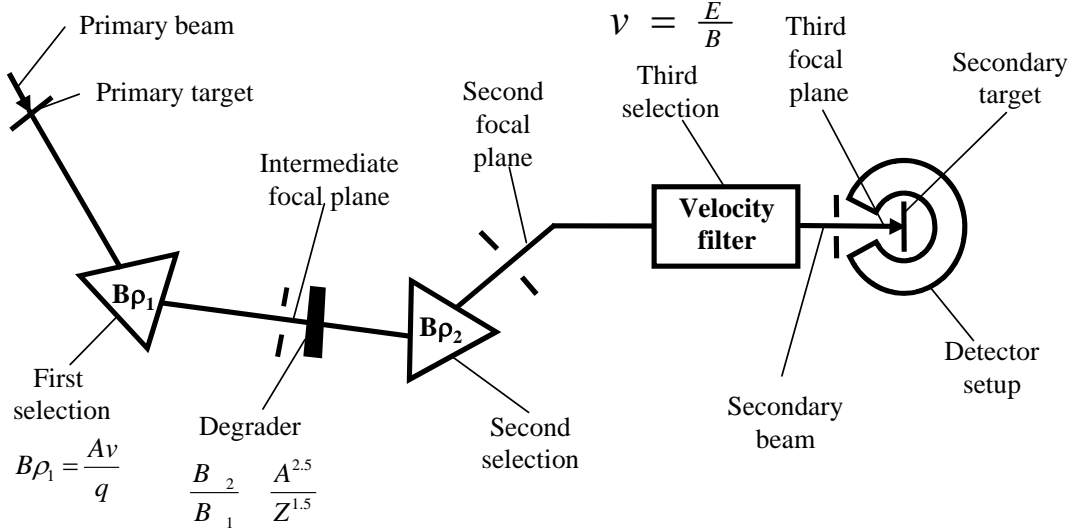


Figure 1: Setup of a electromagnetic device.

A general layout of an electromagnetic device is shown in Figure 30. According to the complexity of RNB, these devices are further categorized as subsequent arrays comprising one-stage such as GIRAFFE, two-stage such as FRS, or three-stage such as LISE.

### 5.3.2 Mass separator online

Mass separator online use fusion evaporation reactions or spallation reactions to produce RNB, which are stopped in a catcher in an ion-source. Different kinds of ion-sources are used to combine chemical selectivity with high efficiency even for short-lived nuclei. For example, laser ion-source can be applied to achieve more chemical selectivity. The RNB of interest are then extracted, accelerated, and mass separated for the final use.

## 5.4 Beam intensity and applications

The intensity of RNB can be obtained by using the following formulae.

$$I = \varepsilon n_i N_t \sigma,$$

where  $\varepsilon$  is the collection and separation efficiency of secondary beam line,  $n_i$  the beam intensity,  $N_t$  the effective target thickness, and  $\sigma$  the production cross section. The product of  $n_i$  and  $N_t$  is also called luminosity. Depending on the available RNB intensities, various nuclear physics experiments can be performed as illustrated in Figure 2.

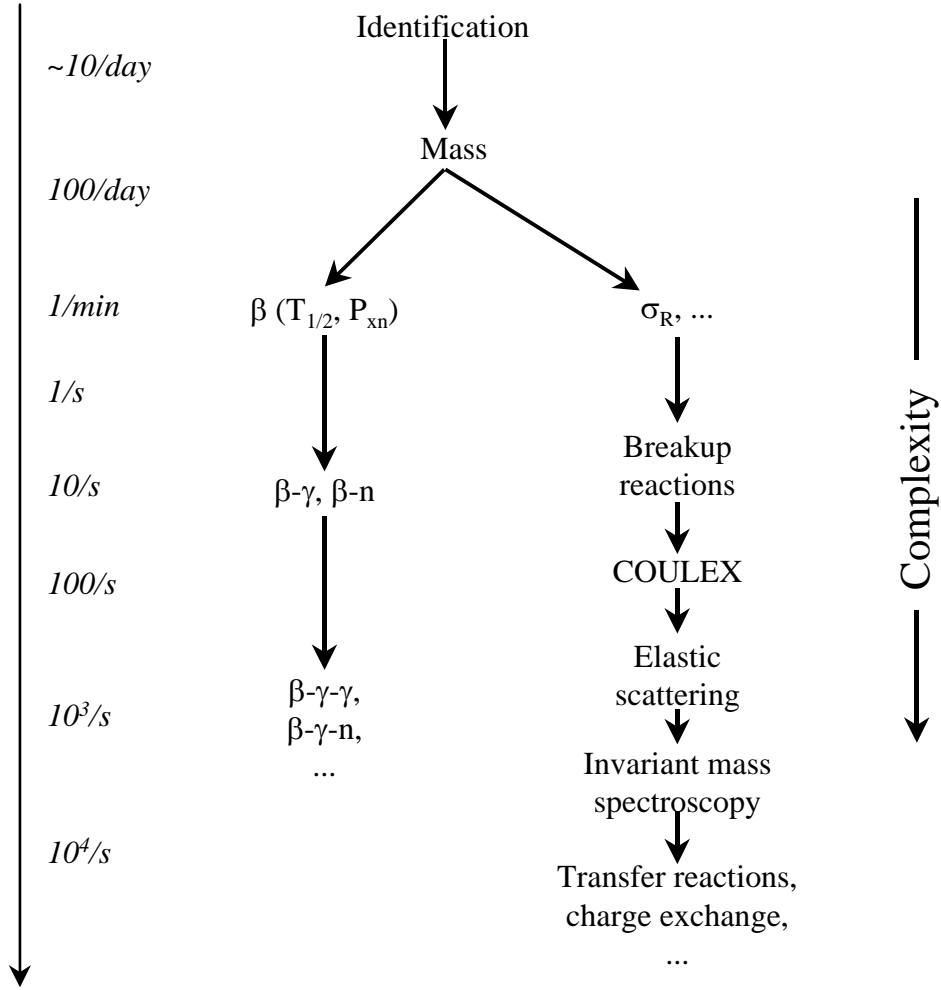


Figure 2: The relation between the intensity of RNB and its possible nuclear physics experiments.

### 5.5 FRS, the secondary beam line in GSI

The second part of this Ph.D. thesis, i.e. the measurement of  $\beta$ -decay of  $^{40}\text{Ti}$  and  $^{41}\text{Ti}$ , was performed on the GSI fragment separator (FRS) [GEI92]. It uses projectile fragmentation reaction and has a two-stage electromagnetic design. Because of the high magnetic rigidity of fragments (up to 18 Tm), it is not possible to include a third-stage separation, namely a velocity filter. This solution was ruled out due to the difficulties of reaching high electric fields.

#### 5.5.1 General layout

The general layout of FRS is shown in Figure 3. It is a double achromatic device, so that ions with angular emittance of 3.4 msr and a momentum distribution of 2 % can be focused at  $F_4$  to a spot of 0.6 cm in diameter. Apart from the conventional energy degrader at  $F_2$ , an additional degrader was installed at  $F_1$  in order to further suppress contaminants.

### 5.5.2 Beam diagnostics

In front of the primary target, an ionization chamber (SEETRAM) can be inserted to measure the primary beam intensity. In  $F_2$ ,  $F_3$ , and  $F_4$ , scintillation counters (SC), and MWPC's can be inserted to measure TOF and beam profile, respectively.

Furthermore, a MUSIC detector is used for measuring the energy-loss of RNB at  $F_4$ , in order to identify the projectile fragments by their atomic number. The SC and MWPC, can stand counting rates up to 10 kHz, whereas the counting rates in the MUSIC is limited to 1 kHz. It is therefore important to suppress the contaminants as much as possible at  $F_4$ .

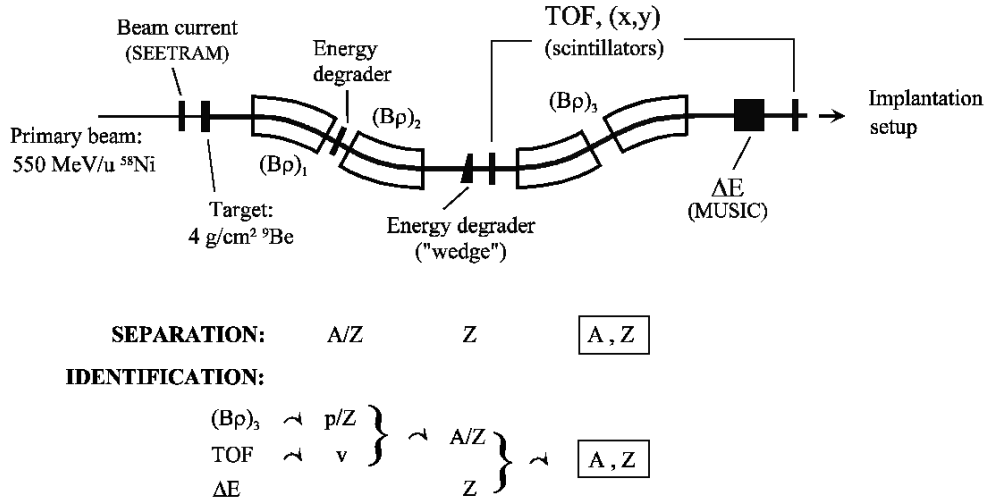


Figure 3: Layout of FRS.

### 5.5.3 Production of $^{40}\text{Ti}$ beam

The beam-target combination used to produce  $^{40}\text{Ti}$  beam was  $^{58}\text{Ni}$  on  $^9\text{Be}$ . In the original proposal underlying this experiment, a  $^{50}\text{Cr}$  beam was proposed, which unfortunately was not available at the time of the experiment. The  $^{40}\text{Ti}$  production cross sections calculated by EPAX are  $1.6 \times 10^{-5} \text{ mb}$  and  $3.6 \times 10^{-5} \text{ mb}$  for  $^{58}\text{Ni}$  and  $^{50}\text{Cr}$  beam, respectively. Furthermore, the  $1\sigma$ -widths of perpendicular momentum of  $^{40}\text{Ti}$  are 320 MeV/c and 257 MeV/c for  $^{58}\text{Ni}$  and  $^{50}\text{Cr}$  beam, respectively, so that the FRS transmission for  $^{50}\text{Cr} \rightarrow ^{40}\text{Ti}$  is 20 % higher than that for  $^{58}\text{Ni} \rightarrow ^{40}\text{Ti}$ . Therefore, the  $^{40}\text{Ti}$  beam intensity from  $^{58}\text{Ni}$  fragmentation was lower than originally proposed.

The basic parameters for the FRS, used in the  $^{40}\text{Ti}$  measurement, are summarized in Table 1. By using the energy degrader in  $F_2$ , the contaminants are effectively rejected as shown in 错误！未找到引用源。 .

Table 1: The FRS parameters used in the  $^{40}\text{Ti}$  measurement

---

Primary beam: $^{58}\text{Ni}$ , $14^+$ , 500·A MeV, $10^9$ ions/s
Primary target: natural Be, 4000 mg/cm <sup>2</sup>
Magnetic rigidities: $B\rho_1$ 5.488 Tm, $B\rho_2$ 4.969 Tm, $B\rho_3$ 3.787 Tm, $B\rho_4$ 3.772 Tm, ( $\rho = 11.3$ m)
F <sub>1</sub> degrader: Al, 1778 mg/cm <sup>2</sup>
F <sub>2</sub> degrader: Al, 3158 mg/cm <sup>2</sup>
Counting rates: F <sub>2</sub> 25 kHz, F <sub>4</sub> 150 Hz

---

To shift the center of the  $^{40}\text{Ti}$ -range profile to the center of the silicon detector stack, an energy degrader of 1.14 g/cm<sup>2</sup> Al was inserted at F<sub>4</sub>. As a result of this degrader, a secondary-reaction loss of  $^{40}\text{Ti}$  ions has to be taken into account in the calculation of absolute proton branching ratio in  $^{40}\text{Ti}$  decay. This can be either calculated or measured. According to the EPAX prediction [SÜM90], the total reaction cross section of 200·A MeV  $^{40}\text{Ti} + ^{27}\text{Al}$  amounts to 2.0 b. Taking into account the degrader thickness, we estimated the secondary reaction loss to be 10 %. This is in good agreement with the measured value of 13(3) %.

## 5.6 Future development

The future developments are based on the idea of improving RNB, with respect to beam quality and/or intensity. This can be realized by coupling an accelerator after an electromagnetic ISOL device such as Louvain-la-Neuve in Belgium (ISOL method), or by building an accelerator with enhanced primary beam intensity followed by a projectile fragment separator (PF method) such as the RNB factory in RIKEN. Presently, a large number of facilities base on ISOL or PF method are being constructed or planned. In the near future, considerably improved studies of the isospin degree of freedom and of phenomena of interest to nuclear astrophysics will thus become possible.

## 6. Appendix 2: Production and Use of secondary radioactive nuclear beams at HI-13 Tandem Accelerator

### 6.1 Introduction

A radioactive nuclear beam (RNB) facility (GIRAFFE) has been built at the HI-13 tandem accelerator of China Institute of Atomic Energy (CIAE). The facility makes use of the inverse kinematics. It was designed for yielding low energy  ${}^6\text{He}$ ,  ${}^7\text{Be}$ ,  ${}^8\text{Li}$ ,  ${}^{11}\text{C}$ ,  ${}^{12}\text{B}$ ,  ${}^{13}\text{N}$ ,  ${}^{15}\text{O}$  and  ${}^{17}\text{F}$  secondary beams with intensities of  $10^4$ - $10^6$  ions/s and for studying reactions of nuclear physical and astrophysical interest. The facility and experimental results in producing RNB will be described.

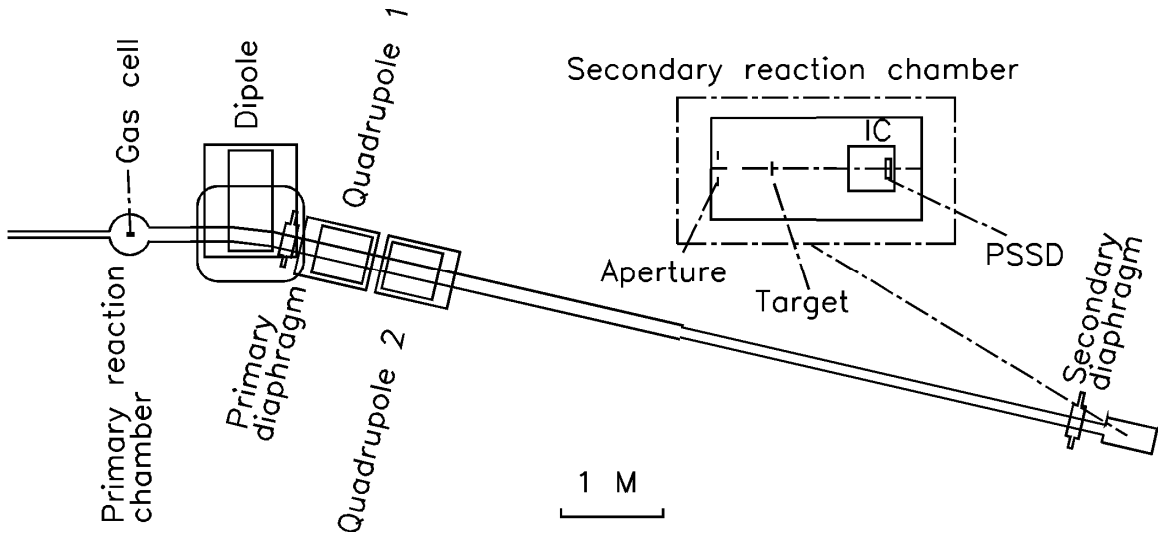


Figure 1: Layout of GIRAFFE

### 6.2 General Description of the Facility

As a starting point towards studies with RNB at CIAE, the facility GIRAFFE for producing and for utilizing low energy beams of unstable nuclei such as  ${}^6\text{He}$ ,  ${}^7\text{Be}$ ,  ${}^8\text{Li}$ ,  ${}^{11}\text{C}$ ,  ${}^{12}\text{B}$ ,  ${}^{13}\text{N}$ ,  ${}^{15}\text{O}$  and  ${}^{17}\text{F}$  has been constructed at the HI-13 tandem laboratory. GIRAFFE was designed for studying a number of reactions of astrophysical interest and charge-exchange reactions among several  $T_z = \pm 1/2$  pairs of mirror nuclei.

GIRAFFE makes use of the inverse kinematics. The general feature of the facility is schematically shown in Figure 1. It comprises a primary reaction chamber, a dipole-quadrupole doublet (D-Q-Q) beam transport system and a secondary reaction chamber. The primary beams of  ${}^7\text{Li}$ ,  ${}^{11}\text{B}$ ,  ${}^{12}\text{C}$ , and  ${}^{16}\text{O}$  ions from the HI-13 tandem accelerator were used for bombarding a hydrogen or deuterium gas cell in the primary reaction chamber to produce unstable nuclei of interest via reactions such as  ${}^1\text{H}({}^7\text{Li}, {}^7\text{Be})n$ . Because of the kinematic effect, the desired unstable nuclei are compressed into a forward cone. Figure 2 displays the angular distribution of the magnetic rigidity of  ${}^7\text{Be}$  and that of scattered  ${}^7\text{Li}$ , and Figure 3 shows the differential cross section of the  ${}^7\text{Be}$  ions from the  ${}^1\text{H}({}^7\text{Li}, {}^7\text{Be})n$  reaction at  $E({}^7\text{Li}) = 35$  MeV. The RNB of interest were then magnetically separated from the scattered  ${}^7\text{Li}$  beam and unwanted reaction products, and finally focused onto a secondary reaction target by using the D-

Q-Q system. Figure 4 shows the result of beam optics calculation. The basic parameters of the secondary beam line are summarized in Table 1.

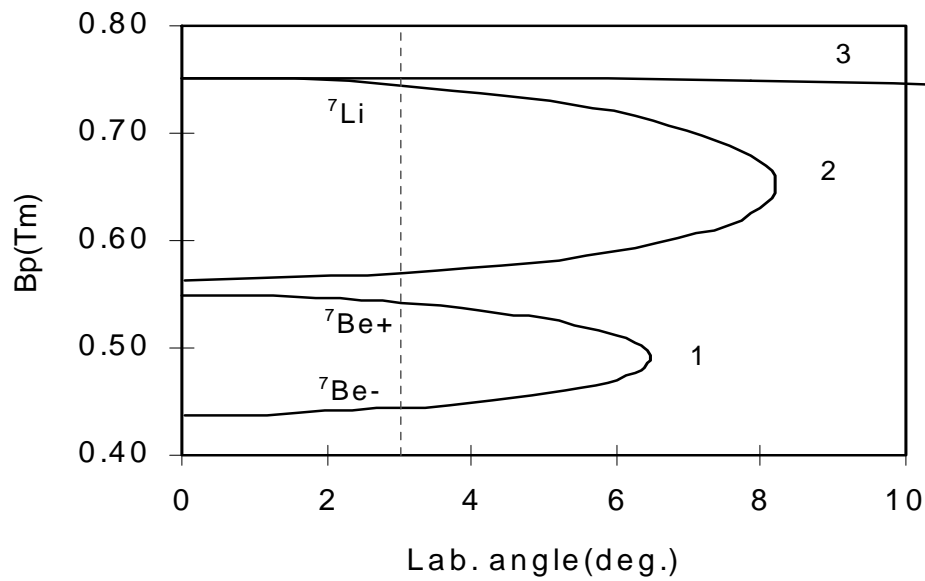


Figure 2: Angular distributions of magnetic rigidity of  ${}^7Be$  and scattered  ${}^7Li$ . 1:  ${}^1H({}^7Li, {}^7Be)n$ , 2:  ${}^1H({}^7Li, {}^7Li){}^1H$ , 3:  ${}^{nat}Ti({}^7Li, {}^7Li){}^{nat}Ti$  at  $E({}^7Li)=35$  MeV. The dashed line shows the acceptance angle of GIRAFFE.

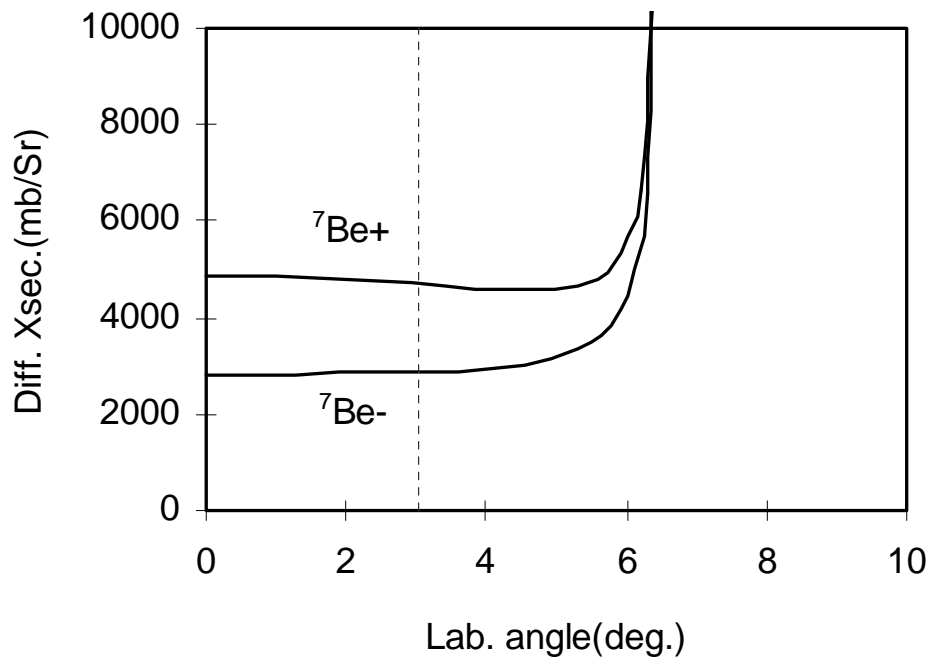


Figure 3: Differential cross section of  ${}^1H({}^7Li, {}^7Be)n$  reaction at  $E({}^7Li)=35$  MeV. The dashed line shows the acceptance angle of GIRAFFE.



Table 1: The basic parameters of GIRAFFE.

Maximum solid angle	$\Delta\Omega = 1.8 \text{ msr}$ ( $\Delta\theta = \pm 16.4 \text{ mrad}$ , $\Delta\phi = \pm 34.8 \text{ mrad}$ )
Maximum rigidity	$B\rho = 1.4 \text{ Tm}$
Total length	$L = 9.8 \text{ m}$
Focal plane dispersion	$\Delta X/(\Delta p/p) = 0.47 \text{ cm/\%}$
Acceptance angle	$3^\circ$
Deflection angle	$13^\circ$

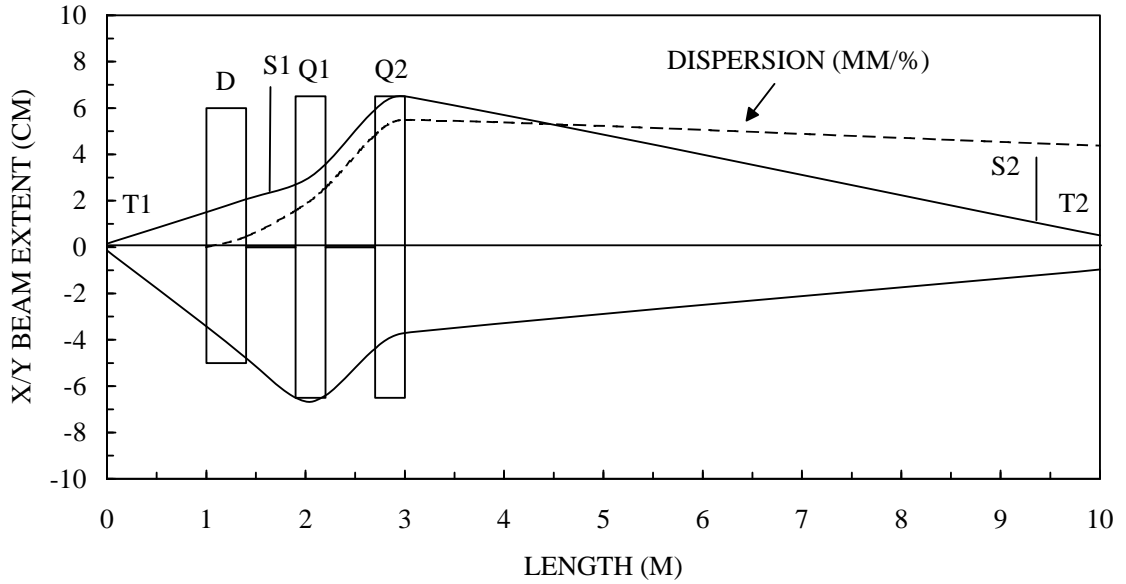


Figure 4: The result of beam optics calculation (T1: production target; D: dipole magnet; Q1 and Q2: quadrupole magnets; S1 and S2: slits; T2: secondary target).

Downstream of the secondary reaction target, a detector telescope was mounted on a rotatable arm for observing the reaction products of interest. It was found in the initial RNB tuning experiments that the appropriate choice of the acceptance angle for each of the desired RNB plays a critical role in purifying secondary beams. So far a value of  $3^\circ$  has been chosen for this angle (see Section 6.6). It is planned to install a beam swinger at upstream of the primary reaction chamber for optimizing the incident angles.

### 6.3 Choice of production reactions

Taking the beam energy and the beam intensity at HI-13 Tandem accelerator into account, the RNB production reactions were selected based on the following considerations:

- The reaction products should have high differential cross sections. Consequently the reactions of inverse kinematics, such as  $^1\text{H}(^7\text{Li}, ^7\text{Be})\text{n}$ , were selected, in which the reaction products of interest were compressed into a forward cone.
- The reactions should have large total cross sections. The charge exchange and single nucleon transfer reactions were adapted. As a result, RNB are limited to the isotopes near the  $\beta$ -stability line.
- The magnetic rigidities of the desired RNB should be considerably different from those of the primary beams and the products from other reaction channels. The (p,n) and (d,n) reactions are most suitable for this purpose, since the RNB of interest and the primary beam have different magnetic rigidities due to the differences in atomic numbers.
- In order to sustain the high current of the primary beam, a  $\text{H}_2$  or  $\text{D}_2$  gas target with titanium windows was adopted.
- For a specific reaction, one can select either the positive or negative group of center-of-mass angular distribution, depending on the compromise between magnetic rigidity difference and the differential cross sections.

Some reactions that meet the above criteria are summarised in Table 2.

Table 2: Summary of production reactions for the secondary beams and the characteristics of resulted beams.

RNB	Production reaction	$E_{\text{beam}}$ (MeV)	$d\sigma/d\Omega$ (mb/Sr)	$E_{\text{RNB}}$ (MeV)	$\Delta B\rho/B\rho$ (%)	Intensity* (pps)
$^6\text{He}$	$^2\text{H}(^7\text{Li}, ^6\text{He})^3\text{H}$	42.0	160+	$34.0 \pm 1.0$	17.3	$2.2 \times 10^5$
$^7\text{Be}$	$^1\text{H}(^7\text{Li}, ^7\text{Be})\text{n}$	35.0	5000+	$33.0 \pm 0.5$	-3.1	$1.4 \times 10^7$
$^8\text{Li}$	$^2\text{H}(^7\text{Li}, ^8\text{Li})^1\text{H}$	42.0	900+	$40.0 \pm 0.5$	5.2	$1.2 \times 10^6$
$^{11}\text{C}$	$^1\text{H}(^{11}\text{B}, ^{11}\text{C})\text{n}$	78.1	6700-	$57.0 \pm 1.0$	-17.5	$4.5 \times 10^6$
$^{12}\text{B}$	$^2\text{H}(^{11}\text{B}, ^{12}\text{B})^1\text{H}$	66.0	1100+	$65.0 \pm 1.0$	6.3	$1.5 \times 10^6$
$^{13}\text{N}$	$^2\text{H}(^{12}\text{C}, ^{13}\text{N})\text{n}$	70.8	3000+	$70.0 \pm 1.0$	-9.7	$2.1 \times 10^6$
$^{15}\text{O}$	$^2\text{H}(^{14}\text{N}, ^{15}\text{O})\text{n}$	84.0	8300+	$82.0 \pm 1.0$	-12.7	$3.7 \times 10^6$
$^{17}\text{F}$	$^2\text{H}(^{16}\text{O}, ^{17}\text{F})\text{n}$	88.0	28000+	$85.0 \pm 0.3$	-10.8	$1.3 \times 10^7$

\*Values calculated by assuming a primary beam intensity of 1.0  $\mu\text{A}$ , gas cell pressure of 1 atm, and differential cross sections at their optimum angles. The marks + and - refer to the forward and backward center-of-mass angular group selected, respectively.

## 6.4 Design of the beam line

In the designing of beam line GIRAFFE, the following factors were taken into account:

- Large solid angle. The dipole magnet (D) with large gap and the quadrupole lens (Q) with large aperture were selected. The basic characteristics of the dipole and quadrupoles are listed in Table 3.
- Enough separation power. In order to obtain sufficient separation power, the focal-plane dispersion should be larger than 5 mm per 1 % rigidity change, whereas for the measurement of secondary reaction, the beam spot size should be confined to 2 cm in diameter. In practice, a compromise was made between the dispersion and the beam-spot size.

Table 3: The specifications of the electromagnetic components of the secondary beam line GIRAFFE.

Dipole magnet (D)	Quadrupole lens ( $Q_1$ , $Q_2$ )
Magnet gap 10.0 cm	Aperture 13.9 cm
Maximum field 6.5 kG	Maximum field gradient 435 Gs/cm
Radius of effective deflection 2.2 m	Effective length 0.36 m
Deflection angle $13^\circ$	

As a result, a D-Q-Q configuration was selected. The geometrical arrangement of each component and the beam envelope calculated by using the TRANSPORT code are shown in Figure 4. The basic parameters of this beam line are presented in Table 1. The final layout of GIRAFFE facility is shown in Figure 1.

## 6.5 Beam production

### 6.5.1 Beam tuning procedure

The RNB tuning procedure was performed in the following steps:

1. The initial D-Q-Q current setting. A computer code (RNBSET), which gave the initial field setting parameter for the desired RNB, was developed. It involves the magnetic field calibration data for each component, beam optics calculation, reaction kinematics, and energy loss calculation.
2. Adjustment of the primary beam position by tuning the electrostatic deflector upstream the primary target. The deviation of the primary beam spot from the optical center was found to cause a severe decrease in the transmission efficiency for RNB and an increase of the multiple scattering of the primary beam in the beam pipe, thus significantly decreasing the beam purity.
3. Fine-tuning of D-Q-Q fields. The beam purity had a strong dependence on the D setting and a weak dependence on the  $Q_1$  and  $Q_2$  settings since the latter only change the beam focus. It was found that the deviations of the magnetic field values between the RNBSET results and final field settings were less than 5 % for the dipole and less than 3 % for  $Q_1$  and  $Q_2$ .

## 6.6 Purification of RNB

It can be seen from the energy spectra of RNB that the contaminants come from secondary products of other reaction channels and from the low energy tail of the primary beam, which fall into the selected rigidity window due to multiple coulomb scattering. In order to study the purity of RNB, two acceptance angle settings of GIRAFFE ( $0^\circ$  and  $3^\circ$ ) were used and a shadow bar was installed in the case of  $0^\circ$  setting. The corresponding results are listed below:

In the  $0^\circ$  setting, the installation of the shadow bar allows to eliminate low energy beam contaminant. This results from the fact that the primary beam components have smaller emittance than that of secondary beam. The purity of  $^{11}\text{C}$  beam was increased from 6 % to 14 % by installing the shadow bar.

In the  $3^\circ$  setting, the purity of RNB (with the shadow bar removed) is higher than that obtained at  $0^\circ$  with the shadow bar. This is due to the Coulomb scattering cross section, which is proportional to  $\sin^4(\theta/2)$ ,  $\theta$  being the acceptance angle. Setting acceptance angle values other than  $0^\circ$  can greatly reduce the accepted scattering primary beam, whereas the differential cross section of RNB is similar to that at  $0^\circ$ . Another advantage of such a setting is that the shadow bar is not necessary, since the center of primary beam and scattered component is automatically avoided, thus increasing the transmission for RNB. The drawback of the  $3^\circ$  setting is the slightly lower energy resolution of RNB, which is due to the kinematics.

## 6.7 Production of secondary beams

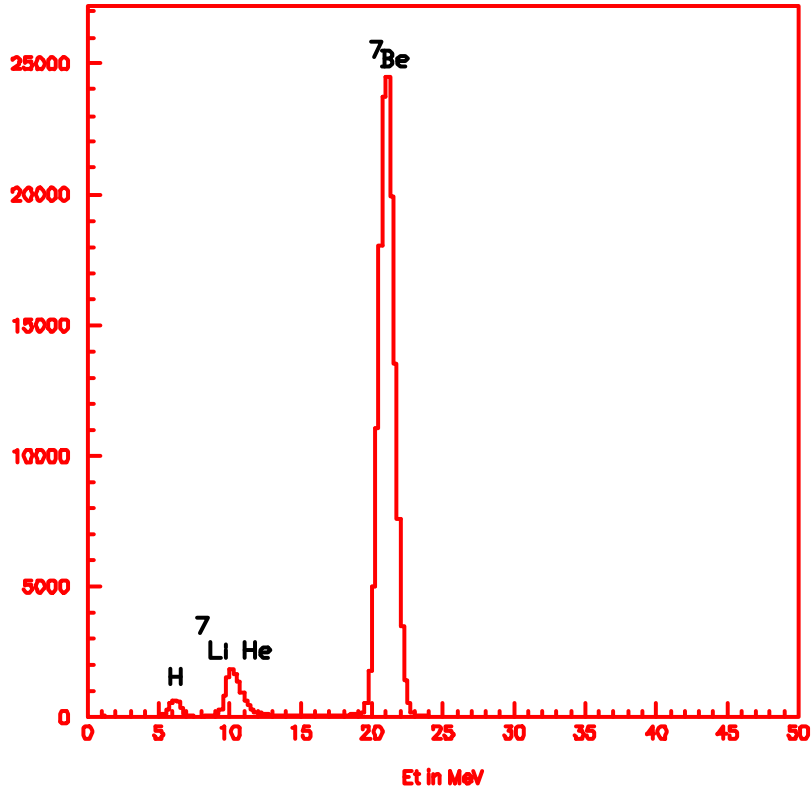


Figure 5: Energy spectra of  $^7\text{Be}$  beam and contaminants of  $^7\text{Li}$ , He and H isotopes.

In the RNB production experiments, a gas cell at 1.2 atm pressure was used as the target, the entrance and exit windows being made of  $\sim 2.5 \text{ mg/cm}^2$  thick titanium foils. The RNB were measured by using a  $\Delta E$ -E counter telescope consisting of an ionization chamber filled with P-10 gas backed by a  $45 \times 45 \text{ mm}^2$  Hamamatsu two-dimensional position-sensitive silicon detector (PSSD) of  $450 \text{ }\mu\text{m}$  in thickness. So far, the production of the  $^6\text{He}$ ,  $^7\text{Be}$ ,  $^{11}\text{C}$ ,  $^{13}\text{N}$ , and  $^{17}\text{F}$  beams has been tested. The characteristics of these beams are summarized in Table 4. As examples, the energy spectra of  $^7\text{Be}$  and  $^6\text{He}$  are shown in Figure 5 and Figure 6, respectively. The position profile for  $^7\text{Be}$  beam is presented in Figure 7.

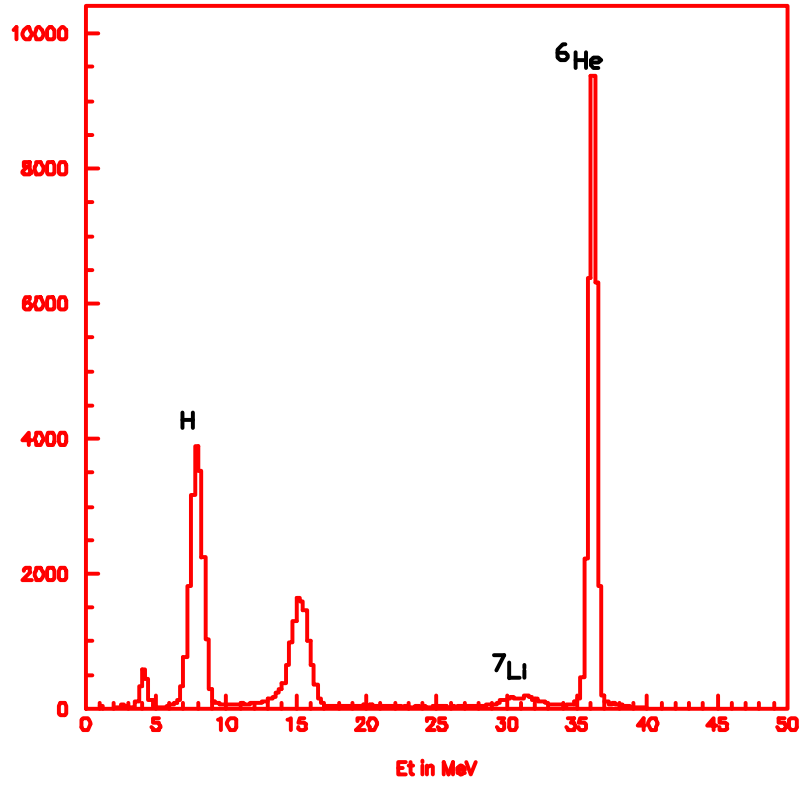


Figure 6: Energy spectra of  ${}^6\text{He}$  beam with contaminants of  ${}^7\text{Li}$  and H isotopes.

Table 4: Summary of the produced RNB

RNB	Reaction	Energy ( MeV )	FWHM (MeV)	Purity ( % )	Conversion Ratio
${}^6\text{He}$	${}^2\text{H}({}^7\text{Li}, {}^6\text{He}){}^3\text{He}$	35.3	0.7	43	$3.4 \times 10^{-8}$
${}^7\text{Be}$	${}^1\text{H}({}^7\text{Li}, {}^7\text{Be})\text{n}$	23.0	1.3	92	$2.1 \times 10^{-7}$
${}^{11}\text{C}$	${}^1\text{H}({}^{11}\text{B}, {}^{11}\text{C})\text{n}$	38.2	2.7	85	$6.8 \times 10^{-8}$
${}^{13}\text{N}$	${}^2\text{H}({}^{12}\text{C}, {}^{13}\text{N})\text{n}$	65.7	2.3	6	$6.0 \times 10^{-8}$
${}^{17}\text{F}$	${}^2\text{H}({}^{16}\text{O}, {}^{17}\text{F})\text{n}$	74.9	4.8	24	$6.6 \times 10^{-7}$

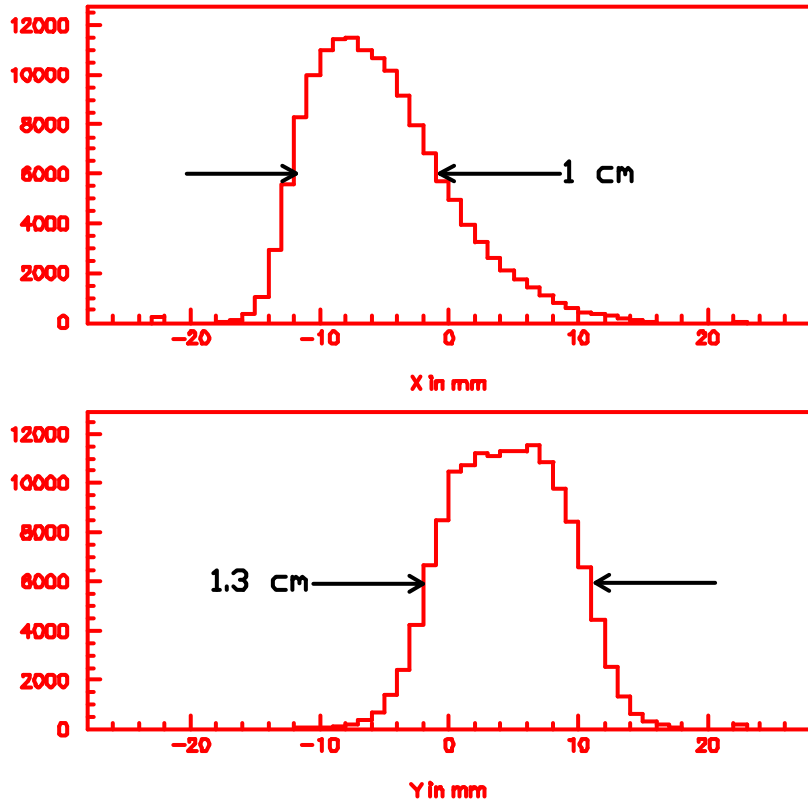


Figure 7: Position profiles for the  $^7\text{Be}$  beam. The horizontal arrows show the FWHM of beam profiles.

## 6.8 Future developments

The possible improvements of GIRAFFE are planned into two phases.

For the phase I, a beam swinger will be installed in front of the primary target chamber. It was designed for altering the incident angle of the primary beam on target, so that one can select the optimal acceptance angle for each RNB. Velocity filter and beam-switcher are planned to be installed in front of the focal plane. In addition, a velocity filter will be used to enhance the secondary beam selection, see Section 5.3 of Appendix 1. Taking the  $^7\text{Be}$ -beam production as an example, the velocity filter will effectively filter out  $^7\text{Li}$  contaminants, since the  $^7\text{Li}$  ions have the same magnetic rigidity but different charge states, thus different velocity. The beam switcher will be used to serve for the decay measurement. During such a measurement, RNB itself will be switched off, so that background will be effectively reduced.

A detector setup for decay measurement was also considered in phase I. This setup will include implantation/detection silicon detectors and germanium detectors to detect the  $\gamma$ -rays in the decay process. A helium-jet technique can be used to transport the RNB to a detector station with lower background. This measure will also improve the implantation profile in range and in beam spot.

The GIRAFFE improvement phase II consists of adding a second-stage magnetic separation, so that an energy degrader can be placed in the intermediate focal plane, which will allow double achromatic operation with isotopic selection.

The upgrading of the focal plane detector is also planned. A general detector chamber was designed, which will cover larger angular range than current setup. In addition, the use of a MUSIC detector is planned. This detector has better  $\Delta E$  resolution and provides the possibility of measuring the excitation function in a single setting of GIRAFFE, by using the gas of the MUSIC both for detection and as a secondary target.

All the above-proposed improvements are summarized in the Figure 8.

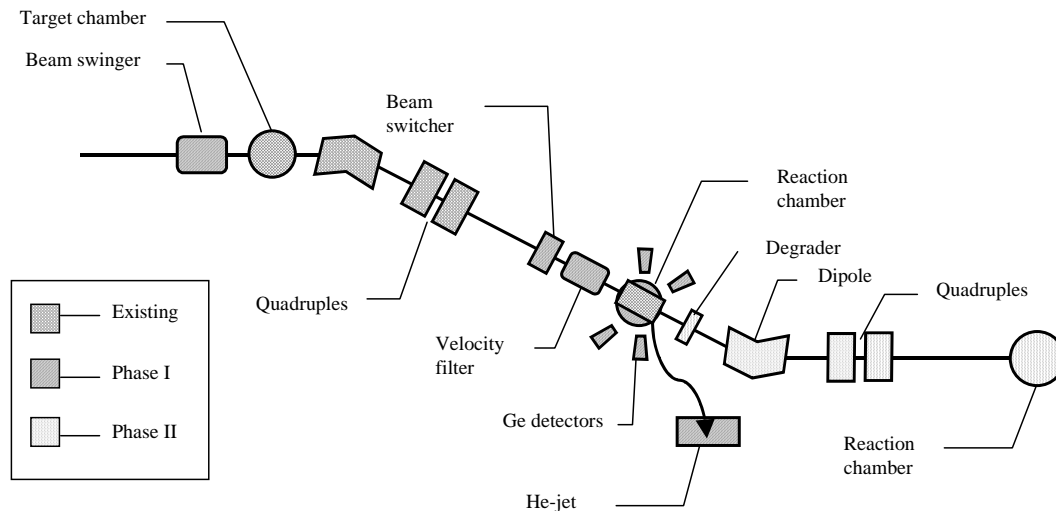
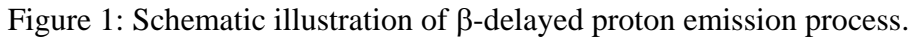


Figure 8: The future developments of GIRAFFE.

The decay mode known as  $\beta$ -delayed proton emission consists of two consecutive decay processes, i.e.  $\beta$ -decay and proton emission. The general decay scheme shown in Figure 1 exemplifies this disintegration mode for a typical  $\beta^+$ -delayed proton precursor. The  $\beta$ -decay of the precursor populates states in the emitter, many of which lie above the proton separation energy ( $S_p$ ). These levels then decay via proton emission to states in the daughter nucleus, as summarized in Figure 1. Thus the experiment involves the observation of protons that exhibit the half-life of the precursor. The proton energies are determined by the excitation energy of the  $\beta$ -populated state in the emitter and by the  $S_p$  values of the states in the daughter. The observed proton intensities are used to obtain  $\beta^+$ -decay transition rates and to determine the relative reduced proton widths for proton emission to various final states. These observations provide a challenging test for shell-model calculations.



By a standard application of time-dependent perturbation theory, the probability of emitting a  $\beta$ -particle with energy  $E$  and momentum  $p$  is given by

where  $M_{fi}$  is the  $\beta$ -decay matrix element connecting the initial and final states,  $F(Z,E)$  is the Fermi function which takes into account the Coulomb distortion of the charged



lepton's wave function form that describes a free particle (i.e., a plane wave) due to the nuclear charge and the surrounding atomic electrons,  $Z$  is the atomic number of the  $\beta$ -daughter, and  $E_0$  is the maximum  $\beta$ -particle energy (for  $\beta^+$ -decay:  $E_0 = Q_{EC} - E_x - 2m_e c^2$ ). The  $\beta$ -decay constant ( $\lambda$ ) for a particular transition is obtained by integrating this probability over all allowed energies

$$\lambda = \frac{1}{2\pi^3 \hbar^7 c^5} |M_{fi}|^2 \int_0^{E_0} F(Z, E) (E_0 - E)^2 p E dE .$$

The integral in the above equation is known as the statistical rate function or phase space factor  $f$ . Substituting  $f$ , which can be expressed in units of  $(m_e c^2)^5/c$ , in this equation, and rewriting the relationship in terms of partial half-life,  $t = \ln 2/\lambda$ , one obtains the comparative half-life for the transition or its  $ft$  value.

$$ft = \frac{2\pi^3 (\ln 2) \hbar^7 / m_e c^4}{|M_{fi}|^2} .$$

Comparative half-lives (often quoted as  $\log ft$ 's) tend to fall into certain groups that enable  $\beta$ -transitions to be classified in terms of superallowed, allowed, or forbidden transitions, see Table 1 for detail. Once a particular decay is classified, the spin, parity, and isospin of the populated level is restricted to certain values governed by the selection rules for that type of transition. Since the present work only deals with superallowed and allowed transitions, the discussion will be limited to those decays.

Table 1: List of classification of  $\beta$ -transitions and corresponding selection rules.

Class	$\log ft$	L	Fermi transition		Gamow-Teller transition	
			$\Delta I$	$\Delta \pi$	$\Delta I$	$\Delta \pi$
Superal- lowed	2.9-3.7	0	0	No	(0), 1	No
Allowed	< 5.9	0	0	No	(0), 1	No
1 <sup>st</sup> forbid- den	> 8.0	1	(0), 1	Yes	0, 1, 2	Yes
2 <sup>nd</sup> for- bidden	> 10.6	2	(1), 2	No	2, 3	No

For allowed and superallowed transitions, the  $\beta$ -decay matrix element can be divided into two parts, the Fermi matrix elements ( $I$ ) and that of Gamow-Teller (GT) matrix elements ( $\sigma$ ), together with their respective vector and axial vector coupling constants,  $g_V$  and  $g_A$ , as

$$|M_{fi}|^2 = g_V^2 \langle I \rangle^2 + g_A^2 \langle \sigma \rangle^2 ,$$

where the coupling constants have been renormalized to include electromagnetic corrections. Combining the above equations, one obtains the familiar relation

$$ft = \frac{2\pi^3 (\ln 2) \hbar^7 / m_e^5 c^4}{g_V^2 \langle l \rangle^2 + g_A^2 \langle \sigma \rangle^2}.$$

Using the most recent values for the physical constants, together with the latest values of the renormalized coupling constants, leads to [TRI95B],

$$ft = \frac{6127(9)}{\langle l \rangle^2 + 1.567 \langle \sigma \rangle^2} s.$$

The Fermi matrix element is given as

$$\langle l \rangle = \left\langle \psi_f \left| \sum_j \tau_{\pm}(j) \right| \psi_i \right\rangle = \langle \psi_f | T_{\pm} | \psi_i \rangle,$$

where i and f represent the initial and final wave functions,  $\tau$  is the isospin raising or lowering operator for the  $j^{\text{th}}$  nucleon (i.e., for  $\beta^+$ -decay,  $\tau_+ p = n$ ), and the sum of the  $j$  operator over all  $j$  nucleons is defined as the total isospin operator  $T$ . Analogous to the angular momentum raising and lowering operator  $J$ , the isospin operator raises or lowers the isospin projection,  $T_z$ , by one unit, thus

$$T_{\pm} | \psi(J^{\pi}, T, T_z) \rangle = \left[ (T \mp T_z) (T \pm T_z + 1) \right]^{1/2} | \psi(J^{\pi}, T, T_z \pm 1) \rangle$$

Correspondingly, the selection rules for allowed Fermi interactions are  $\Delta J^{\Delta\pi} = 0^{(no)}$  and  $\Delta T = 0$ . Neglecting the small isospin impurities in the final wave function, the Fermi matrix element becomes

$$\langle l \rangle^2 = T(T+1) - T_{zi} T_{zf},$$

where  $T_{zi}$  and  $T_{zf}$  are the initial and final isospin projections.

The GT matrix element is given by

$$\langle l \rangle = \left\langle \psi_f \left| \sum_j \sigma(j) \tau_{\pm}(j) \right| \psi_i \right\rangle,$$

where  $\sigma(j)$  is the Pauli spin operator. The selection rules for allowed GT interactions are  $\Delta J^{\Delta\pi} = 0, 1^{(no)}$  and  $\Delta T = 0, 1$ . Unlike the Fermi matrix element, this matrix element depends upon the explicit details of the initial and final wave functions. Within the simplest shell-model, where initial and final states are described by a single particle coupled to an inert  $J = 0$  core (i.e.,  $\left[ l_j \otimes \left( l_j \right)_{J=0}^n \right]_{J=j}$ ), the GT matrix element is given by

$$\langle \sigma \rangle^2 = 6(2J_f + 1) \left\{ \begin{matrix} 1/2 & 1/2 & 1 \\ J_i & J_f & l \end{matrix} \right\}^2,$$

where the term enclosed by brackets is a Wigner 6j symbol. This expression applies to allowed transitions between single particle state where  $J_i = 1 + 1/2$  such as a  $1d_{5/2} \rightarrow 1d_{3/2}$  transition.

Unfortunately, due to configuration mixing, most nuclear states can not be accurately expressed by only one shell-model configuration, but require wave functions consisting of several different shell-model configurations. Shell-model calculations,

which allow configuration mixing between a large variety of different configurations restricted by the basis space covered, have proven to be very successful in predicting various experimental observables, see Section 7.3 for details.

## 7.2 IMME mass predictions

From the observed proton decay energy of the IAS as measured in this work, one can determine the mass excess of the IAS (if the ground state mass excess is known), which can then be used to predict the precursor's mass through the use of isobaric multiplet mass equation (IMME). As shown by Wigner [WIG57] the mass of an isobaric multiplet member with isospin  $T$  and isospin projection  $T_z$  is given by the following quadratic relation

$$M(T_z) = a + bT_z + cT_z^2$$

Thus if one knows the masses of all but one members of a multiplet, one can calculate the mass of the remaining members.

In the following, this method is used to deduce the ground state mass excess of  $^{40}\text{Ti}$  and the  $Q_{EC}$  value of  $^{40}\text{Ti}$   $\beta$ -decay, based on our measured  $^{40}\text{Sc}$  IAS state excitation energy. Table 2 summarizes the list of input data for the IMME fit procedure.

Table 2: Masses and  $T=2$  excited states of  $A = 40$ ,  $T = 2$  series.

Nucleus	$T_z$	G.S. mass excess (keV)	$E_x$ of $T=2$ states (keV)	$T=2$ states mass excess (keV)
$^{40}\text{Ar}$	2	-35039.891(5)	0	-35039.891(5)
$^{40}\text{K}$	1	-33535.0(3)	4384.0(3)	-29151.0(4)
$^{40}\text{Ca}$	0	-34846.0(3)	11988(2)	-22858(2)
$^{40}\text{Sc}$	-1	-20526(4)	4365(8) <sup>a</sup>	-16161(9)
$^{40}\text{Ti}$	-2	To be determined	0	To be determined

<sup>a</sup>Measured in this work and the work of Trinder et al. [TRI97B].

Based on these data, the polynomial fits were performed, which yielded the coefficients as listed in Table 3.

Table 3: List of polynomial fit constants.

Set	Fit condition	a (keV)	b (keV)	c (keV)
I	$^{40}\text{Ar}$ , $^{40}\text{K}$ , $^{40}\text{Ca}$ (this work)	-22858.0(16)	-6495.2(24)	202.0(8)
II	$^{40}\text{Ar}$ , $^{40}\text{K}$ , $^{40}\text{Ca}$ , and $^{40}\text{Sc}$ (this work)	-22858.0(16)	-6495.1(24)	202.1(8)
III	$^{40}\text{Ar}$ , $^{40}\text{K}$ , $^{40}\text{Ca}$ ,	-22857.9(16)	-6495.2(24)	202.1(8)

Using the constants from Set I, the excitation energy of  $^{40}\text{Sc}$  IAS state was calculated to be 4365 keV, compared with experimental value of 4365(8) keV. The excellent agreement shows that the IMME prediction is reliable enough to predict the  $^{40}\text{Ti}$  ground state mass excess. The fit procedure was extended by including the measured  $^{40}\text{Sc}$  IAS excitation energy. This resulted the constants marked as Set II, which is supported by the results in [TRI97B] (Set III). By using these constants, the ground state mass excess was predicted and the  $Q_{EC}$  value for  $^{40}\text{Ti}$  was determined to be -9060(12) keV and 11466(13) keV, respectively. These values are considerably more precise than the previous values of -8850(160) keV and 10680(160) keV given in [AUD97], which were based on a systematic mass evaluation.

### 7.3 Neutrino absorption calculation

In calculating the neutrino capture cross section for the reaction  $\nu_e + ^{40}\text{Ar} \rightarrow ^{40}\text{K}^* + e^-$ , all states in  $^{40}\text{K}$  with excitation energy up to the particle-decay threshold at 7.58 MeV [9] have to be considered. The cross section for absorbing a neutrino with energy  $E_\nu$  from the ground state of  $^{40}\text{Ar}$  to the  $i^{\text{th}}$  excited state in  $^{40}\text{K}$  is given by

$$\sigma_i(E_\nu) = \frac{G_v^2}{\pi c^3 \hbar^4} |M_{if}|^2 E_e^i k_e^i F(Z, E_e^i).$$

where  $E_e^i = E_\nu - Q_i + m_e c^2$ .

The total absorption cross section for solar neutrinos is obtained by folding this cross section with the normalized solar neutrino flux  $\Phi(E_\nu)$ , and summing contributions due to excited states, i.e.

$$\Sigma_{tot} = \sum_i \Sigma_i = \sum_i \int_{Q_i + E_{cut}}^{\infty} \Phi(E_\nu) \sigma_i(E_\nu) dE_\nu.$$

The quantity  $E_{cut} = 4.489$  MeV is the minimum electron kinetic energy observable in the ICARUS detector, while the function  $\Phi(E_\nu)$  associated with the  $^8\text{B}$  spectrum was taken from [BAH95]. In this calculation, the above relations are simplified as

$$\Sigma_i = \aleph(E_x(i)) |M_{if}|_i^2,$$

with  $|M_{if}|_i^2 = (B(F) + B(GT))_i$ .

According to [ORM95], the function  $\aleph(E_x)$  can be parameterized as

$$\aleph(E_x) = \sum_{i=0}^3 a_i E_x^i,$$

with  $a_i$  being 8657.7, -3035.7, 349.61, and -13.105 respectively. This relation is shown in Figure 2. Multiplying  $\Sigma_{tot}$  by the total integrated neutrino flux  $\mathfrak{F}(^8\text{B}) = 6.6_{-1.6}^{+1.3} \times 10^6 \text{ cm}^{-2} \text{ s}^{-1}$  [BAH95], one obtains the neutrino capture rate on  $^{40}\text{Ar}$  as,

$$\Re(^{40}\text{Ar}) = \sum_i \Re_i(^{40}\text{Ar}) = \Sigma_{tot}(^{40}\text{Ar}) \Im(^8\text{B}) = 9.4 \pm 0.2(\text{stat.})^{+1.3}_{-1.6}(\text{syst.}) \text{ SNU} .$$

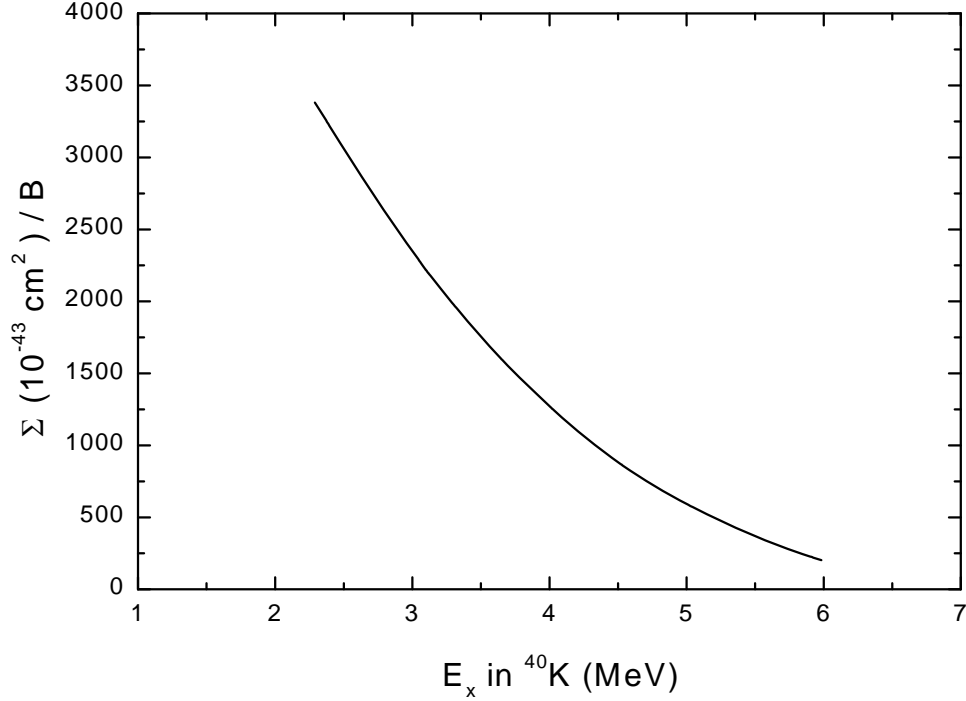


Figure 2: The ratio of neutrino absorption cross-section for  $^{40}\text{Ar}$  over decay strength as a function of excitation energy in  $^{40}\text{K}$ .

#### 7.4 Spherical Shell-Model

The increased binding of certain combinations of neutrons and protons was pointed out by Elsasser [ELS34] in 1934, and this effects for light nuclei with N or Z values of 2 ( $^4\text{He}$ ), 8 ( $^{16}\text{O}$ ), and 20 ( $^{40}\text{Ca}$ ) were already known in these early days of nuclear physics. In 1948 Mayer [MAY48] observed strong evidence for additional "magic numbers" at 50 and 82 for protons, and 50, 82, and 126 for neutrons. This phenomenon can be clearly seen from the 2p or 2n separation energies along lines of constant isospin for even-even nuclei. Mayer and Jensen [MAY55] explained this in terms of a "shell-model", where nucleons are bound by a spherically symmetric potential well. If a harmonic oscillator of the form

$$V(r) = -V_0[1-(r/R)^2]$$

is used, where  $V(r)$  is the potential at a distance  $r$  from the center of the nucleus and  $R$  is the nuclear radius, the resulting quantum states can be characterized by  $n$ , the principal quantum number related to the number of radial nodes in the wave function, and by  $l$ , the orbital angular momentum of the particle. By analogy to atomic spectroscopy, states with  $l = 0, 1, 2, 3, 4, 5, 6, \dots$  are designated as s, p, d, f, g, h, i, ..., respectively. The states are identified by as 1s, 2f, 3p, etc, where, unlike in atomic spectroscopy,  $n$  is defined so that each state has  $n-1$  radial nodes.

The solution of the Schrödinger equation for the isotropic harmonic oscillator gives the level energies

$$E = \hbar \omega_0 [2(n-1) + 1] + E_0,$$

where  $\omega_0 = [2V_0/M/R^2]^{1/2}$ ,  $M$  is the nucleon mass, and  $E_0 = 3/2 \hbar \omega_0$ . Here states with the same value of  $N=2(n-1) + 1$  are degenerate, and states of a given energy must all have either even or odd values of  $l$ . Thus, degenerate states must have the same parity.

Mayer [MAY50] and Haxel *et al* [HAX50] showed that the interaction between the intrinsic angular momentum (spin) of the particles and their total angular momentum would split the orbital into two sub-states with  $l \pm 1/2$  (e.g.  $1p_{1/2}$  and  $1p_{3/2}$ ). These states are then no longer degenerate, and it was shown that, if the "spin-orbit" interaction is of the same order as the spacing between oscillator shells, states with  $j = l+1/2$  are more stable than states with  $j = l-1/2$  and the magic numbers can be reproduced. The evolution of shell-model states from the harmonic oscillator model is depicted in Figure 3.

In the shell-model calculation, the interaction between the valence particles and the core nucleus is treated by the perturbation theory. Because of the large valence space of  $^{40}\text{Ti}$ , the two major oscillator shells must be included in the calculation, e.g. the  $1d_{5/2}2s_{1/2}1d_{3/2}$  (sd) and the  $1f_{7/2}2p_{3/2}1f_{5/2}2p_{1/2}$  (fp) shells. Correspondingly, the number of possible configurations of the model space in the shell-model calculation is as large as  $10^6$ . To truncate the model space, the  $n\hbar\omega$  truncation was imposed [ORM95].

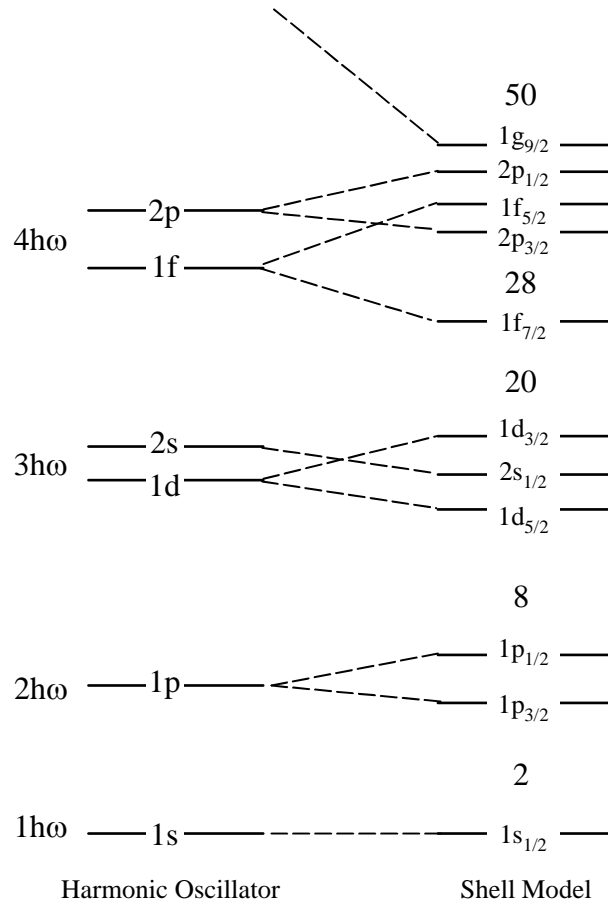


Figure 3: Evolution of nuclear level from the harmonic oscillator model to the shell-model.

## 8 Appendix 4: Formulae for deducing s factors

### 8.1 Formulae concerning S factors

To separate the energy dependence of the cross section due to nuclear structure and Coulomb penetration factor, respectively. The following equations are used for extrapolating the low energy of astrophysical interest.

$$S(E) = \sigma(E) E e^{2\pi\eta} ,$$

$$2\pi\eta = 31.29 Z_1 Z_2 \sqrt{\frac{\mu}{E}} ,$$

where  $Z_1$  and  $Z_2$  are the atomic number of interacting particles, and  $\mu$  the reduced mass;  $E$  the center-of-mass energy in keV.

For the non-resonant part, the polynomial formula is used for describing the remaining energy dependence of a S factor.

$$S(E) = S(0) + S'(0)E + \frac{1}{2} S''(0)E^2 .$$

In the low-energy range (tens of keV), the cross section is enhanced by the lowering of Coulomb barrier due to electron screening, which is the typical situation of terrestrial experiment performed for determining the low-energy cross sections. In this context, cross sections of bare nuclei or of nuclei in different charge states ought to be considered in any solar model. This can be achieved by introducing a screening factor

$$f_{lab}(E) = \frac{\sigma_s(E)}{\sigma_b(E)} \approx e^{\frac{\pi\eta U_e}{E}} ,$$

where  $U_e$  is the electron-screening energy, the above equation results from the equivalent energy shift of incident energy by an amount of  $U_e$ , which is of the order of the electron binding energy

$$U_e \approx \frac{Z_1 Z_2 e^2}{R_a} , \text{ with } R_a \text{ being atomic radius.}$$

The approximate dependence of the solar neutrino fluxes on different low-energy nuclear cross-section factors [ADE97] is summarized in the following equations. They are useful in estimating the dependence of individual neutrino flux on the nuclear cross section.

$$\phi(pp) \propto S_{11}^{0.14} S_{33}^{0.03} S_{34}^{-0.06}$$

$$\phi({}^7\text{Be}) \propto S_{11}^{-0.97} S_{33}^{-0.43} S_{34}^{0.86}$$

$$\phi({}^8\text{B}) \propto S_{11}^{-2.6} S_{33}^{-0.40} S_{34}^{0.81} S_{17}^{1.0} S_{e-7}^{-1.0}$$

### 8.2 Formulae concerning the $S_{17}(0)$ factor from one-proton transfer reaction

The  $(p, \gamma)$  reaction ( $A+x \rightarrow B+\gamma$ ), also called radiative capture, are divided into the direct capture and compound nucleus capture. Since the transfer reaction is only related to the direct process, only this process is discussed here.



This cross-section can be calculated by using the matrix elements of an E1 electric operator, in which the wave function of incident and out-going channels are used. These wave functions can be separated into  ${}^7\text{Be-p}$  part and  ${}^8\text{B-}\gamma$  part. The cross section of the process is described by a matrix element:

$$\sigma \propto \left| \langle B | O | A + x \rangle \right|^2,$$

where O is the E1 operator. Since the particle A have to penetrate the Coulomb and centrifugal barrier. Such reaction cross section is vanishingly small.

The bridge to link this matrix element to the transfer reaction is their common overlap factor, if A and B are the same in both cases. The detailed treatment [TAN97] yields

$$\sigma(E1) \propto R^2,$$

where  $R = \int_0^\infty u_x(r) O(r) u_B(r) r^2 dr$  and u is the radial part of the bound state wave

function that takes the shape of the Whittaker function at  $r > R_N$  (nuclear radius). The integration R has its maximum outside nucleus. In fact, only the tail of the wave function determines this integral. It was proved that above matrix element could be determined by the peripheral behavior of the wave functions, that is, radical part of wave functions out side the surface of nucleus. At this region, the shape of wave function is best described by the Whittaker function. This can be expressed as,

$$u = c_{lj} W_{-\eta, l+1/2}(2kr) / r$$

The only quantity one need to know is the normalization factor for the Whittaker function. This parameter is called asymptotic normalization constant (ANC). So finally the determination of (p,g) cross section is converted to the determination of ANC ( $c_{lj}$ ).

As suggested by the work of Xu *et al.* [Xu94], it is possible to deduce the ANC from one-proton transfer reaction on  ${}^7\text{Be}$ . This idea was based on the separation of the wave functions mentioned above, and on the fact that by transfer reaction, such as  ${}^7\text{Be}(d,n){}^8\text{B}$ , the peripheral part of  ${}^7\text{Be}$  and  ${}^8\text{B}$  part of wave function can be experimentally determined.

Now we discuss the transfer reaction  $A(a,b)B$ , its matrix element is give by

$$m = \langle bB | V | aA \rangle$$

If we select the appropriate beam energy, in which the direct transfer process dominate, we are dealing with the peripheral reaction so that,

$$m = c_{lj} W_{-\eta, l+1/2}(2kr) / r \Big|_{R_N}^\infty$$

here the ANC is exactly the same for the (p, $\gamma$ ) reaction.

Now we go to practical procedure for  ${}^7\text{Be}(d,n){}^8\text{B}$  reaction. The  $S_{17}(0)$  factor is related to the cross section of  ${}^7\text{Be}(p,\gamma){}^8\text{B}$  at zero energy. The treatment was base on the calculation of  ${}^7\text{Be}(p,\gamma){}^8\text{B}$  reaction, so that the  ${}^7\text{Be}$  and  ${}^8\text{B}$  wave function can be used to assemble  ${}^7\text{Be-p}$  and  ${}^8\text{B-}\gamma$  wave function. Firstly we compare the experimental angular distribution and that calculated by DWBA,

$$\sigma_{\text{exp}}(\theta) - \sigma_{\text{CN}}(\theta) = S_{lj} \sigma_{\text{DWBA}}(\theta)$$

where  $S_{lj}$  is the spectroscopic factor. We also have

$$C_{lj}^2 = S_{lj} b_{nlj}^2$$

where  $b_{nlj}$  can be deduce from,

$$u_{nlj}(r) = b_{nlj} W_{-\eta, l+1/2}(2\kappa r) / r, \quad r \geq R_N$$

With this relation

$$C_{lj}^2 = S_{lj} b_{nlj}^2 = S_{1,0} b_{nlj}'^2$$

In the case of  $S_{1,0} = 1.0$ , Xu *et al.* [XU94], pointed out that

$$S_{17}(0) = b_{nlj}'^2 / 0.026$$

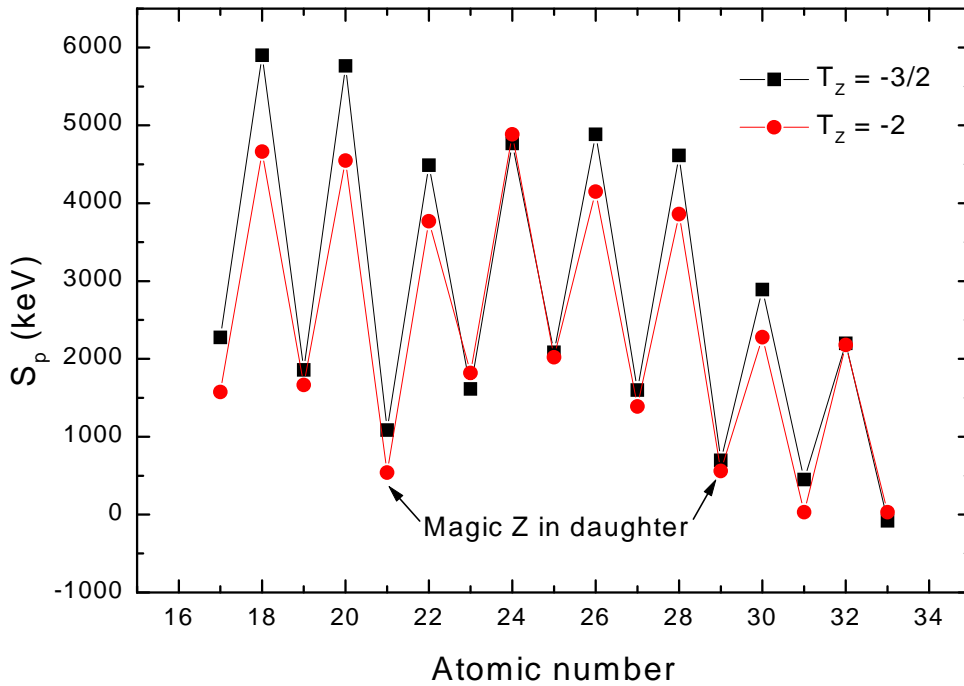
So Finally we can get  $S_{17}(0)$  value. See also Chapter 2 for the description of corresponding DWBA calculations.

This approach is of course not limited to the  ${}^7\text{Be}(p,\gamma){}^8\text{B}$  reaction, but is applicable to all  $(p,\gamma)$  reactions, such as  ${}^{11}\text{C}(p,\gamma){}^{12}\text{N}$ , many of those being of astrophysical interest. To do this the relevant assembling relations should be reliably calculated done in the case of  ${}^7\text{Be}(p,\gamma){}^8\text{B}$ . The transfer reactions induced by RNB and stable beam can be served as an independent way to determine  $(p,\gamma)$  reaction of astrophysical interest. The transfer reactions have cross sections that are many order of magnitude higher than  $(p,\gamma)$  reactions. Meanwhile, they can be directly connected the S factors at zero energy whereas normal  $(p,\gamma)$  measurements have a limitation of the lowest reachable proton energy so that the theoretical extrapolations have to be made.

## 9. Appendix 5: Further discussions on proton separation energy

### 9.1 Proton separation energy and proton branching ratio

The occurrence of a  $\beta$ -delayed proton branching ratio close to 100 % for  $^{40}\text{Ti}$  and  $^{41}\text{Ti}$  is due to two effects. On the one hand, the  $\beta$ -decay of  $^{40}\text{Ti}$  ( $0^+$ ) and  $^{41}\text{Ti}$  ( $3/2^+$ ) to the ground state of  $^{40}\text{Sc}$  ( $4^+$ ) and  $^{41}\text{Sc}$  ( $7/2^+$ ), respectively, is forbidden. On the other hand, *all* excited levels of  $^{40}\text{Sc}$  and  $^{41}\text{Sc}$ , populated in  $\beta$ -decay, are unbound against proton emission. This feature reflects the fact that, as the proton emitting nucleus (Sc) has odd- $Z$  and its proton daughter (Ca) represents a proton shell closure ( $Z=20$ ), the proton separation energies  $S_p$  for  $^{40}\text{Sc}$  and  $^{41}\text{Sc}$  are unusually low, i.e. 539(4) keV and 1085.07(9) keV, respectively [AUD97]). If one extends such simple considerations from  $^{40}\text{Ti}$  to heavier nuclei of the  $T_z = -2$ ,  $A = 4n$  series, one would expect  $^{56}\text{Zn}$  to also be a pure  $\beta$ -delayed proton emitter. The corresponding extension of the  $T_z = -3/2$ ,  $A = 4n+1$  series beyond  $^{41}\text{Ti}$  also explains the observation of  $\beta$ -delayed protons from  $^{57}\text{Zn}$



[VIE76]. This interpretation is illustrated in Figure 1.

Figure 1: Proton separation energies of the  $T_z = -2$ ,  $A = 4n$  and the  $T_z = -3/2$ ,  $A = 4n+1$  series. The positions for  $^{40}\text{Ti}$  and  $^{56}\text{Zn}$  are indicated by arrows.

The above phenomenon can be explained on the basis of the shell-model.  $^{40}\text{Ti}$ , for example, has 22 protons and 18 neutrons, i.e. two valence protons and two neutron holes, that are most probably located in the shell-model orbitals  $1f_{7/2}$  and  $1d_{3/2}$ , respectively. In the  $\beta$ -delayed proton emission of  $^{40}\text{Ti}$ , one of the valence protons fills the neutron hole in  $^{40}\text{Sc}$ , with the remaining valence proton being emitted to form a

$^{39}\text{Ca}$  nucleus with a closed proton shell and one neutron hole. It is the effect of the proton shell closure that makes the proton separation energy of  $^{40}\text{Sc}$  as low as 539 keV.

## 9.2 Decay measurement for $^{56}\text{Zn}$

Following the discussion on the  $S_p$  systematics in Chapter 4.4, an interesting candidate for the study of  $\beta$ -decay along the  $T_z=-2$  line is  $^{56}\text{Zn}$ . The  $\beta$ -decay daughter  $^{56}\text{Cu}$  has a low  $S_p$  value of 560(140) keV [AUD97] (see also Figure 1). Therefore, the most favorable decay mode for  $^{56}\text{Zn}$  is expected to be  $\beta$ -delayed proton emission. Such a study will provide the possibility of testing the isospin symmetry in this mass region, since the  $^{56}\text{Fe}(p,n)^{56}\text{Co}$  reaction data are already available [WAN88]. In addition, the experimental results can be compared with the shell-model predictions [CAU98] as a means to further investigate the GT-quenching in fp-shell. This study may also be relevant to astrophysics, since the experimental  $\beta$ -decay properties of  $^{56}\text{Zn}$  would eventually modify the path of the rp-process.

However, the production of  $^{56}\text{Zn}$  is a difficult task. Although the early study of  $^{57}\text{Zn}$  [VIE76] showed that it may be produced via fusion-evaporation reaction, the experimental results from the production of  $^{58}\text{Zn}$  at ISOLDE and at the GSI mass separator showed its secondary beam intensity to be lower from fusion-evaporation reactions than from spallation reactions. The alternative way is to use projectile fragmentation reactions. The most suitable projectile is  $^{64}\text{Zn}$ , but according the EPAX calculation, the cross section is only  $2.5 \times 10^{-7}$  mb, i.e. 2 orders of magnitude lower than that of  $^{40}\text{Ti}$ . At GANIL [POU87], it was found that multi-nucleon transfer reaction, at intermediate energies offer favorable cross sections for producing proton-rich isotopes with atomic numbers larger than that of the projectile. This method led to the discovery of new proton-rich isotopes such as  $^{61}\text{Ga}$ ,  $^{63}\text{Ge}$ , and  $^{65}\text{As}$  by using  $^{64}\text{Zn}$  projectiles. According to these studies, the production cross section of  $^{56}\text{Zn}$  via transfer reaction induced by  $^{58}\text{Ni}$  was estimated to be the order of  $10^{-5}$  to  $10^{-6}$  mb. Accordingly, the study of  $^{56}\text{Zn}$   $\beta$ -decay should be feasible at facilities like LISE3-GANIL, FRS-GSI, or RIPS-RIKEN.

## 10 Appendix 6: Detailed description of $^{40}\text{Ti}$ data analysis

### 10.1 Calculation of the efficiencies for the detection of protons in a silicon detector

In the measurement of  $\beta$ -delayed proton emission, the range of the heavy-ions of interest is sometimes wider than the thickness of a silicon detector, as can be seen from the case of  $^{40}\text{Ti}$   $\beta$ -decay (see Chapter 3 for details). In this situation, a fraction of protons do not lose their full energy. Such events are usually rejected by requiring an anti-coincidence condition with adjacent detectors. It is important to calculate or to measure the amount of the escaped events (full-energy detection efficiency) in order to be able to deduce the proton branching ratio from the integration of proton peaks. This can be achieved by requiring a coincidence condition with adjacent detectors. However, this approach sometimes suffers from the electronic threshold that is not low enough for registration all of the proton escape events. Fortunately, this quantity can be reliably calculated by using a Monte-Carlo simulation or an analytical calculation. The experimental results and the results from the Monte-Carlo simulation were described and compared in Chapter 3 and in 错误! 未找到引用源。 . Here, a description of the analytical calculation is presented.

This approach is based on the assumption of a heavy-ion being implanted into a silicon counter of thickness  $T$  with a uniform range profile. The relationship between proton energy and range  $R$  in silicon material was found in a range table [ZIE80]. The calculation of the full-energy detection efficiency was divided into two cases (see Figure 1 for more details).

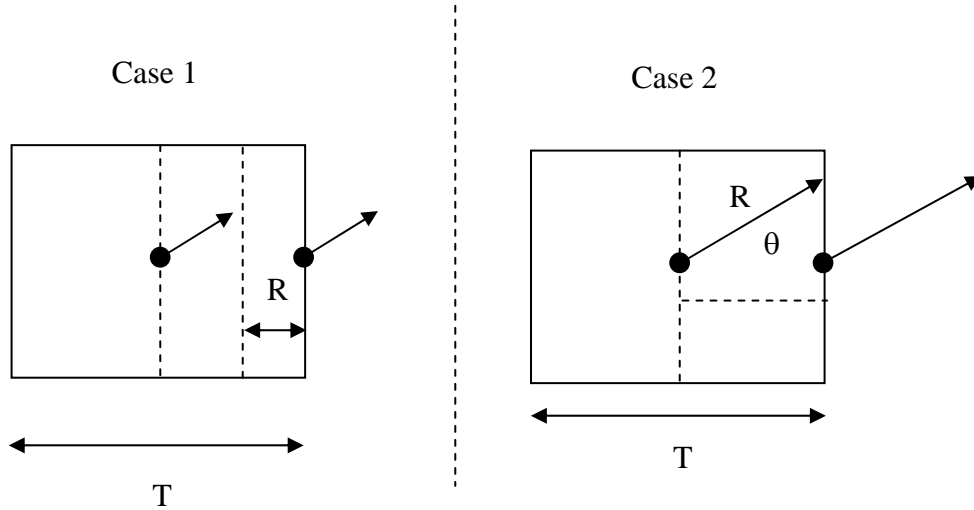


Figure 1: Schematic drawing of proton emissions from a silicon detector.

Case 1:  $R \leq T/2$

The thickness  $t_{full}$  of a central layer, which corresponds to the full stopping of a proton ( $\varepsilon_{full} = 100\%$ ) is,

$$t_{full} = T - 2R$$

Outside this layer, protons can either stop or escape, depending on their emitting angles. The extreme case is proton emission occurring at the surface of the silicon

counter, with the full energy detection efficiency  $\varepsilon_{sur}$  being 50 %. Taking an average between the “surface efficiency” ( $\varepsilon_{sur} = 50$  %) and the efficiency for detection of a proton emitted from the edge of the central layer ( $\varepsilon = 100$  %), the averaged efficiency  $\varepsilon_{out}$  is 75 %. The efficiency in a silicon counter  $\varepsilon_{ave}$  is then derived as a weighted average,

$$\varepsilon_{ave} = \frac{\varepsilon_{full}t_{full} + \varepsilon_{out}t_{out}}{T} = \frac{1.0(T - 2R) + 0.75(2R)}{T}.$$

Case 2:  $R > T/2$

Here the efficiency is determined by averaging efficiencies under two extreme situations, namely a proton being emitted from the center point of a detector and from its surface.

At the center point, the angle  $\theta$ , with which the proton has a path length of  $R$  can be calculated as  $\theta = \cos^{-1}(T/2R)$ . Apparently, the proton emitted within this angle escapes either in forward or backward direction, the full-energy detection efficiency  $\varepsilon_{cen}$  at this point is:  $\varepsilon_{cen} = 1 - 2(1 - \cos\theta)/2 = \cos\theta$ .

On the surface, the efficiency  $\varepsilon_{sur}$  is 50 %. The averaged efficiency  $\varepsilon_{ave}$  is thus

$$\varepsilon_{ave} = (\varepsilon_{cen} + \varepsilon_{sur})/2 = (0.5 + \cos\theta)/2$$

Combining the formulae determined for Case 1 and Case 2, the full-energy detection efficiency is calculated and compared with a Monte-Carlo calculation [TRI]. The results are summarized in Table 1.

Table 1: The full-energy detection efficiency ( $\varepsilon_{ave}$ ) of a silicon detector with a thickness of 300  $\mu\text{m}$  for protons, compared with that obtained by a Monte-Carlo calculation ( $\varepsilon_{MC}$ ) [TRI].

Case	$E_p$ (MeV)	$R$ ( $\mu\text{m}$ )	$\varepsilon_{ave}$ (%)	$\varepsilon_{MC}$ (%)
1	1	16.0	97	97.3
1	2	48.2	92	92.2
1	3	91.5	85	84.6
1	4	147.6	75	75.2
2	5	214.6	60	64.2
2	6	292.2	51	51.3

It can be seen from Table 1 that a good agreement was reached between the analytical calculation and the Monte-Carlo simulation. Since the present method is based on a simple analytical form, it is much easier to use with the help of a range-energy table.

## 10.2 Measurement of the efficiency of NaI detectors

In the experiment on  $^{40}\text{Ti}$   $\beta$ -decay, 14 NaI detectors were arranged around the silicon detectors in order to measure  $\gamma$ -rays emitted in the decay process. The task was to measure the detector efficiency dependence upon  $\gamma$  energy and the source position.

This section presents the experimental NaI efficiencies obtained by using a mixed  $\gamma$  source.

The  $\gamma$ -source was positioned in a way that simulating the  $^{40}\text{Ti}$ -implantation profile in order to obtain the position dependence of the total and individual efficiencies of NaI detectors in the  $\beta$ -decay measurement. The efficiency was deduced by using the formula:  $\varepsilon(E_\gamma) = N(E_\gamma)/I_\gamma/t_{\text{real}}$ , where  $\varepsilon(E_\gamma)$  is the photo-peak efficiency at energy  $E_\gamma$ ,  $N(E_\gamma)$  the integrated counts within  $E_\gamma$  photo-peak,  $I_\gamma$   $\gamma$  intensity calculated for the respective measurement by using the decay half-life and the initial  $\gamma$  intensity of the source, and  $t_{\text{real}}$  the real time of the data taking system. We obtained the later quantity by comparing the number of real and accepted triggers. The dead time loss typically amounted to 40 %. The results are summarised in Table 2 and Table 3.

Table 2: The individual NaI detector efficiency at a  $\gamma$  energy of 1173 keV, with the  $\gamma$  source positioned at the center (Eff1) and at the upper part (Eff2) of the silicon counter No. 4.

No.	1	2	3	4	5	6	7	8	9	10	11	12	13	14
Eff1 (%)	1.9	1.0	0.9	0.9	1.2	1.2	1.3	2.0	1.3	0.8	0.8	0.9	1.5	1.7
Eff2 (%)	1.8	1.4	1.0	0.8	1.0	1.0	1.5	1.9	1.4	0.9	0.8	0.8	1.5	1.7

Table 3: The summed efficiency of the NaI detectors No. 1 to No. 13 (in the data taking period, detector No. 14 did not function) versus source position and  $\gamma$  energy.

Source position	662 keV	1173 keV	1332 keV
Si det. No. 4 center	23 %	16 %	15 %
Si det. No. 4 up	21 %	16 %	15 %
Si det. No. 4 right	21 %	16 %	15 %
Si det. No. 5 center	22 %	17 %	16 %
Average	22(3) %	16(2) %	15(2) %

These data show that, although the individual efficiencies differed due to the difference of the source-detector distance, the summed efficiencies are independent of the source position within the experimental uncertainties. This can be explained by the large solid angle coverage (80 %) of the NaI detector setup. Such results greatly simplified the data analysis, since the position dependence of the  $\gamma$ -efficiency can be neglected for the proton- $\gamma$  coincidence data. The photo-peak efficiency at the  $\gamma$ -energy of 2.5 MeV was determined to be 13(3) % by using a polynomial extrapolation.

### 10.3 Estimation of uncertainty for branching ratios and decay trengths

#### 10.3.1 Branching ratios

The peaks in the proton spectra were classified into main peaks (proton branching ratio  $b_p > 5$  %) and small peaks or energy groups ( $b_p < 5$  %). The small energy groups were further classified into groups inside the tail of a main peak and those outside the tail of a main peak.

For the main peak, the  $b_p$  value was deduced by,

$$b_p = \frac{A}{N(1-f)\varepsilon} \text{ and } A = A_p + A_t,$$

A being the area of the peak, N the number of implanted particles, f the fraction of secondary reaction,  $\varepsilon$  the full-energy detection efficiency discussed above,  $A_p$  the area of the central peak, and  $A_t$  the tail area of the peak deduced from the fitting procedure.

The uncertainty contributions, which are divided into statistical (stat.) and systematical (sys.) are listed in the Table 4. All of the numbers represent the relative uncertainties. According to the error prorogation law, the accumulated uncertainties are tabulated and the final uncertainties for  $b_p$  are also given in Table 4.

Table 4: The uncertainties of proton branching ratios

Uncertainty (%)	Stat.	Sys.	Total
$A_p$	2-5		2-5
$A_t$	5-10	50	50
$\varepsilon$		3-4	3-4
N	1		1
f		20	20
1-f			3-4
$A_p + A_t$			8-13
I/e			9-14
$b_p$			10-14

The number of events assigned to small energy groups inside the tail were obtained by correcting the area integration ( $A_p$ , typically 200(14) ) for the fitted contribution ( $A_t$ , typically 100(50) ) of the main peak. The final uncertainties for such  $b_p$  value is 50 %.

For the small energy groups outside the tail, the poor statistics of the area integration dominate the uncertainties. Typically N range from 10 to 100, so that the uncertainty is 15 to 30 %.

### 10.3.2 Decay strength

The decay strength B is derived by,

$$B = K/ft$$

where  $t = t_{1/2}/b_p$  and K is a constant, f the phase-space factor, and  $t_{1/2}$  the decay half-life. The uncertainties of these parameters are 1 %, 4 %, and 0.1 % for f,  $t_{1/2}$ , and K, respectively.

Combining the uncertainties of  $b_p$  from the above discussion, the uncertainties of the proton branching ratios and of decay strengths are obtained as shown in Table 5.



Table 5: Final uncertainties of proton branching ratio and decay strength

Case	$b_p$ (%)	B (%)
Main peak	10-14	10-14
Small energy groups inside the tail	50	50
Small energy groups outside the tail	15-30	15-30



## 11. References

- [ADE91] E.G. ADELBERGER *ET AL.*, PHYS. REV. LETT. 67 (1991) 3658.
- [ADE97] E.G. ADELBERGER *ET AL.*, IN *SOLAR FUSION RATES* (1997) UNPUBLISHED.
- [AND96] B. D. ANDERSON *ET AL.*, PHYS. REV. C54 (1996) 602.
- [AND98] B. D. ANDERSON, PRIVATE COMMUNICATION
- [AUD97] G. AUDI *ET AL.*, NUCL. PHYS. A624 (1997) 1.
- [AZH98] A. AZHARI *ET AL.*, PROGRESS IN RESEARCH, 1997-1998, CYCLOTRON INSTITUTE, TEXAS A&M UNIVERSITY.
- [BAH86] J.N. BAHCALL *ET AL.*, PHYS. LETT. B178 (1986) 324.
- [BAH95] J. N. BAHCALL, REV. MOD. PHYS. 67 (1995) 781.
- [BAH96] J. N. BAHCALL, NUCL. PHYS. B (PROC. SUPPL.) 48 (1996) 309.
- [BAI95] X. BAI *ET AL.*, NUCL. PHYS. A588, (1995) 273C.
- [BAR80] F. C. BARKER, AUST. J. PHYS. 33 (1980) 177.
- [BAR86] F.C. BARKER AND R.H. SPEAR, ASTROPHYS. J. 307 (1986) 807.
- [BEL97] G. BELLINI, 1997, NUPECC REPORT, NUCLEAR PHYSICS IN EUROPE: HIGHLIGHTS AND OPPERTUNITIES, EDITED BY J. VERVIER *ET AL.*, P. 93.
- [BEL97A] E. BELLOTTI, 1997, IN PROCEEDINGS OF THE 8<sup>TH</sup> INTERNATIONAL CONFERENCE ON NUCLEAR REACTION MECHANISMS, EDITED BY E. GADIOLI, SUPPLEMENTO N. 111, P. 666.
- [BRO85] B.A. BROWN *ET AL.*, AT. DATA NUCL. DATA S 33 (1985) 347.
- [BRO92] B.A. BROWN, PHYS. REV. LETT. 69 (1992) 1034.
- [CAU98] E. CAURIER *ET AL.*, PHYS. REV. C57 (1998) 2316.
- [DAR96] A. DAR AND G. SHAVIV, NUCL. PHYS. B (PROC. SUPPL.) 48 (1996) 335.
- [DÉT90] C. DÉTRAZ *ET AL.*, NUCL. PHYS. A519 (1990) 529.
- [ELS34] W. ELSASSER, J.PHYS. RAD.5 (1934) 625.
- [END90] P.M. ENDT, NUCL. PHYS. A521 (1990) 1.
- [FAU96] L. FAUX *ET AL.*, NUCL. PHYS. A602 (1996)167.
- [FER98] J.C. FERNANDES *ET AL.*, 1998, IN PROCEEDINGS OF THE 2<sup>ND</sup> INTERNATIONAL CONFERENCE ON EXOTIC NUCLEI AND ATOMIC MASSES (TO BE PUBLISHED).
- [FIL83] B.W. FILIPPONE *ET AL.*, PHYS. REV. LETT. 50 (1983) 412

- [FUK98] Y. FUKUDA *ET AL.*, HEP-EX/9807003, SEE ALSO  
[HTTP://WWW.PS.UCI.EDU/~SUPERK/](http://www.ps.uci.edu/~superk/)
- [GAG96] C.A. GAGLIARDI *ET AL.*, PHYS. REV. LETT. 80 (1998) 421.
- [GEI92] H. GEISSEL *ET AL.*, NUCL. INSTR. METH. B70 (1992) 286.
- [GEI95] H. GEISSEL *ET AL.*, ANN. REV. NUCL. PART. SCI. 45 (1995) 163.
- [GOL74] A. S. GOLDBERGER, PHYS. LETT. B53 (1974) 396.
- [GON82] S. A. GONCHAROV *ET AL.*, SOV. J. NUCL. PHYS. 35(3) (1982) 383.
- [HAI83] R.C. HAIGHT *ET AL.*, NUCL. INST. METHODS 212 (1983) 245.
- [HAM98] H. HAMMACHE *ET AL.*, PHYS. REV. LETT. 80 (1998) 929.
- [HAX50] O. HAXEL, J.H.D. JENSEN, AND H.E. SUESS, Z. PHYSIK 128 (1950) 295.
- [HON97] A. HONKANEN *ET AL.*, NUCL. PHYS. A621(1997) 689.
- [ICA93] ICARUS COLLABORATION, ICARUS II PROPOSAL, LNGS REPORT 95/99-I(1993), SEE ALSO  
[HTTP://WWW.AQUILA.INFN.IT:80/ICARUS/MAIN.HTML](http://www.aquila.infn.it:80/icarus/main.html).
- [JUN98] M. JUNKER, 1998, IN PROCEEDINGS OF THE INTERNATIONAL WORKSHOP XXVI ON GROSS PROPERTIES OF NUCLEI AND NUCLEAR EXCITATIONS, EDITED BY M. BABALLA *ET AL.* (GSI, DARMSTADT), P. 271.
- [KAL97] N. I. KALOSKAMIS *ET AL.*, PHYS. REV. C55 (1997) 630.
- [KOX85] S. KOX *ET AL.*, PHYS. LETT. 159B (1985) 15.
- [KUN] P.D. KUNZ, COMPUTER CODE DWUCK4.
- [LIU90] W. LIU *ET AL.*, NUCL. INSTRUM. METHODS, A287 (1990) 476.
- [LIU96] W. LIU *ET AL.*, PHYS. REV. LETT 77 (1996) 611.
- [LIU97] W. LIU *ET AL.*, Z. PHYS. A359 (1997)1.
- [LIU98] W. LIU *ET AL.*, PHYS. REV. C (IN PRESS).
- [MAY48] M.G. MAYER, PHYS. REV. 74 (1948) 235.
- [MAY50] M.G. MAYER, PHYS. REV. 78 (1950) 16.
- [MAY55] M.G. MAYER AND J.H.D. JENSEN, IN ELEMENTARY THEORY OF NUCLEAR SHELL STRUCTURE, JOHN WILEY & SONS, INC., NEW YORK (1955).
- [MET86] V. METAG *ET AL.*, COMMENTS NUCL. PART. PHYS. 16 (1986) 213.
- [MOR94] D.R.O. MORRISON, 1994, IN 27<sup>TH</sup> INTERNATIONAL CONFERENCE ON HIGH ENERGY PHYSICS.
- [MOT94] T. MOTOBAYASHI *ET AL.*, PHYS. REV. LETT. 73 (1994) 2680.
- [MUE93] A.C. MUELLER *ET AL.*, ANN. REV. NUCL. PART. SCI. 45 (1993) 529.

- [OBE98] L. OBERAUER, 1998, IN PROCEEDINGS OF THE INTERNATIONAL WORKSHOP XXVI ON GROSS PROPERTIES OF NUCLEI AND NUCLEAR EXCITATIONS, EDITED BY M. BABALLA *ET AL.* (GSI, DARMSTADT), P. 262.
- [ORM89] W.E. ORMAND *ET AL.*, NUCL. PHYS. A491 (1989) 1.
- [ORM95] W.E. ORMAND *ET AL.*, PHYS. LETT. B345 (1995) 343.
- [PER76] C. M. PEREY, ATOMIC DATA AND NUCLEAR DATA TABLES 17(1) (1976) 2.
- [PIE94] A. PIECHACZEK, PH.D. THESIS, TECHNISCHE HOCHSCHULE DARMSTADT 1994.
- [PIE95] A. PIECHACZEK *ET AL.*, NUCL. PHYS. A584 (1995) 509.
- [POU87] F. POUGHEON *ET AL.*, Z. PHYS. A327 (1987) 17.
- [SAT83] G.R. SATCHLER, IN *DIRECT NUCLEAR REACTIONS* (OXFORD UNIVERSITY PRESS, OXFORD, 1983), P. 786.
- [SCH] C. SCHEIDENBERGER, COMPUTER CODE ATIMA.
- [SEX74] R.G. SEXTRO *ET AL.*, NUCL. PHYS. A234 (1974) 130.
- [SÜM90] K. SÜMMERER *ET AL.*, PHYS. REV. C42 (1990) 2546.
- [TAK97] Y. TAKEEUCHI, 1997, IN '97 ELECTROWEAK INTERACTIONS & UNIFIED THEORIES, EDITED BY J. TRAN THANH VAN (EDITIONS FRONTIERES, PARIS), P. 335.
- [TAN97] X. TANG, MASTER THESIS, CHINA INSTITUTE OF ATOMIC ENERGY, 1997.
- [TOT96] Y. TOTSUKA, NUCL. PHYS. B (PROC. SUPPL.) 48 (1996) 547.
- [TOW73] I.S. TOWNER, NUCL. PHYS. A216 (1973) 589.
- [TRI] W. TRINDER, COMPUTER CODE EFFPROT.
- [TRI95A] W. TRINDER *ET AL.*, PHYS. LETT. B348 (1995) 331.
- [TRI95B] W. TRINDER *ET AL.*, PHYS. LETT. B349 (1995) 267.
- [TRI95C] W. TRINDER, PH.D. THESIS, UNIVERSITÄT FRANKFURT A.M. 1995.
- [TRI97A] W. TRINDER *ET AL.*, NUCL. PHYS. A620 (1997) 191.
- [TRI97B] W. TRINDER *ET AL.*, PHYS. LETT. B 415 (1997) 211.
- [VIE78] D. J. VIEIRA, PH.D. THESIS, LBL-7161 (1978).
- [WAN88] D. WANG *ET AL.*, NUCL. PHYS. A480 (1988) 285.
- [WIG57] E.P. WIGNER, IN PROC. OF THE ROBERT A. WELCH FOUNDATION CONFERENCE ON CHEMICAL RESEARCH, HOUSTON, 1957, ED. W.O. MILLIKAN, P. 67.
- [XU94] H.M. XU *ET AL.*, PHYS. REV. LETT. 73 (1994) 2027.
- [YAM89] T. YAMAGATA *ET AL.*, RNCP ANNUAL REPORT 62 (1989).

- [ZHO85] Z. Y. ZHOU *ET AL.*, PHYS. REV. C31 (1985) 1941.
- [ZIE80] J.F. ZIEGLER, 1980, IN STOPPING CROSS-SECTIONS FOR  
ENERGETIC IONS IN ALL ELEMENTS, EDITED BY J.F.  
ZEIGLER (PERGAMON PRESS).

